Measurement of the W boson Mass using Electrons at the Edge of DØ Central Calorimeter Modules

A Dissertation Presented

by

Yaroslav Kulik

to

The Graduate School

in Partial Fulfillment of the
Requirements
for the Degree of
Doctor of Philosophy
in
Physics

State University of New York
at
Stony Brook

August 2001

ii

State University of New York
at Stony Brook

The Graduate School

Yaroslav Kulik

We, the dissertation committee for the above candidate for the Doctor of
Philosophy degree, hereby recommend acceptance of this
dissertation.

Professor Paul Grannis, Dissertation Advisor

Professor John Hobbs, Chairperson of Defense

Professor Konstantin Likharev, Committee Member

Professor Ron Madaras , Outside Member

This dissertation is accepted by the Graduate School.

Dean of the Graduate School

Abstract of the Dissertation

Measurement of the W boson Mass using Electrons at the Edge of DØ Central Calorimeter Modules

by

Yaroslav Kulik

Doctor of Philosophy

in

Physics

State University of New York

at Stony Brook

2001

We present a measurement of the W boson mass in proton-antiproton collisions at $\sqrt{s} = 1.8$ TeV based on a data sample of integrated luminosity 82 pb^{-1} collected by the DØ detector at the Fermilab Tevatron. We utilize

$e\nu$ events in which the electron shower is close to the edge of one of the 32 modules in the DØ central calorimeter. The electromagnetic calorimeter response and resolution in this region differs from that in the rest of the module and electrons in this region were not previously utilized. We determine the calorimeter response and resolution in this region using $Z \rightarrow ee$ events. We extract the W boson mass by fitting to the transverse mass and the electron and neutrino tranverse momentum distributions. The result is combined with previous DØ results and we obtain an improved measurement of the W boson mass of $M_W = 80.483 \pm 0.084$ GeV.

To Sid and Nancy

Contents

List of Figures

xiii

List of Tables

Acknowledgements

First of all, I would like to pay my respect to all the people from the DØ Collaboration, to all who designed, built and ran the detector for all these years. It really is an enormous accomplishment, which I came to appreciate more and more with time.

Special thanks goes to my adviser, Paul Grannis, for always finding time for me and leaving a lot of room to make my own decisions and a freedom to choose any research project.

I would like to thanks members of my Editorial Board, especially Ashutosh Kotwal, John Ellison, Paul Grannis and Ron Madaras for greatly contributing to this analysis and helping me with the most unpleasant part of documenting it.

And finally, I'd like to thank Bogdan and my closest friends: Ru, Dennis, Alexey, Andrei, B&B for being around me and creating an environment that

transformed all these years into a very enjoyable time.

Chapter 1

Introduction

The study of the properties of the W boson began in 1983 with its discovery by the UA [1] and UA2 [2] Collaborations at the CERN $p\overline{p}$ collider. Together with the discovery of the Z boson in the same year [3, 4], it provided a direct confirmation of the unified description of the weak and electromagnetic interactions, which together with the theory of the strong interaction (QCD), now constitutes the standard model.

Since the W and Z bosons are the carriers of the weak force, their properties are closely coupled to the structure of the model. The properties of the Z boson have been studied in great detail in e^+e^- collisions at LEP and SLC. The study of the W boson has proved significantly more difficult, since

DØ combined W mass [8]	80.482 ± 0.091 GeV
CDF combined W mass [9]	80.433 ± 0.079 GeV
Tevatron W mass [15]	80.452 ± 0.062 GeV
LEP combined W mass [14]	80.446 ± 0.040 GeV
World Average (direct W mass measurements) [14]	80.448 ± 0.034 GeV

Table 1.1: List of recent W mass measurements

it is charged and so can not be resonantly produced in a e^+e^- collider. Until recently its direct study has been the realm of experiments at $p\overline{p}$ colliders [5, 6, 7, 8, 9]. Direct measurements of the W boson mass have also been carried out at the CERN e^+e^- collider LEP2, using non-resonant W pair production [10, 11, 12, 13]. A summary of these measurements can be found in Table 1.1. CDF measured the W mass in two decay channels: $\mu\nu$ and $e\nu$. The total number of W events from both channels exceeds the DØ statistics and helped to achieve a smaller uncertainty, though DØ has a better single channel W mass uncertainty. Four LEP experiments (ALEPH, DELPHI, L3, OPAL) directly measured the W mass from W pair production and subsequent decay in to $q\overline{q}q\overline{q}$, $q\overline{q}l\overline{\nu}_l$ and $l^-\overline{\nu}_l l'^+\nu_{l'}$. The uncertainties from each experiment individually is about 77 MeV, but the combination of four of them results in an impressive 40 MeV.

The standard model links the W boson mass to other parameters. As

described in the later chapters, in the standard model W boson mass is determined by three precisely measured quantities: the Z boson mass M_Z, the Fermi constant G_F, and the electromagnetic coupling constant α evaluated at $Q^2 = M_Z^2$ and the radiative corrections. Higher order corrections are dominated by loop diagrams involving the top quark and the Higgs boson. The measurement of the W mass contrains the size of the radiative correction. With a measured top quark mass, this gives a constraint on Higgs boson mass.

A measurement of the W boson mass (M_W) thus constitutes a test of the standard model. In conjunction with a measurement of the top quark mass [16, 17], the standard model predicts M_W up to a 200 MeV uncertainty arising from the unknown Higgs boson mass. By comparing the standard model calculation to the measured value of the W boson mass, we can constrain the mass of the Higgs boson, the standard model source of electroweak symmetry breaking, which so far has not been discovered. A discrepancy with the range allowed by the standard model could indicate new physics. The experimental challenge is thus to measure the W boson mass to sufficient precision, about 0.1%, to be sensitive to these corrections. Figure 1.1 shows current constraints on the mass of the Higgs boson from the world W mass

Run Ia DØ W mass (1991-1992 data) [6]	80.35 ± 0.25 GeV
Run Ib DØ CC W mass (1994-1995 data) [7]	80.43 ± 0.11 GeV
Run Ib DØ EC W mass (1994-1995 data) [8]	80.691 ± 0.227 GeV
Combined DØ Run I W mass (1992-1995 data) [8]	80.482 ± 0.091 GeV

Table 1.2: List of DØ W mass measurements. Two Run Ib measurements utilized electrons detected in the Central Electromagnetic Calorimeter (CC) and Forward EM calorimeter (EC).

and top quark mass measurements.

In this work, I describe the measurement of the W boson mass conducted with the DØ Detector [18]. It is, seemingly, the last in the series of DØ W mass measurements which uses the data collected in 1992-1995 with the DØ detector at the Fermilab Tevatron $p\bar{p}$ collider. The other measurements are listed in the Table 1.2. All of them used the $W \to e\nu$ decay channel with the electron detected in either the end electromagnetic (EM) calorimeter (ECEM) or central EM calorimeter (CCEM). We continued to exploit the $W \to e\nu$ decay channel with the electron detected in the DØ central electromagnetic calorimeter (CCEM). However, in this thesis we concentrate on the narrow region of the CCEM where EM response is thought to be different from the rest of the calorimeter. Events with the electrons in that region have not been utilized before, for that reason. However, there are many sim-

4

ilarities between this analysis and the previous CC analysis. The theoretical calculations behind the Monte Carlo simulations of the production and the decay of the W boson are the same, and the model describing the hadronic recoil is the same. In this dissertation, I will focus primarily on the parts of the analysis which are different from the previous CC measurement. The CC measurement has already been well documented in two theses [19, 20]. In this dissertation, I will give a detailed account of the original parts of the measurement but will only mention and give brief overviews of the details of the work unchanged from the CC analysis.
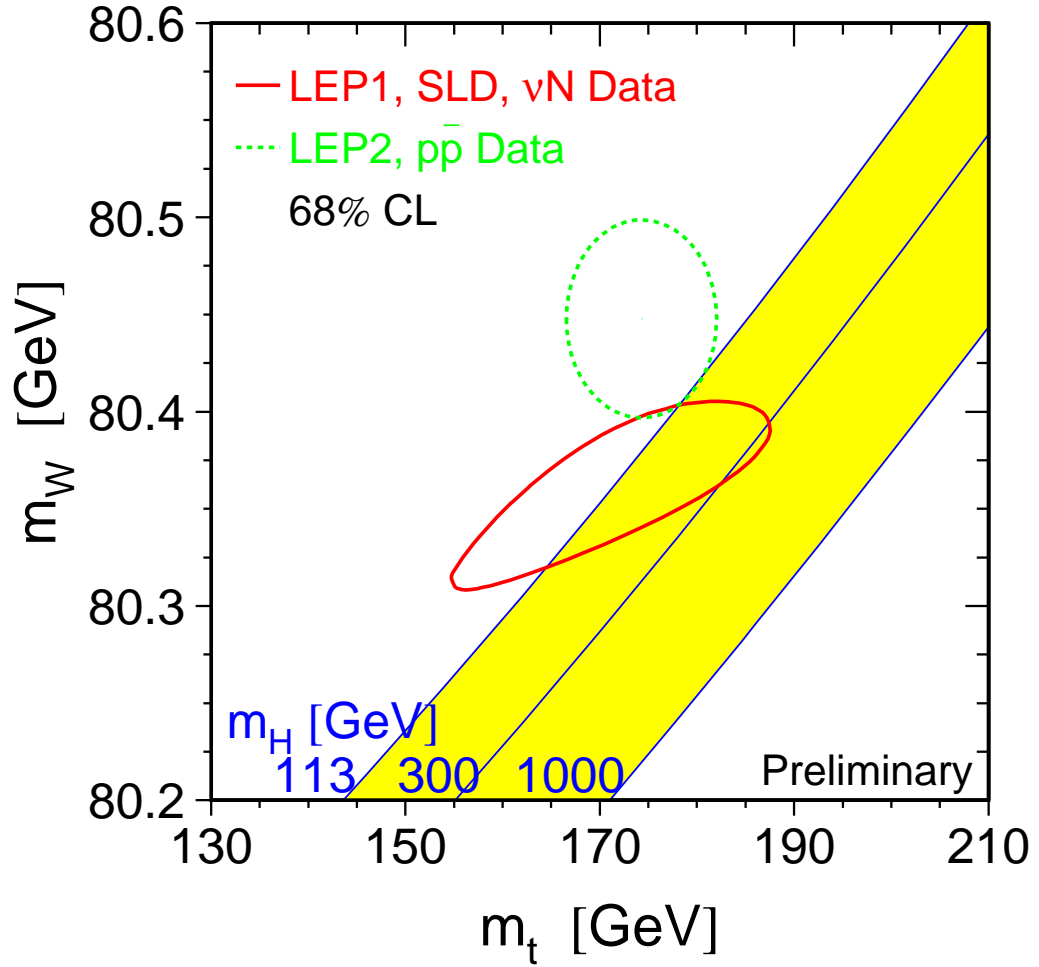
Figure 1.1: The indirect measurements of M_W and m_t (LEP-I+SLD+νN data) (solid contour) and the direct measurement ($p\overline{p}$ colliders and LEP-II data) (dashed contour). In both cases the 68% CL contours are plotted. Also shown is the Standard Model relationship for the masses as a function of the Higgs boson mass.

Chapter 2

Theory

2.1   Introduction

To extract the W mass from a sample of W candidate events recorded at DØ ,
we generate predictions for several kinematic spectra as a function of the
W boson mass. These predictions are then compared to the corresponding
spectra from the data. The mass is measured by choosing the prediction
which best matches the data. This chapter gives a brief overview of the
theory behind these calculations. The purpose is to introduce basic terms
and highlight the key dependences of the W boson mass on the observable
quantities that this analysis uses. The detailed description of the theory

of the weak and electromagnetic interactions in the standard model can be found elsewhere [21].

2.2 Standard Model of Electroweak Interactions

The standard model of electroweak interactions is based upon the $SU(2)_L \times U(1)$ local gauge group. L means that $SU(2)$ acts only on the left-handed components of the lepton and quark fields. Left-handed means the particle has negative helicity. Helicity is the projection of the spin along the direction of the momentum. All known left-handed leptons and quarks are combined into doublets and right-handed fields in singlets on which a symmetry group acts and as follows

$$
\begin{pmatrix} \nu_e \\ e \end{pmatrix}_L , \begin{pmatrix} \nu_\mu \\ \mu \end{pmatrix}_L , \begin{pmatrix} \nu_\tau \\ \tau \end{pmatrix}_L , \; e_R, \; \mu_R, \; \tau_R, \; \nu_{eR}, \; \nu_{\mu R}, \; \nu_{\tau R}
$$

The subscript R refers to the right handed component of the fields. In the same manner, the quarks are divided into the doublets and the singlets

8

as

$$\begin{pmatrix} u \\ d' \end{pmatrix}_L , \begin{pmatrix} c \\ s' \end{pmatrix}_L , \begin{pmatrix} t \\ b' \end{pmatrix}_L , \ u_R, \ c_R, \ t_R, \ d_R, \ s_R, \ b_R$$

The prime on d,s and b indicates that the quark mass eigenstates are not the same as the weak interaction eigenstates. The weak eigenstates may be written as a linear combination of mass eigenstates. In the theory with only two families (which existed before discovering the third generation), the d' states could be expressed as

$$d' = d \cos\theta_C + s \sin\theta_C$$

where θ_C is known as the Cabibbo angle and regulates the mixing between the families. The full three generation matrix is called the CKM matrix and is named after Cabibbo, Kobayashi and Maskawa.

$$\begin{pmatrix} d' \\ s' \\ b' \end{pmatrix} = \begin{pmatrix} V_{ud} & V_{cd} & V_{td} \\ V_{us} & V_{cs} & V_{ts} \\ V_{ub} & V_{cb} & V_{tb} \end{pmatrix} \begin{pmatrix} d \\ s \\ b \end{pmatrix}$$

The inclusion of the abelian U(1) group incorporates the electric charge into

9

the theory. The $SU(2)_L \times U(1)$ group yields two charged and two neutral gauge bosons. The bosons must be massless in order for the theory to be renormalizable. Through the Higgs mechanism the symmetry of the $SU(2)_L \times U(1)$ is broken and the charged $(W^\pm)$ and neutral (Z) bosons acquire mass with the photon (γ) remaining massless.

The Higgs mechanism introduces to the Standard model four Lorentz scalar fields conforming to SU(2)xU(1) symmetry and thus organized into a weak iso-spin doublet $\phi = (\phi^+, \phi^0)$ with each doublet component being a complex field consisting of two scalar fields.

$$\phi^+ \equiv (\phi_1 + i\,\phi_2)/\sqrt{2}$$
$$\phi^0 \equiv (\phi_3 + i\,\phi_4)/\sqrt{2} \tag{2.1}$$

The effective potential of such field is

$$V(\phi) = \mu^2 \phi^+ \phi^0 + \lambda(\phi^+ \phi^0)^2$$

where μ is the mass term and λ is the coupling constant. If $\mu^2 < 0$ such a potential has a non zero minimum in 4 dimensional $\phi^+ \phi^0$ space at $|\phi|^2 = -\mu^2/2\lambda = v^2$. Three out of four components could be chosen freely still

10

keeping the field at minimum. In the Standard model the vacuum expectation value is chosen at : $\phi_2 = v$ and $\phi_{1,3,4} = 0$. Near the minimum the Higgs field can be represented as:

$$\phi = \begin{pmatrix} 0 \\ v + H \end{pmatrix}$$

One of the degrees of freedom transforms into a scalar, neutral Higgs boson and three others generate the masses for W^{+-}, Z^0 bosons. $M_W = \frac{1}{2}(gv)$ and $M_Z = \frac{v}{2}\sqrt{g^2 + g'^2}$. The mass of the Higgs boson itself is $\sqrt{2\lambda v^2}$. λ is a free parameter in this theory and has to be determined experimentally.

The electroweak theory has three free parameters (besides quark and lepton masses), that have to be measured experimentally. These are the coupling strength of the SU(2) weak isospin (g), the U(1) hypercharge coupling (g'), and the vacuum expectation value (v) from the spontaneous symmetry breaking. However, it is often more convenient to work with parameters determined from low energy weak interactions. Such variables are the fine structure constant $\alpha = \frac{e^2}{4\pi}$, the Fermi constant G_F and $\sin^2 \Theta_W$, where Θ_W is the weak mixing angle [22, 23].

The first two constants are known to a very high precision. The current

11

values for $\alpha(Q^2 \approx 0)$ and G_F are [24]

$$\alpha = 1/137.0359895(61)$$

$$G_F = 1.16639(2) \times 10^{-5} \text{ GeV}^{-2}$$

According to the standard model, at the lowest order of pertrubation theory, the masses of the W and Z bosons are then given by

$$M_W = \frac{A}{\sin \Theta_W} \tag{2.2}$$

$$M_Z = \frac{A}{\sin \Theta_W \, cos\Theta_W} \tag{2.3}$$

where

$$A = \left(\frac{\pi \, \alpha}{\sqrt{2}G_F} \right)^{\frac{1}{2}} \tag{2.4}$$

or $\sin^2 \Theta_W$ as

$$\sin^2 \Theta_W \equiv 1 - \frac{M_W^2}{M_Z^2}$$

With a measurement of $\sin^2 \Theta_W$ the W and Z boson masses can be predicted using the equations 2.2 and 2.3. However, the contibutions from higher order

loop diagrams are essential and modify Eq. 2.2 to

$$M_W = \frac{A}{\sin \Theta_W \sqrt{1 - \Delta r}} \tag{2.5}$$

where $\Delta r = \Delta r(M_{\text{Higgs}}, M_{\text{quarks}}, M_{\text{leptons}}, ...)$ incorporates the effect of higher order quantum corrections and depends upon the masses in the theory. The value of Eq. 2.4 is also modified because of the running of the electromagnetic coupling constants to the scale of M_W. The mass dependence on the two most interesting particles, the Higgs boson and top quark, enter in the following way

$$\Delta r(M_{\text{Higgs}}) \propto \ln \left(\frac{M_{\text{Higgs}}}{M_W} \right) \tag{2.6}$$

$$\Delta r(M_{\text{top}}) \propto \left(\frac{M_{\text{top}}}{M_W} \right)^2 \tag{2.7}$$

Equation 2.5 is essential in qualitative understanding of how a precise measurements of the M_W and M_{top} constrain the mass of the Higgs. Figure 2.1 gives the two dominant examples of the self energy diagrams that go into the calculation of Eqs. 2.6 and 2.7.

Also, in extensions to the standard model, new particles (besides top quark and the Higgs boson) may lead to additional corrections to the value of
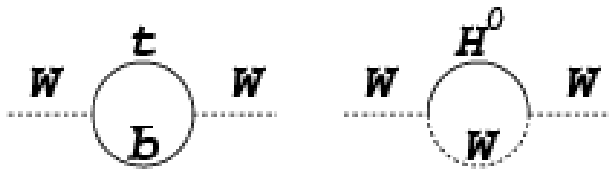
Figure 2.1: Examples of the W boson self energy diagrams involving the top quark and the Higgs boson.

the W boson mass. For example in the minimal supersymmetric extension to the standard model (MSSM) additional corrections can increase the predicted W boson mass by up to 250 MeV [25].

2.3 W boson Production

At lowest order a W boson is produced through quark-antiquark annihilation at the Fermilab collider. The interaction is described by the parton model [26]. The proton consists of three valence quark and the multitude of the "sea" quarks of all "flavors" – u, d, s, c, b, t. In a proton, the valence quarks are two u quarks and one d quark. The antiproton is composed from the charge conjugate anti-quarks. The momentum of parton in a proton is given by its momentum fraction (x) times the momentum of the proton. The
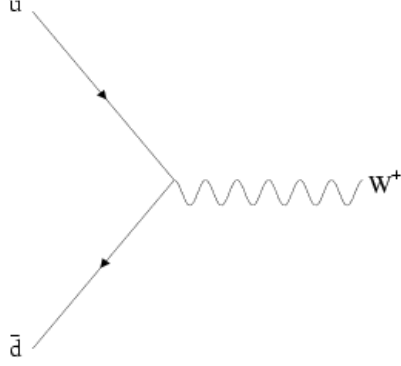
Figure 2.2: W boson production diagram

probability for a parton of "flavor" i, carrying momentum x, to be found in the proton in the interaction at energy scale Q^2 is called a parton distribution function (PDF), $f_i(x, Q^2)$. An example of the production of a W would be a hard scattering of quark u from p and quark $\overline{d}$ from $\overline{p}$ as shown in Fig. 2.2

$$u\overline{d} \rightarrow W^+ \quad . \tag{2.8}$$

The partons in the proton which do not participate in the hard scattering are called "spectators". The spectators cause the collision to contain hadronic debris which does not originate from the hard-scattering process. The debris usually gives extra low transverse momentum particles. These particles are collectively referred to as the "underlying event". The underlying event

15

for production of colorless objects (W, Z production) qualitatively resembles events recorded in generic inelastic $p\bar{p}$ collisions. These interactions are referred to as "minimum bias" interactions. Like the underlying event, the particles produced in minimum bias events are typically soft.

From Eq. 2.8 follows that the energy and momentum of the W boson are given by

$$E = \frac{\sqrt{s}}{2}(x_p + x_{\bar{p}}) \tag{2.9}$$

$$P_L = \frac{\sqrt{s}}{2}(x_p - x_{\bar{p}}) \tag{2.10}$$

where $\sqrt{s}$ is the center of mass energy of the proton-antiproton system and $x_p(x_{\bar{p}})$ is the momentum fraction of the quark from the proton(antiproton). A useful quantity is the rapidity (y) of a particle which is defined to be

$$y \equiv \frac{1}{2} \ln \left(\frac{E + P_L}{E - P_L} \right) \tag{2.11}$$

where E is the energy and P_L is the longitudinal momentum. Since, $E^2 = \vec{p}^{\,2} + m^2$, in the limit of $m \ll E$ the above equation becomes

$$\eta = -\ln \left(\tan \frac{\theta}{2} \right) \tag{2.12}$$

16

where θ is the polar angle and η is referred to as the pseudorapidity. Equations 2.12 is not valid for the W boson because of the large mass but it is valid for the decay products of the boson. By inserting Eq. 2.9 and 2.10 into the 2.11 the rapidity reduces to

$$y = \frac{1}{2} \ln \frac{x_p}{x_{\overline{p}}} \tag{2.13}$$

The total cross section for the W (and Z) production as shown in Eq. 2.8 is the sum over all possible quark combinations from the proton-antiproton system and depends on five quanities:

$$\frac{\partial^5 \sigma(Q, p_T, y, \phi, \epsilon)}{\partial Q \partial p_t \partial y \partial \phi \partial \epsilon} = \sigma(Q, p_t, y, \phi, \epsilon)$$

Where $Q, p_T, y, \phi, \epsilon$ are the $W(Z)$ mass, transverse momentum, rapidity, azimuthal angle and polarization respectively. In the fast Monte Carlo that we use to simulate the W production the differential cross section is factorized into four terms.

$$\frac{\partial^5 \sigma}{\partial Q \partial p_t \partial y \partial \phi \partial \epsilon} \approx \left. \frac{\partial^2 \sigma}{\partial p_T \partial y} \right|_{Q^2 = M_W^2} \times \frac{\partial \mathcal{P}}{\partial Q} \times \frac{\partial \mathcal{P}}{\partial \phi} \times \frac{\partial \mathcal{P}}{\partial \epsilon}$$

17

The ϕ distribution is taken to be a uniform distribution in $[0, 2\pi)$.

The effective cross section is calculated as a sum over all contributing parton flavors and the partonic cross section times the parton distribution functions (PDF) for both p and $\overline{p}$

$$\sigma = \sum_{i,j} \int dx_p dx_{\overline{p}} f_i(x_p, Q^2) f_j(x_{\overline{p}}, Q^2) \hat{\sigma}(i,j)$$

where i and j range over parton flavors, f_i is the PDF for parton i in the proton and f_j the PDF for parton j in the antiproton, and $\hat{\sigma}(ij)$ is the partonic cross section for process 2.8 for a given x_p, $x_{\overline{p}}$.

The mass distribution then can be represented by

$$\frac{\partial \mathcal{P}}{\partial Q} = \mathcal{L}_{q\overline{q}}(Q) \frac{Q^2}{(Q^2 - M_W^2)^2 + \frac{Q^4 \Gamma_W^2}{M_W^2}} \tag{2.14}$$

For the line shape of the W boson we use a Breit-Wigner curve with a mass dependent width. The intrinsic width of the W is $\Gamma_W = 2.062 \pm 0.059$ GeV [27]. The line shape is skewed due to the momentum distribution of the quarks inside the proton and antiprotons. We call this term,

$$\mathcal{L}_{q\overline{q}}(Q) = \frac{2Q}{s} \sum_{i,j} \int_{\frac{Q^2}{s}}^{1} \frac{dx}{x} f_i(x, Q^2) f_j(\frac{Q^2}{sx}, Q^2),$$

18
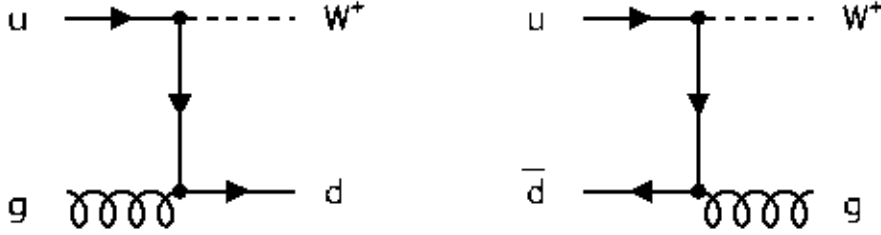
Figure 2.3: The Compton and initial state radiation diagrams which contribute to the transverse momentum of the W boson.

the parton luminosity. To evaluate it, $W \to e\nu$ events were generated using the HERWIG Monte Carlo event generator [28], interfaced with a specific from the PDF libraries [29]. The event selection was subject to the same kinematic and fiducial cuts as for the W and Z samples. The parton luminosity is approximated by function

$$\mathcal{L}_{q\bar{q}}(Q) = \frac{e^{-\beta Q}}{Q},$$

where β is extracted by fitting the HERWIG generated invariant mass distribution with Eq. 2.14, varying β as a fit parameter. The parton luminosity is rapidity dependent so it was essential to apply the same fiducial cuts on the decay leptons in HERWIG events as for the W and Z data.

19

For the interaction shown in Eq. 2.8 the W boson does not have any momentum transverse to the z direction (p_T^W), where the z axis is in the direction of the proton momentum. All W boson events produced in $p\overline{p}$ collisions have some transverse momentum due to initial and final state radiation, $gq \rightarrow Wq$ Compton scattering, and the Fermi motion of the quarks in the hadron. Initial state gluon radiation occurs when a quark radiates gluons before it annihilates to produce the W boson. Figure 2.3 shows the lowest order Compton diagrams that contibute to the transverse momentum of the W boson. At the Tevatron the average p_T^W is about 6 GeV. At such energies perturbative QCD is not valid and non-perturbative corrections are neccessary. In the Monte Carlo generation we relied on the formalism developed by Collins, Soper and Sterman (CSS) [30]. The differential cross section as a function of p_T is given by

$$
\frac{d^2\sigma(AB \rightarrow W)}{dp_T^2 dy} = \frac{\sigma_0}{4\pi s} \int \{ d^2\vec{b} e^{i\vec{p}_T \cdot \vec{b}} \sum_{i,j} \tilde{W}_{ij}(b^*, Q, x_A, x_B) e^{-S(b^*, Q)}
$$
$$
F_{ij}^{NP}(b, Q, Q_0, x_A, x_B) \} + Y(p_t, Q, x_A, x_B) \quad (2.15)
$$

Here, $\widetilde{W}(b^*, Q, x_A, x_B)$ includes the convolution of parton densities for partons i, j, the Cabibbo-Kobayashi-Maskawa elements, and the electroweak

parameters. The quantity Y is the term which dominates at high P_T^W when perturbative QCD is valid. The F term parametrizes the non-perturbative physics. F is known up to some number of phenomenological parameters. In the Monte Carlo we used Ladinsky and Yuan's [32] parametrization which has three parameters g_1, g_2 and g_3 which are not specified by theory and must be measured separately

$$F_{ij}^{NP}(b, Q, Q_0, x_A, x_B) = \exp\left[-b^2 g_1 - g_2 b^2 \ln\left(\frac{Q}{2Q_0}\right) - g1 - g_3 b \ln(100 x_A x_B)\right]$$

Q_0 is a cutoff parameter. Ladinsky and Yuan determined parameters g_1, g_2, g_3 by fitting Drell-Yan and Z data at different values of Q^2. They find the values to be [32]

$$g_1 = 0.11^{+0.04}_{-0.03} \text{ GeV}^2$$

$$g_2 = 0.58^{+0.1}_{-0.2} \text{ GeV}^2 \qquad (2.16)$$

$$g_3 = -1.5^{+0.1}_{-0.1} \text{ GeV}^{-1}$$

for mass cut-off $Q_0 = 1.6$ GeV and the CTEQ2M PDF. The W mass is most sensitive to the parameter g_2. In Ref. [7] DØ used its own Z data to additionally constrain g_2 by fitting the Z transverse momentum distribution. In that analysis, g_2 found to be 0.59 ± 0.10 GeV^2 for the MRSA$'$ PDF. For

more details on the calculation of $\frac{d\sigma}{dp_T^W}$ refer to [30, 31, 32] .

Finally the polarization term for 2.8 process is proportional to

$$\frac{d\mathcal{P}}{d\epsilon} \propto \frac{igV_{ud}}{2\sqrt{2}}\gamma^\mu(1+\gamma_5)$$

The $1+\gamma_5$ term selects only left-handed component of the d field and right-handed component of the $\overline{u}$ field. The d is left-handed if its spin is antiparallel to its momentum, and the $\overline{u}$ is right-handed if its spin is parallel to its momentum. For instance, in the $d\overline{u} \rightarrow W^-$ production, if d comes from the proton the $\overline{u}$ has to come from the antiproton resulting in the negative W^- helicity. The W bosons are produced by the annihilation of two valence quarks, two sea quarks, or one valence and one sea quark. For sea-sea quark combination W has positive or negative helicity with equal probability. For processes involving valence quarks, the W^- bosons always have helicity -1. The fraction of W's produced from two sea quarks f_{ss} is a Monte Carlo parameter. Using HERWIG events, f_{ss} was found to be 0.207 [6], independent of W the boson topology.

2.4 W boson Decay

To measure the mass of the W boson, information must be extracted from the particles into which it decays. The W boson decays into quark-antiquark and lepton-neutrino pairs. Table 2.1 lists the decay products of the W boson and the fraction of time that the decay occurs. The $q\overline{q}$ pairs have the largest branching ratio. When a $q\overline{q}$ pair is produced, two jets of particles are observed. The $W \rightarrow q\overline{q}$ channel suffers from a huge background from direct QCD dijet production. This leaves us with only the lepton modes. In the τ channel, the τ predominantly decays into hadrons making this channel difficult for two reasons. The first is the difficulty in separating the signal from the large QCD background, and second the jet energy scale is not known well enough to make a precise mass measurement. The muon channel also does not allow for a precise mass measurement since the DØ detector does not have a sufficient momentum resolution for high p_T muons. This leaves only the electron channel to measure the mass. The properties of the electron from the W boson decay are discussed below.

At the lowest order the W boson has zero p_T and is fully polarized along the beam direction. As discussed in the last section, the W^- boson helicity is ± 1 for sea-sea quark interaction and is negative in the rest of cases (helicity

23

Decay Products	Branching Ratio
$u\bar{d}, u\bar{s}, c\bar{s}, c\bar{d}$	67.8%
$e^+\nu_e$	10.8%
$\mu^+\nu_\mu$	10.6%
$\tau^+\nu_\tau$	10.8%

Table 2.1: The decay products of the W^+ and the measured branching ratios.

of the W^+ is positive). The angular distribution of the charged lepton in the W rest frame is

$$\frac{d\sigma}{d\cos\theta^*} \propto (1 - \lambda q \cos\theta^*)^2 \qquad (2.17)$$

where λ is the helicity of the W with respect to the proton direction, q is the charge of the lepton or W boson, and θ^* is the angle between the charged lepton and proton beam directions in the W rest frame. When $\mathcal{O}(\alpha_s)$ processes are included, the boson acquires finite p_T and Eq. 2.17 is changed to [33]

$$\frac{d\sigma}{d\cos\theta_{\rm CS}} \propto (1 + \alpha_1(p_T)\cos\theta_{\rm CS} + \alpha_2(p_T)\cos^2\theta_{\rm CS}) \qquad (2.18)$$

for W^- bosons with $\lambda = -1$ and after integration over azimuthal angle. The angle θ_{CS} is defined in the Collins-Soper frame [34]. The values of α_1 and α_2 as a function of transverse boson momentum have been calculated at $\mathcal{O}(\alpha_s^2)$

[33]. Equation 2.18 has been implemented in the fast Monte Carlo.

Other processes that affects the mass measurement are radiative W or Z decay, $W \rightarrow e\nu\gamma$ or $Z \rightarrow ee\gamma$. If the decay electron radiates a photon and the photon is sufficiently separated from the electron (so that its energy in the calorimeter is not included in the electron energy) the measured W boson mass is biased to be low. The same is true if an on-shell W boson radiates a photon and therefore is off-shell when it decays. Calculations from Ref. [35] were used in the Monte Carlo. The calculation gives the fraction of events in which a photon with energy $E(\gamma) > E_0$ is radiated, and the angular distribution and energy of the photons. Radiation by the initial quarks or the W boson, if the final W is on-shell, does not affect the mass of the $e\nu$ pair and have not been included in the Monte Carlo. For the minimum photon energy $E_0 = 50$ MeV assumed in the Monte Carlo, 30.6% of all W decays have a radiated photon. Most of these photons, however, are emitted close to the electron direction and cannot be separated from the electron in the calorimeter. In the Monte Carlo, if the radiated photon is close to the electron we add its energy to the electron. If far away, we added it to the recoil. I will describe this approach in more detail in Chapter 8.4.

The calculation of the spin averaged differential cross section is given by

$$\frac{d\widehat{\sigma}}{d\cos\theta^*}(u\overline{d} \to e^+\nu) = \frac{|V_{ud}|^2}{8\pi}\left(\frac{G_F M_W^2}{\sqrt{2}}\right)^2 \frac{\widehat{s}\,(1+\cos\theta^*)^2}{(\widehat{s}-M_W^2)^2 + (\Gamma_W M_W)^2} \quad (2.19)$$

where θ^* is the angle between the positron and the $\overline{d}$ direction and $\widehat{s}$ is the center of mass energy of the $u\overline{d}$ pair. The neutrino passes through the detector without interacting so its presence can only be inferred from the momentum imbalance in the event. Since many particles with large longitudinal momentum escape detection through the beam pipe, only the momentum in the plane transverse to the beam direction can be balanced. Rewriting Eq. 2.19 in terms of the transverse momentum of the lepton (p_T) yields

$$\frac{d\widehat{\sigma}}{d\widehat{p}_T^2}(u\overline{d} \to e^+\nu) = \frac{|V_{ud}|^2}{\pi}\left(\frac{G_F M_W^2}{\sqrt{2}}\right)^2 \frac{1}{(\widehat{s}-M_W^2)^2 + (\Gamma_W M_W)^2}\frac{1-2\widehat{p}_T^2/\widehat{s}}{\sqrt{1-4\widehat{p}_T^2/\widehat{s}}}$$
$$(2.20)$$

The divergence, when $\widehat{p}_T = \frac{1}{2}\sqrt{\widehat{s}}$, is known as the Jacobian edge and is a characteristic of all two body decays. The edge occurs at half the mass of the decaying particle so by knowing the distribution of the lepton transverse momentum one is then able to measure the mass of the decaying particle. Equation 2.20 is a calculation done at the parton level. The total cross section is a convolution over all possible momentum and quark states and is

26

given by

$$\frac{d\sigma}{dp_T^2}(p\overline{p} \to e^+\nu X) = \frac{1}{3}\sum_{q,\overline{q}}\int_0^1 dx_p \int_0^1 dx_p f_q(x_p) f_{\overline{q}'}(x_{\overline{p}})\frac{d\widehat{\sigma}}{d\widehat{p}_T^2} \qquad (2.21)$$

where $f_q(x_p)$ is the fraction of momentum carried by quark(antiquark) $q(\overline{q}')$ from the (anti)proton. The singularity in Eq. 2.20 is removed by the intergration over the Breit-Wigner lineshape and the finite natural width of the W boson.

A problem with measuring M_W from the transverse momentum distribution of the lepton is the uncertainty in p_T^W. This is because the transverse momentum of the W adds directly to the lepton momentum distorting the Jacobian edge. The calculations of the p_T^W contain theoretical momentum uncertainties which lead to an uncertainty on the W boson mass. p_T^W can be measured experimentally but with poor resolution (see explanations below).

Another quantity that has a Jacobian edge is the tranverse mass (m_T), given by

$$m_T = \sqrt{2p_T^e p_T^\nu (1 - \cos\phi^{e\nu})}, \qquad (2.22)$$

where $\vec{p_T^e}$ and $\vec{p_T^\nu}$ are the electron and the neutrino transverse momenta. The

transverse mass is unaffected by longitudinal Lorentz transformation (boosts) and is only affected at the second order by transverse boosts [36]. However, in order to compute m_T one has to know the transverse momentum of the neutrino, and as mentioned above, it is not directly measured but inferred from the transverse momentum imbalance:

$$\vec{p}^{\,rec} = -\vec{p}^{\,W} = -\vec{p}^{\,e} - \vec{p}^{\,\nu}$$

the momentum of the W is equal and opposite to the momentum of the hadronic recoil. Therefore

$$\vec{p}^{\,\nu} = -\vec{p}^{\,e} - \vec{p}^{\,rec}$$

and for measured quantities (transverse momenta),

$$\vec{p}_T^{\,\nu} = -\vec{p}_T^{\,e} - \vec{p}_T^{\,rec}.$$

The measurement of the recoil momentum is very sensitive to the underlying event, detector noise and pileup effects from previous beam crossings. All these effects lead to the smearing of the Jacobian peak and worsened $m_T(W)$

sensitivity to the W boson mass. To qualitively understand the effect on the transverse W mass Eq. 2.22 could be rewritten as

$$m_T = \sqrt{(|\vec{p}_T^e| + |\vec{p}_T^e + \vec{p}_T^{rec}|)^2 - (\vec{p}_T^e - \vec{p}^{rec} - \vec{p}_T^e)^2} \qquad (2.23)$$

Denoting a component of the recoil momentum on the direction of the electron as $u_{||} = \vec{p}_T^{rec} \cdot \vec{p}_T^e$ and expanding the Eq. 2.23 as a Taylor series in p_T^{rec}/p_T we get the 0th, 1st and 2nd order term for the transverse mass as

$$m_T(0) = 2p_T^e$$
$$m_T(1) = 2p_T^e + u_{||} \qquad\qquad (2.24)$$
$$m_T(2) = 2p_T^e + u_{||} + \frac{(p_T^{rec})^2}{2p_T^e} - \frac{3u_{||}^2}{16p_T^e}$$

In this analysis, we use all three variables (p_T^e, p_T^ν and m_T) to fit for the W mass.

Chapter 3

The Experiment

This chapter provides a brief overview of the subsystems of the Tevatron accelerator and the DØ detector.

3.1 Accelerator

The accelerator consists of several subsystems. The detailed information is available in [37]. Figure 3.1 shows an overview of the accelerator and the detectors location.

The starting point for $p\overline{p}$ collisions is production of H^- ions from a magnetron source. The source produces a 50 mA beam of H^- ions at 18 KeV. These ions are accelerated to 750 KeV by a Cockcroft-Walton accelerator.
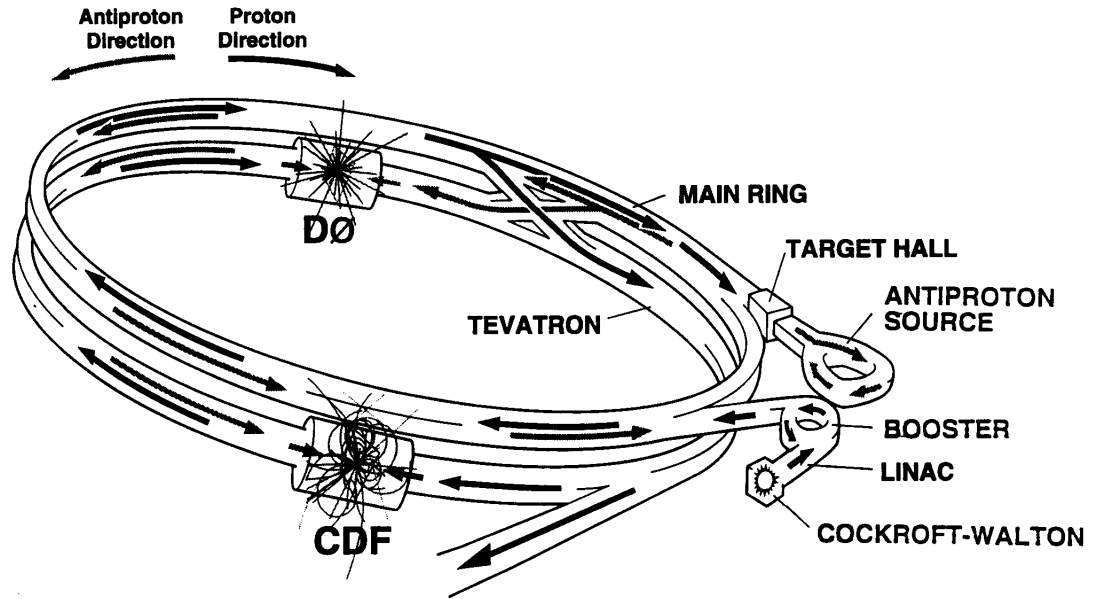
Figure 3.1: Schematic view of the Fermilab accelerator complex.

The ions from the accelerator are fed to the Linear accelerator (LINAC). It is approximately 150 m long. The LINAC is made up of nine drift tubes whose spacing increases along the length of the device. The ions drift inside the tube when an alternating electric field between tubes is in the "deaccelerating" direction and are accelerated when they emerge from the drift tube. The LINAC system accelerates the hydrogen ions to 400 MeV. At the end of the LINAC the ions a stripped of their electrons by passing through a carbon foil. The protons then are injected into the Booster synchotron and accelerated to 8 GeV.

The next two stages are the Main Ring and the Tevatron. Both are synchotrons and are housed in the same tunnel. The Main Ring is made of 1000 conventional copper-coil magnets which are used to increase the protons energy to 150 GeV. The Tevatron has a diameter of approximately 2 km. It uses superconducting magnets immersed in liquid helium cooled to 4.6 K. In normal operations, the protons are accelerated in 6 bunches of about 150×10^9 protons each and 6 bunches of about 50×10^9 antiprotons, counter-rotating in the beam pipe.

If the accelerator is making antiprotons, then the Main Ring only accelerates the protons to 120 GeV. This beam is then extracted and sent to a nickel target. After the interaction the resulting particles contain a fraction of antiprotons which are collected, cooled by stochastic cooling and stored in the antiproton accumulator. When sufficient antiprotons are collected, bunches are reintroduced into the Tevatron in the opposite direction to the protons. The bunches of protons are injected.

When all 12 bunches are injected into the Tevatron, it accelerates them to 900 GeV by a system of 53 MHz radio frequency (RF) cavities. Each RF bucket is 18.8 ns long and the bunch spacing is 186 buckets so that the beam crossing time is 3.5 μs. There are two regions where the beams are

33

allowed to collide, at the CDF and the DØ detector locations. Electrostatic separators prevent the beam from colliding in the other four locations. The luminous region at DØ has $\sigma = 30$ cm in z and its transverse size is about 40 μm. The crossing angle is zero degrees.

3.2 The DØ Detector

The complete description of the DØ Detector can be found in the reference [18]. We give a short description of the subsystems relevant for the present analysis. The detector (Fig. 3.2) consists of three major subsystem: the tracking system, the calorimeters and a magnetic muon spectrometer. The DØ global frame of reference is right-handed with the z axis along the proton beam direction and the y axis pointing upward.

3.2.1 Tracking system

The DØ tracking system consists of Vertex, Central and Forward Drift Chambers and the Transition Radiation detector (Fig. 3.3).

SAMUS PDT
A STATION
B STATION
C STATION

WIDE ANGLE PDT (CM)
A LAYER
B LAYER
C LAYER

WIDE ANGLE PDT (EM)
A LAYER   B LAYER   C LAYER

90°   80°   70°   60°   50°   45°   40°   35°
30°
25°
20°
15°
10°
5°
0°

EF

CF

EF

CENTRAL
DETECTOR

QUAD   QUAD

CALORIMETER

EC   CC   EC

TOROID   CF

SAMUS TOROID

PLATFORM &
ELEC. RACKS

0   5   10 (feet)
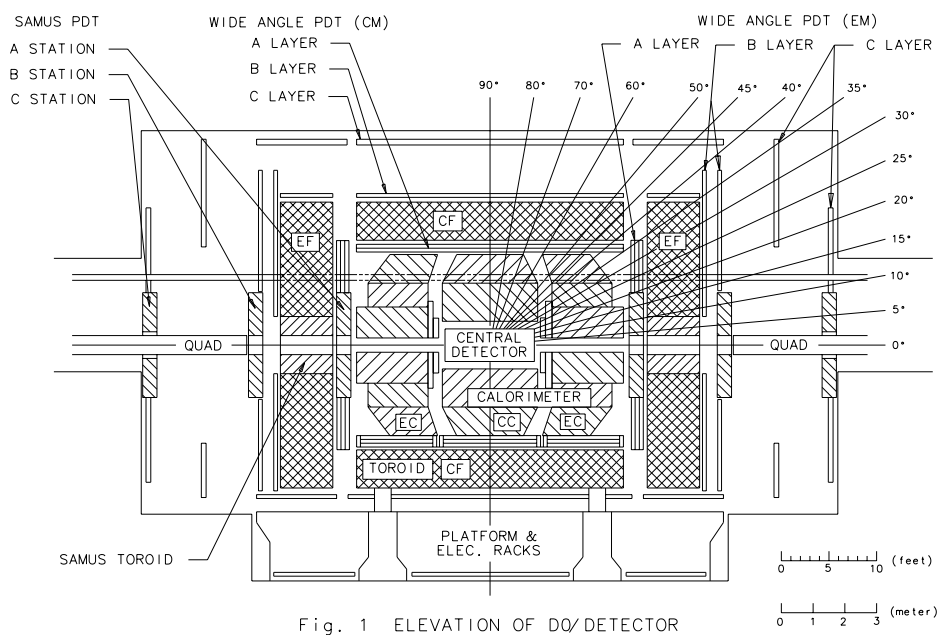
Fig. 1 ELEVATION OF D0/DETECTOR

0   1   2   3 (meter)

Figure 3.2: Major subsystems of the DØ Detector.

35
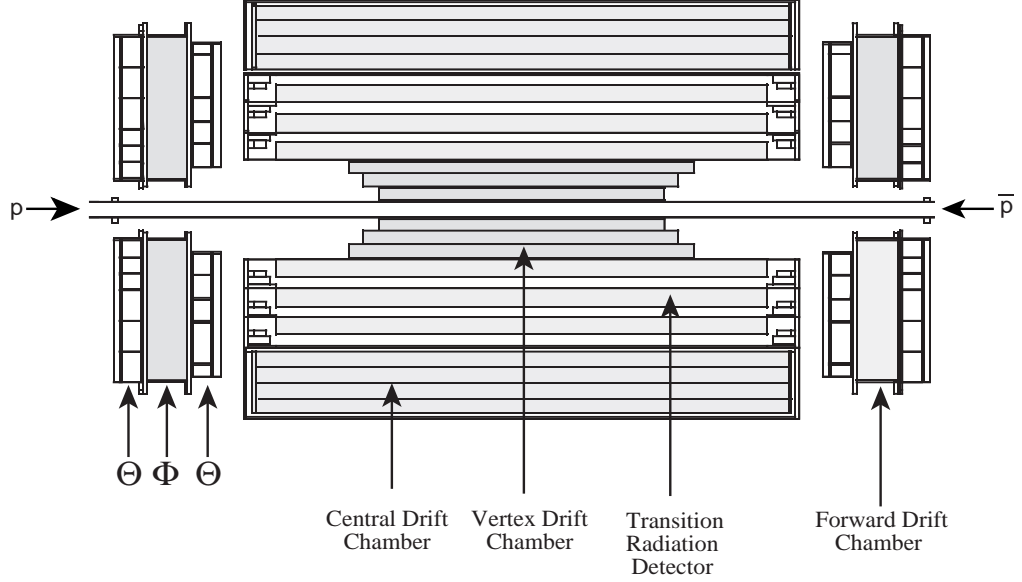
Figure 3.3: DØ Tracking System.

Vertex Drift Chamber (VTX)

Located immediately after the beryllium beam pipe, the vertex drift chamber is used to determine the position of the beam collision spot on a run by run basis in the $r\phi$ view. The beam spot position varies slightly from run to run but negligibly within a run.

The VTX covers the region $|\eta_{\text{det}}| < 1.2$, where η_{det} is a detector pseudo-rapidity, calculated with respect to the nominal vertex at $z = 0$. The VTX consists of three concentric cylindrical layers. Its inner radius is 3.7 cm and the outer is 16.2 cm. An end view of one quadrant is shown in Fig. 3.4.

36
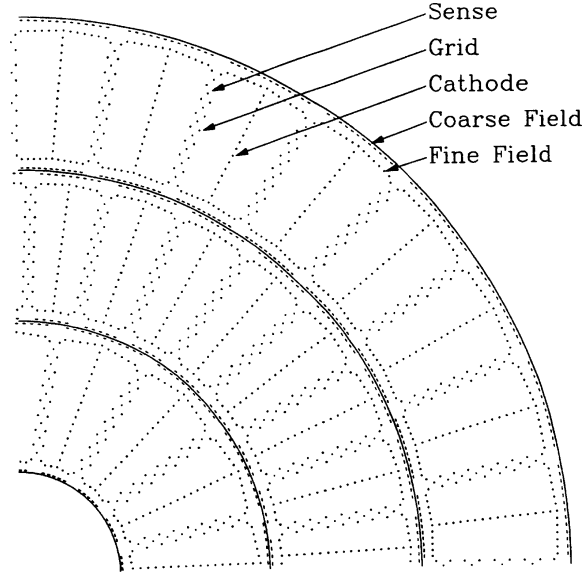
Figure 3.4: $r - \phi$ view of one quadrant of the VTX chamber.

Each layer is divided in azimuth into sectors. Layer 1 consists of 16 sectors and layers 2 and 3 of 32 sectors. In each sector there are 8 sense wires aligned along the beam axis, separated radially by 4.57 mm and staggered by $\pm 100 \mu m$ in the azimuthal direction to help resolve the left-right ambiguity. The sense wires are read out at both ends. Each wires measures a track point in the $r\phi$ view from a drift time and in the rz view via charge division from double sided readout. In measuring electrons, the xy drift time measurement is precise enough to allow track matching in ϕ. However, the VTX rz measurement has not proved to be useful.

37

The Transition Radiation Detector (TRD)

The transition radiation detector is located outside the VTX chambers. It is intended to enhance electron identification efficiency in the central region ($|\eta_{\mathrm{det}}| < 1.0$). The principle of the TRD is that a charged particle crossing the boundary between two media with different dielectric constants radiates photons with probability inversely proportional to the particle mass. Thus electrons, whose mass is 0.511 MeV, radiate much more than any moun or charged hadron. The lightest hadron is the 139.6 MeV pion, and the muon mass is 107 MeV.

The TRD has three separate radiator packages and photon detectors arranged in concentric cylinders beginning outside the VTX and ending to the central drift chamber. Each radiator is made of 393 18 μm thick polypropylene foils immersed in nitrogen gas. Between the radiator and the radiation detector is a gap to provide a buffer so that detector gas is not contaminated with the radiator gas. Figure 3.5 shows a xy view of the TRD. The photons radiated by passing particles typically convert in the 15 mm area outside the mylar window filled with Xe at 1 Atm. The cascade of particles is then amplified in the 8 mm region just inside the 70 μm grid wire. The magnitude and time of arrival of the collected charge is used to distinguish

CROSS-SECTION OF TRD LAYER 1

OUTER CHAMBER SHELL

70μm GRID WIRE

ALUMINIZED MYLAR

8mm

65mm

2mm

15mm

2π/256

4mm

2mm

RADIATOR STACK

N$_2$

CONVERSION
STAGE

30μm ANODE WIRE

23μm MYLAR WINDOWS

100μm POTENTIAL WIRE

HELICAL CATHODE STRIPS
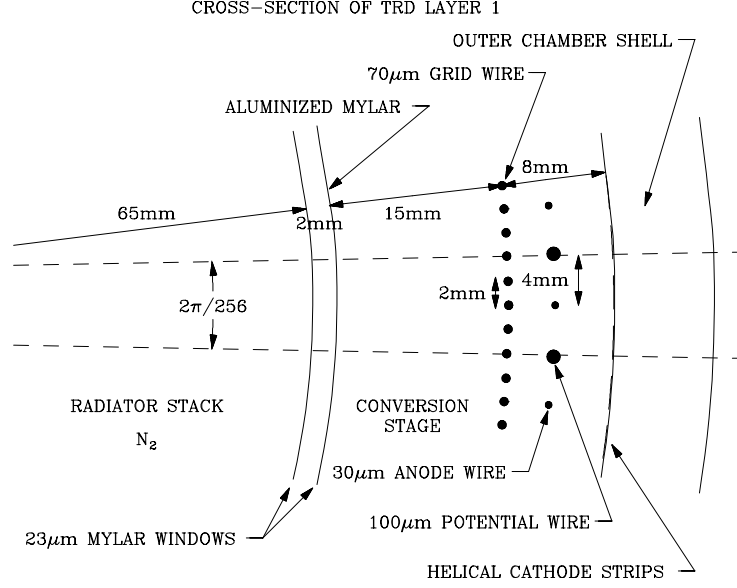
Figure 3.5: A cross section of the TRD.

between electrons and pions or muons.

Central Drift Chamber (CDC)

The central drift chamber consists of four cylindrical layers. It is positioned outside the TRD and just before the central calorimeter. Figure 3.6 shows an end view of a portion of the CDC. The chamber is located radially between 49.5 to 74.5 cm, and is 184 cm long in z. It covers the η_{det} range from -1.2 to 1.2. Each CDC layer is composed of 32 cells in ϕ. The second and fourth layers are offset by half the module angular size with respect to the first and

39

third layers. The maximum drift distance is about 7 cm. There are 7 wires in each cell and appropriate field sharing wires. There are two delay lines embedded in the inner and outer shelves of each cell, seven inner sense wires and 14 grounded potential wires. The sense wires are staggered ± 200 μm in ϕ to resolve left-right ambiguities. The sense wires are read out at one end of the CDC. The $r - \phi$ coordinate is determined by the drift time to the sense wires. The delay line is constructed by winding a coil on a carbon fiber epoxy core and is embedded in the cell wall. A signal is induced upon the delay line by the hit on the nearest sense wire. The inner and outermost sense wires have an additional grounded potential wire to minimize the signal from the next nearest sense wire. The delay lines are read out at both ends. The difference in time arrival of the pulse is used to determine the z coordinate of the hit.

The Forward Drift Chamber (FDC)

There are two forward drift chambers (FDC), located at each end of the CDC, which provide detection of the forward tracks ($1.2 < |\eta_{\text{det}}| < 2.8$).

Each FDC is made of two θ measuring chambers with a ϕ angle measuring chamber in between (Fig. 3.7). The θ chambers are rotated relative to each
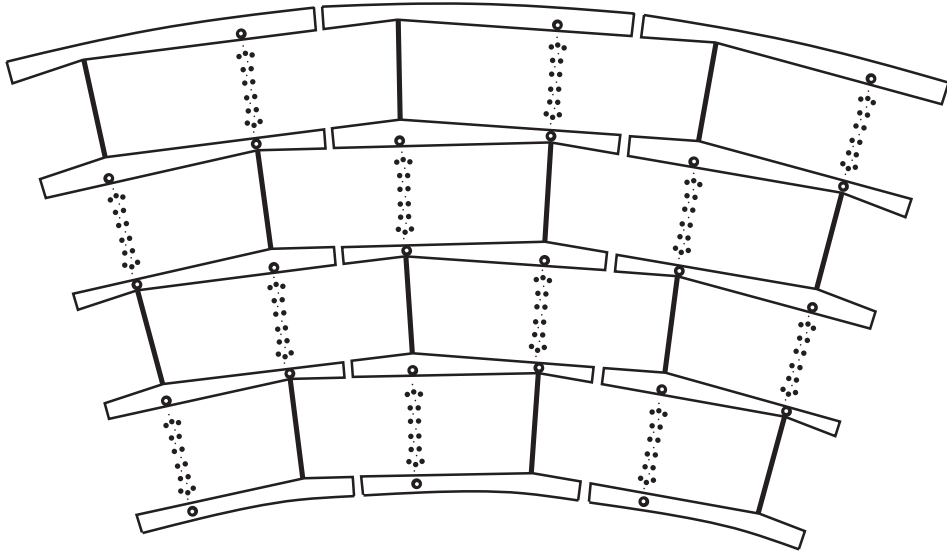
Figure 3.6: $r - \phi$ view of one quadrant of the CDC chamber.
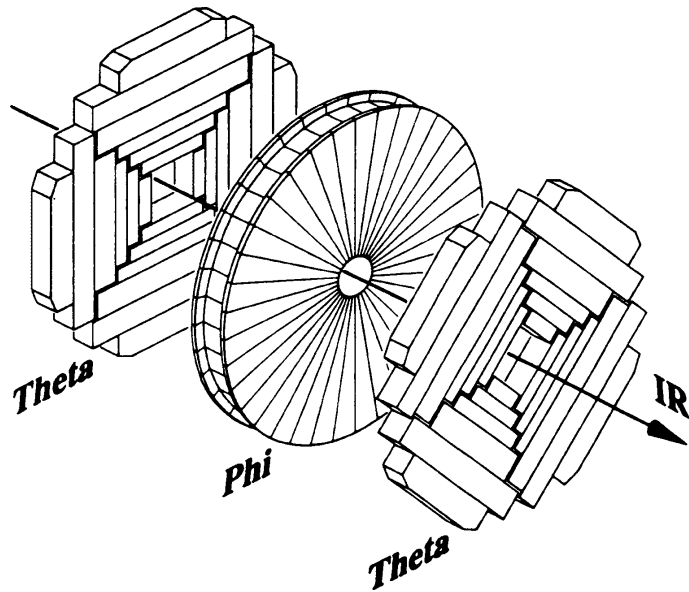
Figure 3.7: View of one of the forward drift chambers.

other by $\frac{\pi}{4}$ radians. The θ chambers have a multirectangular shape. Each is divided into four quadrants, and each quadrant contains six rectangular drift cells. Each drift cell contains eight sense wires (in z) and one delay line, of identical constuction to the CDC, to give local measurement of the orthogonal coordinate. The Φ chamber is divided into 36 azimuthal chambers with wires running radially from the beam line.

3.2.2 Calorimeter

The DØ calorimeter was designed to achieve linear response with energy and good hermeticity. The calorimeter is a uranium-liquid argon sampling calorimeter. The signal is readout from signal boards segmented into pads to localize signals. The pads are ganged in depth to form readout layers. The size of the readout pads varies as a function of η_{det}. Figure 3.8 shows the pseudo-projective geometry of the DØ calorimeter readout cells.

The DØ calorimeters are housed in three different cryostats. The central calorimeter (CC) covers the range of $|\eta_{\text{det}}| < 1$ and two end calorimeters cover the range of $1 \leq \eta_{\text{det}} \leq 4$ (ECS) and $-4 \leq \eta_{\text{det}} \leq -1$ (ECN) (Fig. 3.9).
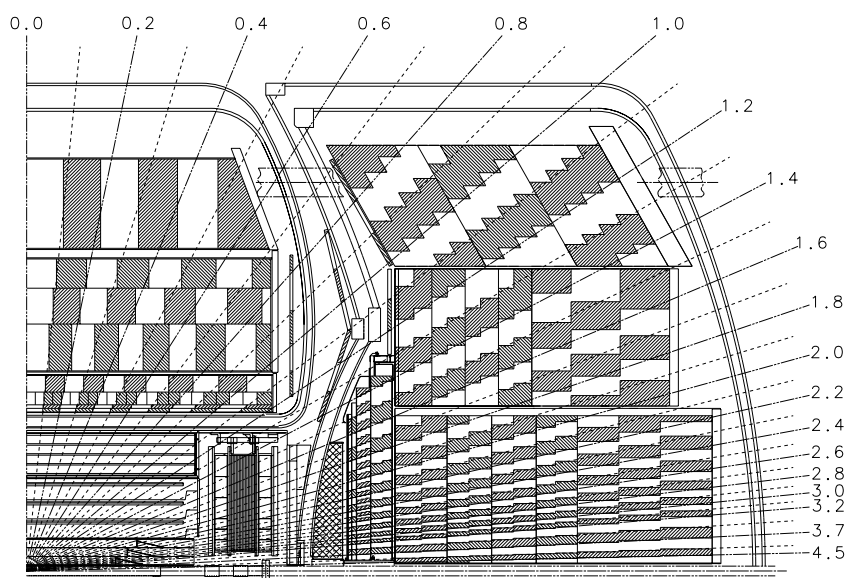
Figure 3.8: One quadrant of the DØ calorimeter. Shading indicates cells forming one readout tower.

Calorimetry principles

When a high energy electron passes through a material with a high atomic number, the primary mechanism by which it loses energy is through Bremsstrahlung, in which a charged particle interacts with the Coulomb field around a nucleus and emits an energetic photon. A high energy photon interacts predominately via e^+e^- pair conversion in the vicinity of a nucleus. The particles emitted in these interactions can themselves undergo Bremsstrahlung or pair production. Thus, an energetic electron or photon passing through a dense material will result in a shower of secondary electrons, positrons, and photons. This process is called an electromagnetic shower. The shower will develop until all the secondaries have sufficiently low energies that ionization becomes a more important energy loss process. The rate at which an incident particle loses energy is a property of the material and is specified in terms of the radiation length X_0, or the length over which an electron's energy diminishes by a factor of e. The DØ electromagnetic calorimeter consists of layers of uranium absorbers causing the development of the EM shower. The space between the plates is filled with the liquid argon. Shower particles passing through the LAr causes the ionization with liberated electrons drifting towards the signal boards located between uranium plates. The signal boards

are biased by a positive voltage of 2.0 kV relative to the absorber plates. The signal induced on all boards over the full shower is proportional to the particles energy. The calorimeter geometry is outlined in the next section.

Central Calorimeter (CC)

The CC is composed of three types of modules. The innermost ring is the electromagnetic calorimeter (CCEM), followed by the fine hadronic calorimeter (CCFH) and the coarse hadronic calorimeter (CCCH). Each calorimeter is subdivided into azimuthal modules. The EM section consists of 32 modules, whereas FH and CH have 16 modules each. Each module extends in z for the full length of the calorimeter. In ϕ there are small gaps between each of the 32 modules. The gaps are about 6 mm wide. The modules consists of several 3 mm thick absorber plates separated by a 2.3 mm gap containing the signal boards (and sometimes readout boards) (Fig. 3.10). The signal boards consists of a copper pad sandwiched between two 0.5 mm thick pieces of G10. The outer surfaces of these boards are coated with a resistive epoxy coating. The coating covers nearly the full width of the board, but is set back by 1/8 of an inch to avoid shorts to the metallic module skin. The gaps between the plates and the boards are filled with liquid argon. The

END CALORIMETER

Outer Hadronic
(Coarse)

Middle Hadronic
(Coarse & Fine)

1m

CENTRAL
CALORIMETER
Electromagnetic

Fine Hadronic

Coarse Hadronic

Inner Hadronic
(Coarse & Fine)

Electromagnetic
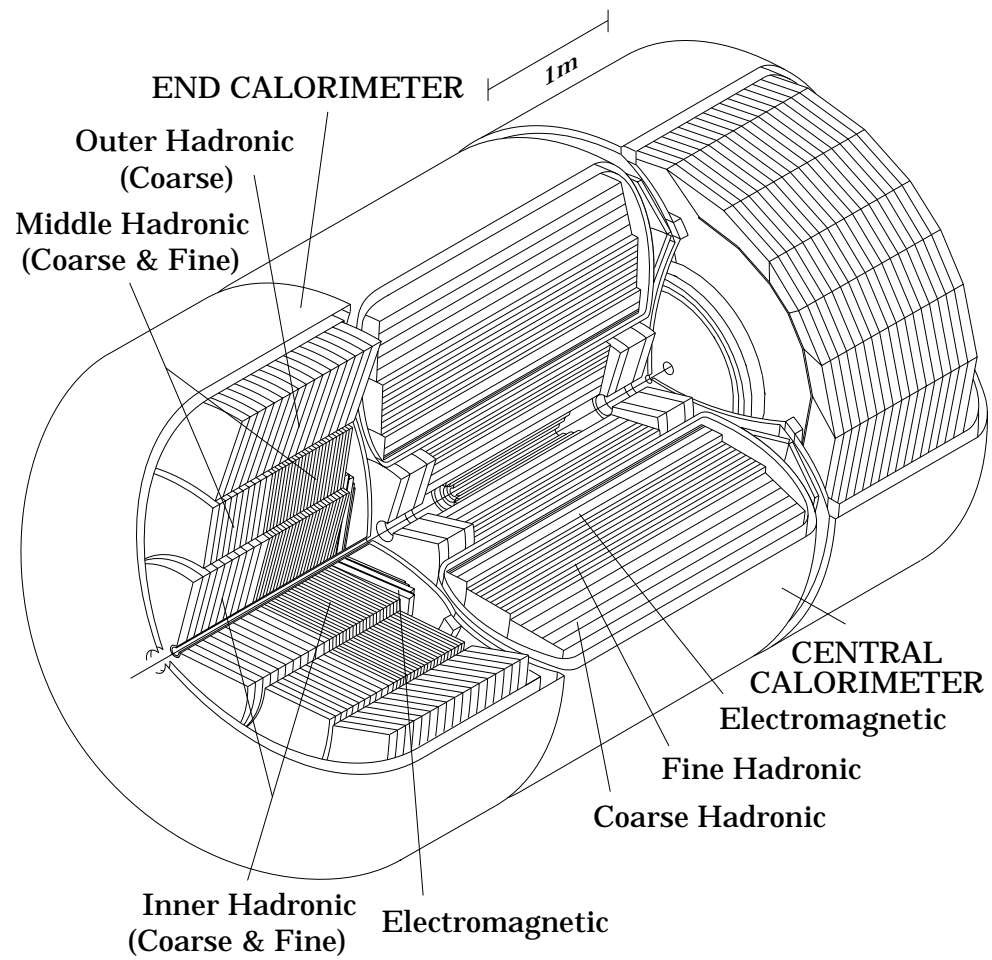
Figure 3.9: A view of the DØ calorimeters.

potential of the absorber plates is kept at ground and the resistive surface of the signal boards are kept at a positive 2000 V. A particle that enters the calorimeter interacts with the absorber plate material and produces a shower of secondary particles. The secondary particles interact electromagnetically with the liquid argon producing electrons and ions. The charge is collected on the resistive coat on the signal boards and the resulting current pulse is capacitively connected to the readout pads. The signal boards are divided into unit cells by cuts on the copper printed circuit pads. Several unit cells are ganged together in depth and read out on a readout board in one of the gaps to make one EM layer. The typical readout cell is shown in Fig. 3.10. There are 4 EM layers labelled EM1 to EM4, formed electronically by ganging signals. The thickness of the layers in radiation length (X_0) are 2,2,7 and 10 respectively. The total thickness of the EM calorimeter is 21 X_0. Typically 20-25 X_0 length are needed to contain an EM shower. In reconstructing electrons and photons, four EM layers and the first layer of the FH section is included in the energy measurement so that logitudinal shower leakage effects are negligible.

The readout cells are organized in pseudo-projective towers. The size of the cell and the tower is 0.1×0.1 in $\eta - \phi$ space. The size of one EM
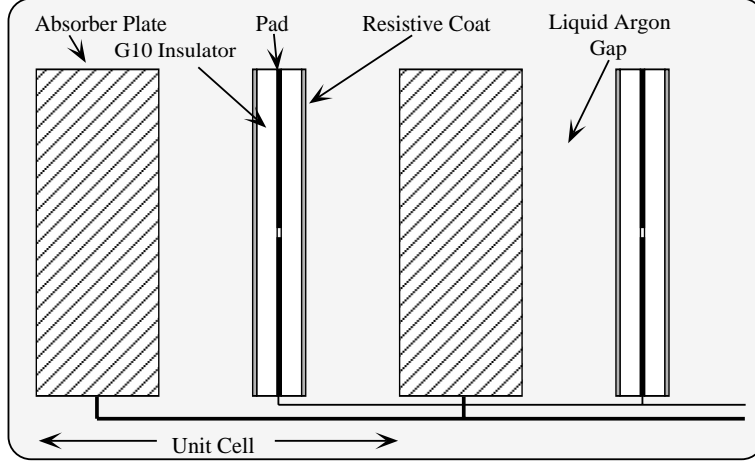
Figure 3.10: Schematic view of a typical readout cell.

module in ϕ is $2\pi/32$ rad, so that signal boards are divided into 2 ϕ pads per module. The EM3 layer is further finely segmented into 0.05×0.05 readout pads. The shower maximum typically occurs in the EM3 layer, so that the finer segmentation allows a better measurement of the shower centroid. It also benefits the shower shape measurements which improves the electron identification efficiency. Module 1 has a ϕ boundary aligned with $\phi = 0$. The EM3 is located at about $r = 90$ cm from the beam line.

The geometry and material distribution of the CCEM near the module boundaries in ϕ is very important in understanding this analysis. I will return to it again later, in the chapter describing the EM response and the resolution

of the CCEM.

The CCFH and CCCH have an $\eta \times \phi$ segmentation of 0.1×0.1. The CCFH has three longitudinal layers of 1.3, 1.0 and 0.9 nuclear interaction length (λ_A). The CCFH plates are fabricated from an uranium-niobium alloy and are 6 mm thick copper. The CCCH has only one layer of $3.2\lambda_A$, and the copper absorber plates are 46.5 mm thick.

End Calorimeter (EC)

The ECs are composed of four types of modules [38]. They are the electromagnetic (ECEM), the inner hadronic (ECIH), the middle hadronic (ECMH), and the outer hadronic (ECOH). Figure 3.9 shows the different module types for the end calorimeter. The ECEM is composed of 4 mm thick circular uranium disks which range from $r = 5.7$ cm to a radius of 84 to 104 cm. The ECEM has four readout layers of 0.3, 2.6, 7.9, and 9.3 X_0. The material in front of the first layer increases the number of radiation lengths in the first layer to about 2. The cell size in η, ϕ space is 0.1×0.1. The third ECEM has a finer $\eta \times \phi$ segmentation than the rest of the layers in the EC of 0.05×0.05. In addition, cells with $|\eta| > 3.2$ have a coarser segmentation of 0.2×0.2. The ECIH modules are cylindrical disks of radii 3.92 to 86 cm. The fine

49

hadronic portion of the ECIH contains four readout layers of $1.1\lambda_A$ each. The plates are made from uranium-niobium alloy. The coarse hadronic is built from stainless steel plates and has a single readout with $4.1\lambda_A$. The ECMH has four fine hadronic sections of $0.9\lambda_A$ and a stainless steel coarse hadronic section of $4.4\lambda_A$. The stainless steel plates of ECOH are tilted 60° with respect to the beam axis.

Calorimeter electronics

The signals induced on the readout pads are pulses with widths on the order of 450 ns compatible to the drift time in the LAr gaps. These signals are led out through four ports in the cryostat to charge sensitive preamplifiers mounted on top of the cryostats. From the preamplifiers, the signals are led to base line subtractor (BLS) modules located in the platform below the detector. The BLS modules perform analog shaping and split signal into two paths. The first path is used for the level-1 calorimeter trigger (see Section 3.2.4). The second path is used for the data readout. The incoming signal is sampled just before the beam crossing and again 2.2 μs later. The difference is presented as a DC voltage which is proportional to the collected charge. This difference is sent to the analog to digital converters (ADC) where, if the

event is accepted by the level-1 trigger the signal is digitized and sent to the level-2 trigger.

Intercryostat detectors

The region between the central and the end calorimeters is covered by scintillator tile detectors. The tiles are read out with photomultiplier tubes (PMTs). The intercryostat detectors (ICDs) are attached to the front surface of the EC. The tiles have a $\eta \times \phi$ segmentation of 0.1×0.1 to match the cell size in the calorimeter. Additionally, rings with two signal boards (single-cell structures without the absorber, called massless gaps) are mounted on the face of the CCCH, the ECMH, and ECOH. The result of including of these tiles is to improve the missing transverse energy ($\not{E}_T$) resolution.

3.2.3 Muon system

High energy muons typically penetrate the calorimeter without significant interactions. The muon detector starts outside the calorimeters (Fig. 3.11). It consists of three layers A,B, and C. Each layer consists of sets of proportional drift tubes which can measure the trajectory of passing muons. The Layer A is separated from the other layers by the large toroidal magnets.
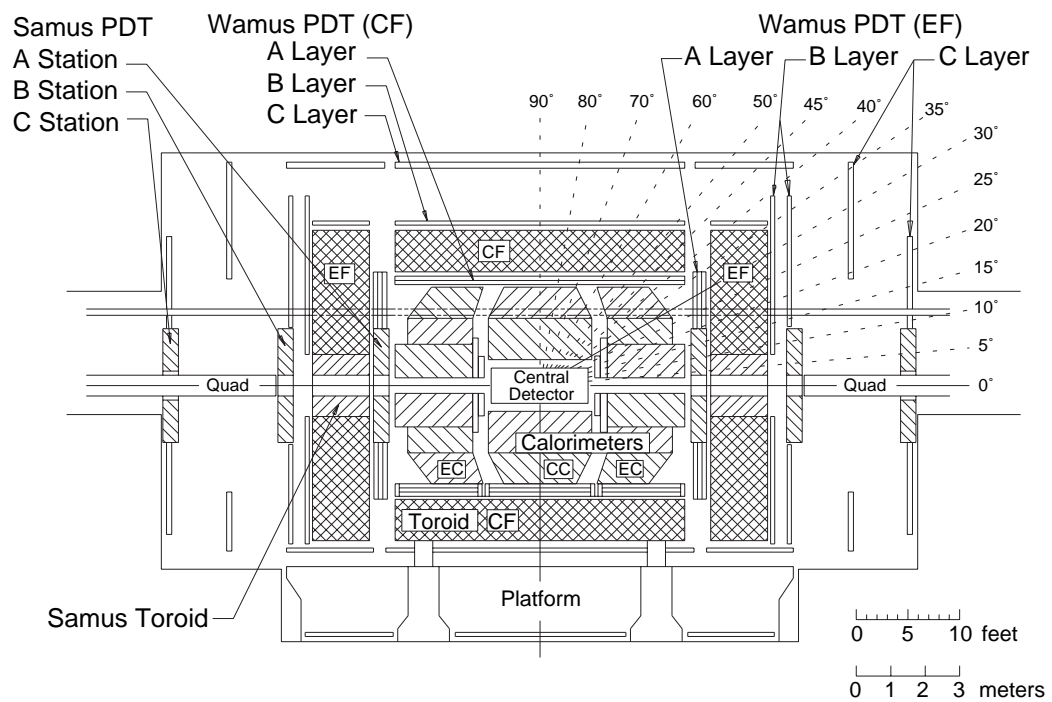
Figure 3.11: Side view of the muon system.

The central toroid (CF) is 109 cm thick and covers a region of $|\eta| < 1$ and two forward toroids (EF) covering $1 < |\eta| < 2.5$. The field magnitude is 1.9 and 2 T respectively. At $\eta = 0$ the minimum muon momentum required to penetrate both the calorimeter and magnet iron is about 3.5 GeV. At higher η, this rises to about 5 GeV. The magnets bend the trajectory of the muons with layer A measuring the trajectory before deflection and layer B and C after deflection. The muon momentum is computed from the angle of deflection. The momentum resolution can be parametrized as

$$(\frac{\delta p}{p})^2 = (0.18)^2 + p^2(\frac{0.01}{\text{GeV}})^2.$$

Since we consider only $W \rightarrow e\nu$ decays in this analysis, the muon detectors have been used only for special calibration runs selecting muons for the drift chamber alignment studies.

3.2.4 Triggering and Readout

At the Tevatron, beam crossings occur at the interaction region at a rate of about 290 kHz. At a luminosity of $5 \times 10^{30}\text{cm}^{-2}\text{s}^{-1}$, an inelastic collision will occur in about 75% of these crossings. However, the processes which

are of the greatest interest are much rarer. Because it is not feasible to record and process data from every crossing, there is a special system of triggers designed to select out only the small fraction of interesting events for permanent storage. The overall layout of the DØ trigger system is shown in Fig. 3.12. It can be conceptually divided into two hierarchical pieces: level-1 (L1) and level-2 (L2). The L1 trigger is a collection of dedicated hardware processors which operate on a coarse subset of the event data. Most of L1 trigger decisions can be made within the 3.5 μs interval between beam crossings, permitting operation without deadtime. However, some triggers, called level-1.5 (L1.5) triggers, may require more time. The goal of the L1 trigger is to reduce the event rate from the beam crossing frequency of 290 kHz to a rate of 200-300 Hz (events per second).

Once an event has been accepted by L1, the complete event is digitized and the data transferred to one of 48 L2 nodes. These are general purpose computers which process events in parallel. They perform a fast reconstruction of the event, and can use general software filters to decide whether or not an event should be kept. If L2 passes an event, it is transferred to the host system, where it is permamently recorded on magnetic tape.

The L1 trigger has two main components: muon and calorimeter. For
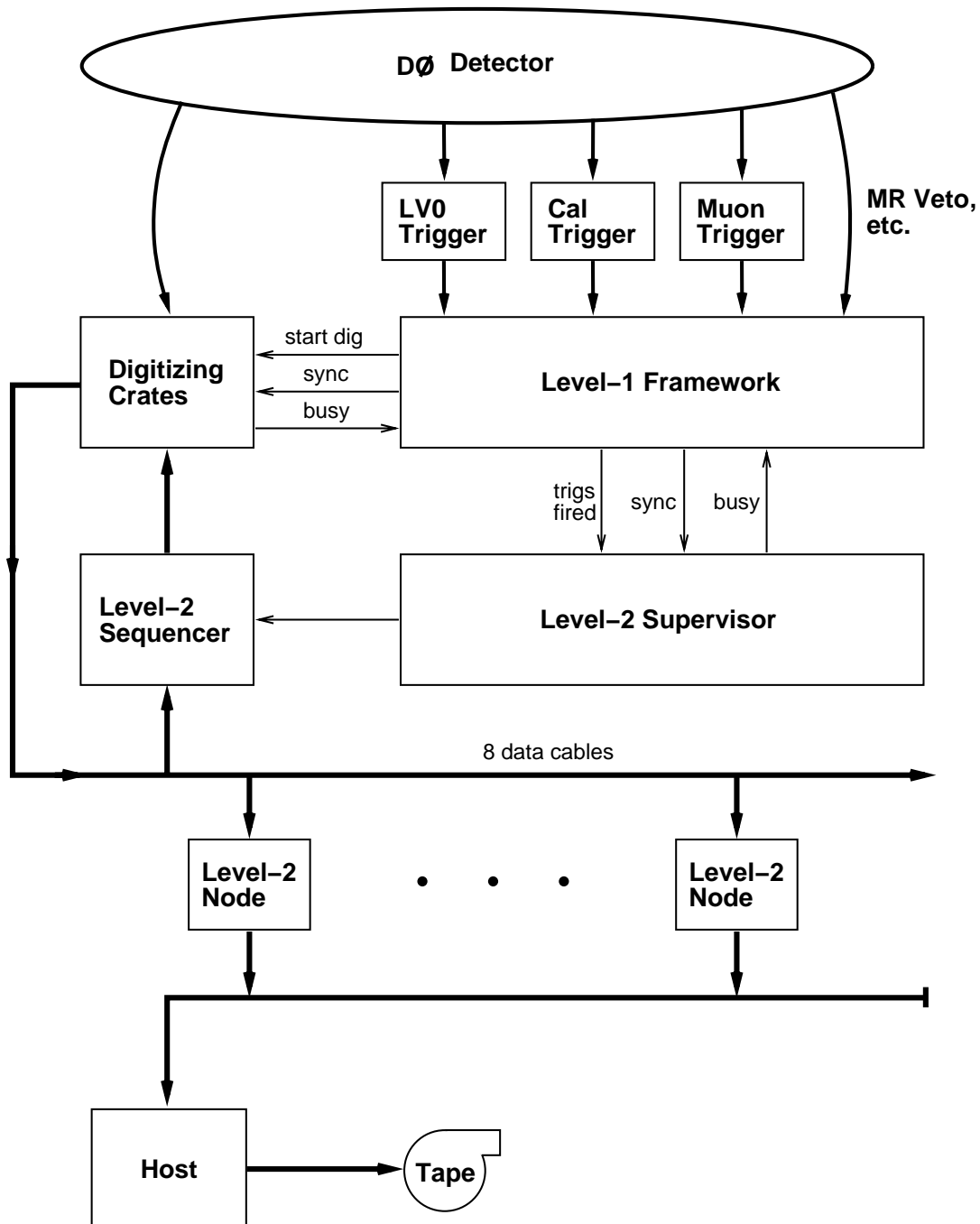
Figure 3.12: Overall layout of the DØ triggering system

more information on the muon triggers see reference [39]. The L1 calorimeter trigger is a hardware trigger which uses information taken from the BLS cards. The trigger tower, the region on which decisions are based, is a 0.2×0.2 region in $\eta \times \phi$ space for η up to 4. The electromagnetic and fine hadronic energy for each tower is available for the decision making. The energy of the EM tower is $E_{em} = \sum_i E_i(\text{EM})$ and hadronic tower is $E_{had} = \sum_i E_i(\text{FH})$. If the level 1 criteria is satisfied then an event is passed directly to L2 or sent on to L1.5 for further selection (depending on the specific trigger).

L1.5 uses the same information as L1 but clusters the two highest energy adjacent towers into a single object. These towers can only be clustered along the η or ϕ direction. For level 1.5 the transverse energy $E_T^{\text{L1.5}}$ and the EM fraction $f_{em}^{\text{L1.5}}$ are calculated from Eqs. 3.1,3.2

$$E_T^{\text{L1.5}} = \sum_{i=1}^{2} E_i(\text{EM}) \sin \Theta_i \tag{3.1}$$

$$f_{em}^{\text{L1.5}} = \sum_{i=1}^{2} \frac{E_i(\text{EM})}{E_i(\text{EM}) + E_i(\text{Had})} \tag{3.2}$$

where Θ_i is the polar angle defined by the Z vertex and the center of the ith 2×2 tower. If $E_T^{\text{L1.5}}$ and $f_{em}^{\text{L1.5}}$ pass certain threshold the event is sent to L2.

The level 2 trigger is a software trigger with information for the entire

56

detector available to make trigger decisions. L2 runs software tools to identify electrons, muons, jets and etc. This information is then used to generate L2 decisions. The energy of the electron candidate is taken from the 0.3×0.3 $\eta \times \phi$ region centered about the highest E_T tower from Level 1. An electron is identified from the transverse shower shape, electromagnetic fraction, and isolation. The isolation f_{iso}^{L2} condition is given by

$$f_{iso}^{L2} = \frac{E(0.4) - E}{E} < 0.15$$

where $E(0.4)$ is the energy in a cone of radius $R = \sqrt{\Delta\eta^2 + \Delta\phi^2}$ equal to 0.4 and E is the energy of the electron candidate. Events are written to tape at 2-4 Hz. The events are then written to tapes and sent to offline reconstruction farm where a reconstruction program produces the variables used in the physics analysis.

For this analysis we used following triggers. Z boson event candidates were selected with EM_2_MED Level 1 trigger, which requires two electromagnetic objects with $E_T > 7$ GeV. The Level 2 trigger, EM2_EIS2_HI, selects two isolated electromagnetic objects with $E_T > 20$ GeV.

For a W boson candidate we used Level 1 trigger, EM_1_HIGH, which

requires one electromagnetic object with $E_T > 10$ GeV and the Level 2 trigger, EM1_EISTRKCC_MS, requires one isolated electromagnetic object with the $E_T > 20$ GeV and $\rlap{/}{E}_T > 15$ GeV.

For the W background studies we also use EM1_ELE_MON level 2 triggers which is identical to the EM1_EISTRKCC_MS but does not have any requirement on the $\rlap{/}{E}_T$.

3.2.5 The reconstruction program

The raw data which comes from the detector is given in terms of quantities such as digitized counts in a calorimeter cell, counts per time bin for a tracking chamber wire, and so on. The program that analyzes the raw data and identifies some physical objects such as leptons and jets is called DØ RECO, the reconstruction program.

The program can be divided into three major phases. First is the unpacking and hit finding, in which the raw data is converted into energy deposits in calorimeter cells, or pulses on tracking chambers and wires of definite energy and spatial location. Then tracking and clustering algorithms are run, where hits pattern are analyzed to identify tracks in the tracking chambers and clusters in the calorimeter. The last step is particle identification, in

which information from all parts of the detector is combined to produce a collection of objects which are candidates for being jets, electrons, or muons. The criteria used for identifying these candidates are made quite loose so that they have a high efficiency, but there will also be a large background. When performing a subsequent analysis, one typically makes much tighter selection cuts on the reconstructed objects.

Chapter 4

Overview of the measurement

4.1 Introduction

In this chapter I present the W mass analysis using CC electrons detected at the edge of the EM modules. The CC calorimeter consists of 32 modules which divide the $r - \phi$ view into 32 segments. All previous precision measurement analyses, and W mass analyses [6, 7, 8] in particular, have rejected the electron if it passes within about 10% of the azimuthal module width of the modules' edges, because the EM response and resolution there differs from the rest of the module. The points in Fig. 4.1 show the Z boson mass distribution if one of the electrons is the "edge" region. In this distribution

there is an excess of events below 80 GeV which can not be described by the simple Gaussian response and resolution relevant to non-edge electron. If the Z mass distribution of the non-edge electrons is subtracted from the edge electron distribution then the difference can be fit with a Gaussian. On one hand, it means that in a large number of events the "edge" electron has the same EM response as the non-edge electron. On the other hand, in the rest of the events the calorimeter EM response is lower. Figure 4.1b suggests that the EM response of the "edge" electron can be parametrized by the sum of two Gaussians. The parameters of the first Gaussian are identical to non-edge electron ones, and parameters of the second Gaussian have to be determined. The model introduces three new parameters: the center of the second Gaussian or EM scale of the "edge" electron, the width of the second Gaussian or resolution of the "edge" electron, and the fraction of events when an "edge" electron showers according to the second Gaussian. In this dissertation I first investigate the accuracy and relevance of the double Gaussian parametrization and then describe a method to determine new parameters. I also check other aspects of the W mass analysis which can be affected by a new EM response and resolution function. The background fraction has to be checked because the "edge" electron's EM shower shape might differ

from that of non-edge electron's, which would alter the relative efficiencies for electrons and jets. The electron's energy correction due to the underlying event energy flow under the electron EM towers, and the dependence of the electron identification efficiency on the component of recoil momentum parallel to the electron's direction ($U_\parallel$ efficiency) might be different for "edge" and non-edge electrons. The correction to the electron's energy due to a radiative photon, when the radiated photon is within the "edge" part of the module and inside the coalesence radius, is studied too.

I then proceed to W mass fitting using the same approach as in previous analyses [6, 7, 8]. Using W events with electrons at the edge of the EM module, I fit the W boson transverse mass (m_t), the electron's $p_t(e)$ and missing $p_t(\nu)$ spectra with the W mass as a free parameter. I also use Z boson events in which one of the electrons is at the "edge" and the other is in the CC or EC calorimeter to additionally constrain the EM scale and resolution parameters of the non-edge CC and the EC electrons. Finally, I combine the new W mass measurement with all previous DØ W boson mass measurements properly taking into account the correlations between the different measurements. I find reduced uncertainties on the EM scale and resolution of the non-edge CC and EC electrons, because of the additional

constraints. The combined W mass uncertainty is reduced from 91 to 84 MeV. The major part of the reduction comes from the smaller uncertainty of the EM scale and resolution of the CC/EC electrons, rather than the additional W event statistics, because the edge EM parameters have a large uncertainty and the W mass is more sensitive to them than to non-edge EM scale and resolution.

4.2 The experiment strategy

The W boson mass is measured by fitting measured distributions of the W boson decay products (e and ν) kinematic quantities such as transverse mass, the electron transverse momentum and $\not{E}_T$ with the predicted distributions. To calculate the predicted distributions we use a fast Monte Carlo (MC) program specifically written for this purpose. We call this Monte Carlo program the CMS Monte Carlo after the Columbia-Michigan State groups that developed it. The CMS MC is divided into two logical parts. First is the generation of the kinematic quantities of the W and Z decay products and the second is simulating the detector response. The generation of the kinematic distributions is based on the theoretical calculations presented in Chapter 2.
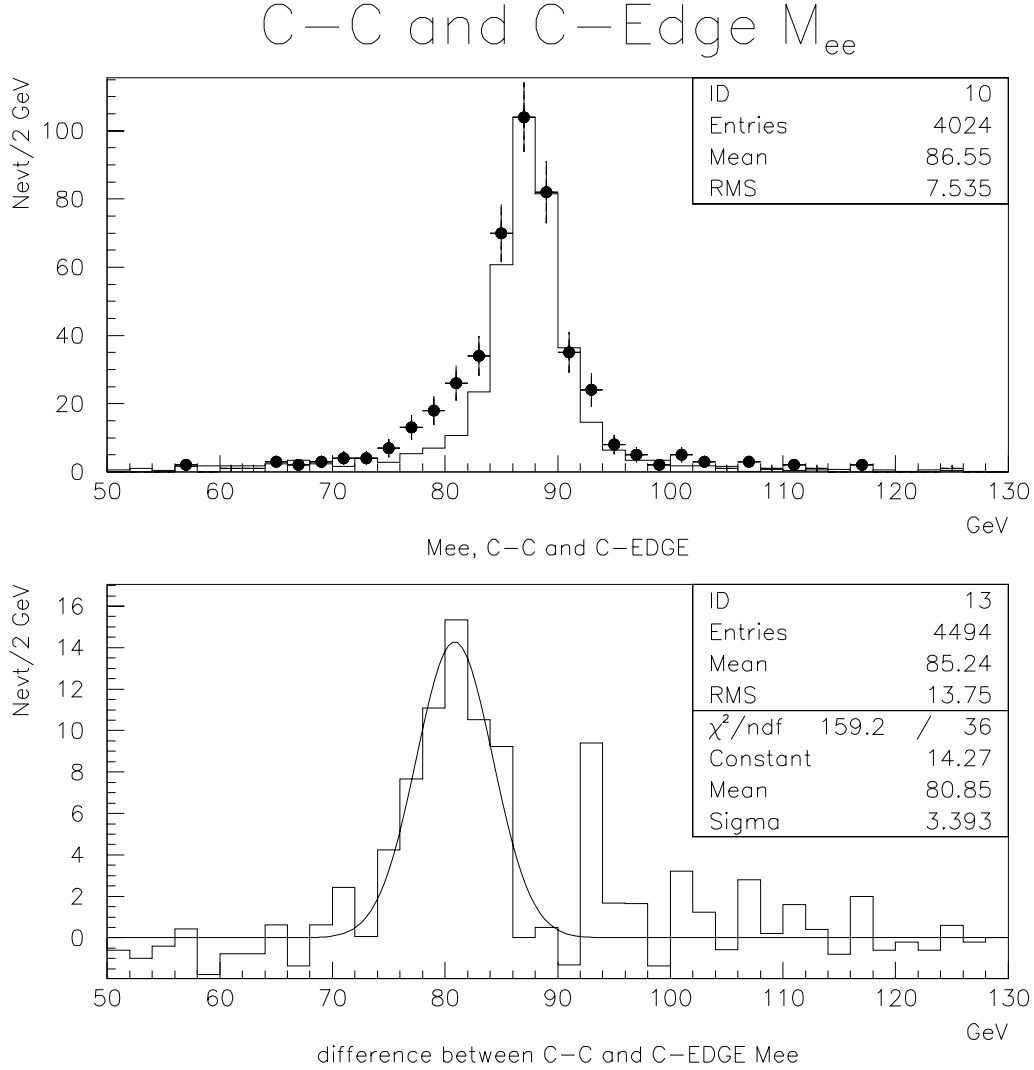
Figure 4.1: Dielectron invariant mass. Z mass from non-edge CC events (solid line) and from Edge-CC events (points). The Edge-CC distribution is scaled so that number of events in the peak bin is the same as in the CC-CC distribution. The figure at the bottom is the difference of the Edge-CC and CC-CC histograms on a bin-to-bin basis, fitted with a Gaussian.

I will describe the process of generating the W boson though the same description applies to the Z as well. The CMS is an event generator where each event has a unit weight. First, the W boson mass is chosen according to the Breit-Wigner distribution skewed by the parton luminosity (Eq. 2.14). Then we choose a sea-sea or sea-valence/valence-valence quark interaction scenario. If sea-sea is chosen the W's positive and negative helicity is generated with the equal probability. Otherwise, the W^- has a negative helicity and W^+ a positive helicity. Then CMS generates the W transverse momentum and rapidity according to Eq. 2.15. The $p_T - y$ distribution is PDF dependent and we use the MRST PDF function in the simulation. Finally the momentum of decay electron and neutrino is generated in the center of mass system of reference and boosted along the W momentum direction. The vertex z position is generated according to the Gaussian distribution with the width of 27 cm. Other processes, such as radiative decays and $W \rightarrow \tau\nu$ decays are simulated as well.

The second phase is the simulation of the detector response. The electron position and momentum, the recoil energy are modified to take the detector resolution into account. The step is called "smearing". The smearing function is parametrized by a few parameters. Many of them have been de-

termined in the previous analysis [7]; some of them are determined in this analysis.

We use Z events to define many of the detector response parameters. The mass of the Z boson is known to a high precision. Using the CMS MC we generated invariant mass distributions and compare them with the mass distribution of the selected Z events. We then tune the Monte Carlo detector response parameters. We choose a parameter or set of parameters to be tuned and generate a set of invariant Z mass distributions for different values of these parameters. We call the generated Z mass distributions the templates. We perform a maximum likelihood fit to the data Z mass distribution and choose the value of the fit parameter corresponding to the template which yielded the smallest negative log likelihood.

Once we developed the adequate description of the detector, we perform the fit for the W boson mass. We generate templates – transverse mass, the electron p_T, and neutrino p_T distrubtions at different W boson mass M_W. For each kind of the templates (m_T, p_T^e, or p_T^ν template) we choose the M_W corresponding to the template that has the smallest negative log likelihood with the data distribution. We then combined the three found M_W into a single measurement taking the correlations into account.

Chapter 5

Triggers and data selection

5.1 Triggers

In this analysis we used events that passed one of the three triggers. The Z boson candidates were selected with EM_2_MED Level 1 trigger, which requires two electromagnetic objects with $E_T > 7$ GeV. The candidate is then passed to the Level 1.5 trigger requiring that one of the objects pass an $E_T > 10$ GeV cut. The Level 2 trigger,EM2_EIS2_HI, selects two isolated electromagnetic objects with $E_T > 20$ GeV. Refer to the Section 3.2.4 for the definition of the electron isolation and EM cluster used in level 2 trigger.

The first trigger requirement for a W boson candidate was a Level 1

69

trigger, EM_1_HIGH, which requires one electromagnetic object with $E_T >$ 10 GeV. Level 1.5 then required the Level 1 object pass an E_T cut of 15 GeV. The Level 2 trigger, EM1_EISTRKCC_MS, requires one isolated electromagnetic object with the $E_T > 20$ GeV and $\not{E}_T > 15$ GeV.

For the W background studies we also use EM1_ELE_MON level 2 triggers which is identical to the EM1_EISTRKCC_MS but does not have any requirement on the $\not{E}_T$.

5.2   Measured quantities

Electron energy

An electron is defined to be a deposition of energy in the electromagnetic portion of the calorimeter along with an associated track in the tracking chambers. The electron energy cluster is required to pass some loose shower shape cuts and an electromagnetic fraction cut. The energy of the electron is the sum of the cells in a $\eta \times \phi$ region equal to 0.5×0.5 in the first five layers (EM1,2,3,4, and FH1) of the calorimeter, This region is called a 5×5

window. The electron centroid $\vec{x}_c = (X_{cal}, Y_{cal}, Z_{cal})$ is calculated from

$$\vec{x}_c = \frac{\sum_i w_i \vec{x}_i}{\sum_i w_i}$$

where the sum runs over all the EM3 cells of the electron and $\vec{x}_i$ is the location of the center of the ith cell. The weights are given by

$$w_i = \max\left(0, w_0 + \ln\left(\frac{E_i}{E}\right)\right)$$

and E_i is the energy in the ith cell in EM3, E is the energy of the cluster, and the global weight w_0 is chosen to minimize the resolution.

Quality variables

In this analysis we used four quantities defining the quality of electron iden-
tification. The EM fraction is defined as a fraction of the electron energy deposited in the electromagnetic calorimeter to the total electron energy

$$f_{EM} = \frac{E_{EM}}{E_{EM} + E_{HAD}}.$$

E_{EM} is a sum over four EM layers and E_{HAD} is a sum over all hadronic layers.

The isolation is defined as

$$ISO = \frac{E(0.4) - E^{EM}(0.2)}{E^{EM}(0.2)}$$

$E(R)$ is an electron's energy collected in the four EM layers and all hadronic layers within a cone with radius $R = \sqrt{\Delta\phi^2 + \Delta\eta^2}$. The electron's energy from the EM layers only is $E^{EM}(R)$.

The covariance matrix χ^2 measures how consistent the shower shape is to that expected from an electron. If one has a set of N measurements of a given type, and each measurement consists of M variables $x^i = (x_1^i, ..., x_M^i)$ one can form the covariance matrix from the outer products

$$V = \frac{1}{N} \sum_{i=1}^{N} (x^i - \overline{x})^T (x^i - \overline{x})$$

where $\overline{x}$ is the mean value of the N measurements. The H-matrix is the inverse of this covariance matrix $H = V^{-1}$. For any subsequent measurement y one can define a χ^2 which describes how likely is that y came from the same

sample as the x:

$$\chi^2 = (y - \overline{x}) H (y - \overline{x})^T.$$

The Monte Carlo electrons used to generate the matrix were tuned on the test beam electrons. There are 41 variables used in the covariance matrix: the energy fraction in EM1,2,4, the log of the total energy, energy in each 6×6 grid centered around the highest energy cell in EM3, and the vertex position divided by the RMS of vertex distribution.

The 4-variable likelihood ratio λ_4 combines the information in EM fraction, χ^2, track-EM cluster match quality variables and the track dE/dx.

The track - EM cluster match significance σ_{trk} determines how well the track found in the CDC matches with electron EM cluster and is defined as

$$\sigma_{\text{trk}}^2 = (\frac{\Delta s}{\delta s})^2 + (\frac{\Delta z}{\delta z})^2$$

where Δs and Δz are the differences between extrapolated to the third EM layer track position (found in the CDC) and the EM cluster centroid in the azimuthal (Δs) and in the z (Δz) directions.

Vertex position

The (X_{vtx}, Y_{vtx}) of the vertex position is known very well due to the fact that the cross-section of the beam is very small, of the order of 50 μm, and varies only slightly over the length of a data run. The Z_{vtx} is determined on an event to event basis from the electron EM centroid and the center of gravity (COG) of the associated track. The vertex is given by

$$Z_{vtx} = Z_{trk} - \frac{R_{trk}}{R_{EMclus} - R_{trk}}(Z_{EMclus} - Z_{trk})$$

where $R_a = \sqrt{(X_a - X_{vtx})^2 + (Y_a - Y_{vtx})^2}$ and $a = trk, clus$.

5.3 Offline Data selection

To select W and Z boson event candidates I applied the same cuts as in the standard CC and EC analyses [7, 8] except for the cut on electron impact distance from the module edge.

The central electrons are required to have:

- $|\eta_{\text{det}}| < 1.1$

- H-matrix $\chi^2 < 100$

- track match significance $\sigma_{track} < 5$ ([40])

- EM fraction > 0.90 ([41])

- electron isolation < 0.15 ([42])

- $|Z_{EMclus}| < 108$ cm

- $|Z_{trk}| < 80$ cm (Z_{trk} is CDC center of gravity)

- The electron has to be within 10% (0.02 rad) in ϕ of either CC module edge to be called an edge electron, and outside the 10% range to be called central. I use the electron's track center-of-gravity in the CDC and the vertex position (x,y) to determine the ϕ angle.

The EC electron has to satisfy:

- $1.5 < |\eta_{\mathrm{det}}| < 2.5$

- H-matrix $\chi^2 < 200$

- track match significance $\sigma_{track} < 10$ ([43])

- EM fraction > 0.90

- 4-variable likelihood variable $\lambda_4 < 4.0$ ([8])

The edge W boson CC sample consists of events that:

- RECO versions in the range [12.13:12.25]

- EM1_EISTRKCC_MS trigger

- neither MICRO_BLANK [44] nor MRBS_LOSS [45] conditions should

  be true.

- $p_t(e) > 25$ GeV

- $p_t(\nu) > 25$ GeV

- $p_t(W) < 15$ GeV

- $|Z_{vtx}| < 100$ cm

I selected the Z sample by requiring:

- RECO version [12.13:12.25]

- EM2_EIS2_HI trigger

- $p_t(e) > 25$ GeV (CC), $p_t(e) > 30$ GeV (EC)

- $60 < m_{ee} < 120$ GeV

- $|Z_{vtx}| < 100$ cm

76

- both electrons are required to have a track if any of the electrons is from the edge. If both electrons are from non-edge region, only one of them was required to have a track.

I will follow the following convention. I will denote a non-edge CC electron by C, an edge CC electron by $\widetilde{C}$, and an EC electron by E. Thus $\widetilde{C}$-C stands for the Z dielectron sample with one non-edge and one edge electron; C-C means both non-edge electrons and so on.

I identify three new Z samples (in addition to old Z samples C-C, E-C and E-E). The $\widetilde{C}$-C sample is the sample with only one of the two electrons at the CC module edge. The $\widetilde{C}$-E sample has the CC electron at the edge and the other in the EC, and in the $\widetilde{C}$-$\widetilde{C}$ sample both electrons are edge electrons.

The number of selected W and Z events are listed in Table 5.1. Edge regions take up about 20% of the CCEM surface, but the number of $\widetilde{C}$ W candidates is only about 14% of the C W events. One of the reasons is that the CDC consists of four concentric layers with 32 cells in each of them. The sense wires are located in the middle of a cell. The middle of the cell in any layer is aligned with the edge of a cell in the adjacent layer. The EM module edges in ϕ are aligned with the middle of the CDC cells in some

77

layers, and the edge of the cells in other layers. So the edge electrons cross
CDC cells either close to the middle or the edge of the cell, which leads to
some inefficiencies in track reconstruction. Figure 5.1 shows the effect of the
CDC track match cut on the edge distance distribution. Another reason is
that the electron identification efficiency is lower in the edge region.

	$\tilde{\text{C}}$ W	$\tilde{\text{C}}$-C Z	$\tilde{\text{C}}$-$\tilde{\text{C}}$ Z	$\tilde{\text{C}}$-E Z
Events	3853	470	47	154

	C-E Z	E-E Z	E W	C-C Z	C W
Events	1265	422	11089	2012	27675

Table 5.1: Number of W and Z candidate events.

78
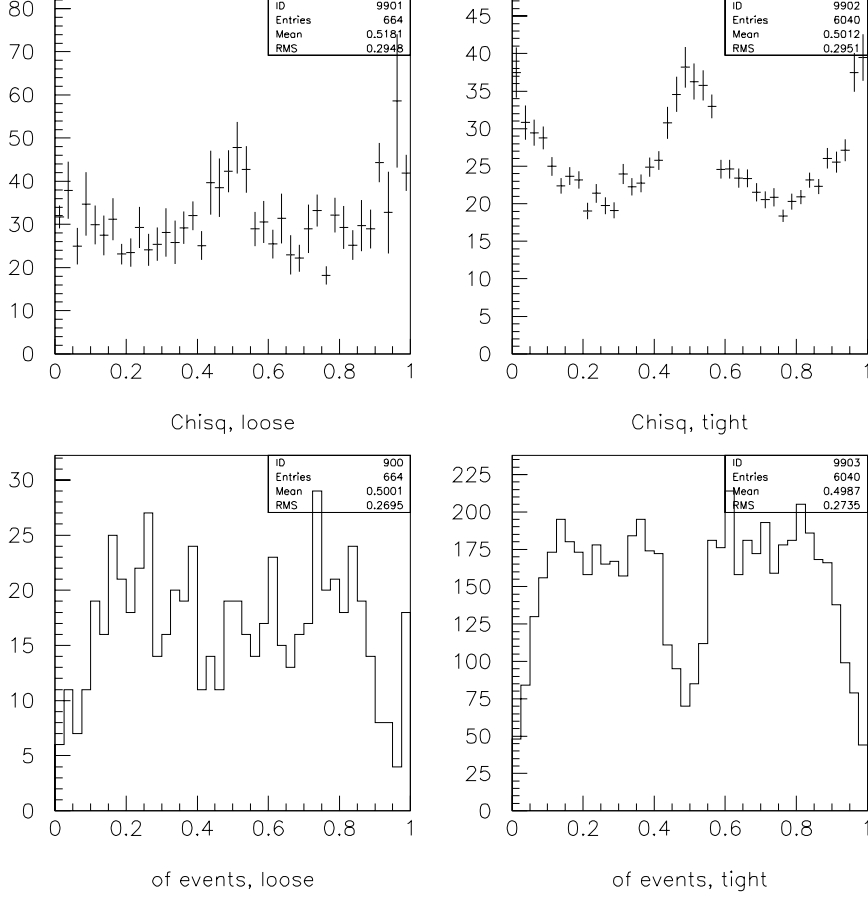
Figure 5.1: Z $\widetilde{C}$-C events. The upper two plots show an average electron's H-matrix χ^2 as a function of the distance to the module edge. $d = 0.5$ corresponds to the middle of the CCEM module. Electrons on the left plot do not have a track matched to the EM cluster (loose electrons) and electrons on the right plot were required to have a matched ($\sigma_{\text{track}} < 5$) track. Two lower plots show the distribution of number of loose (left figure) and tight (right figure) electrons in the Z $\widetilde{C}$-C sample across the CCEM module. CDC sense wires in two CDC layers and chamber walls in the other two layers are aligned in ϕ with EM module edges. It causes the dip in number of events with tight electrons in the middle and edges of the module.

Chapter 6

Backgrounds

6.1 Z boson background

The background to the $\widetilde{\text{C}}$-C Z events consists of QCD multijet events with jets faking the electrons. Other sources of the background (such as $t\bar{t} \rightarrow WWb\bar{b}$ or W+jet production with the jet misidentified as an electron) are negligible. To estimate the background shape I applied the Z selection cuts described above to the data sample but instead of electron quality cuts I used anti-electron cuts to select "bad" electrons. A "bad" electron has:

- H-matrix $\chi^2 > 100$

- no matched track ($\sigma_{track} > 5.0$)

- electron isolation < 0.15 (same as for the "good" electron cut)

- EM fraction > 0.90 (same as for the "good" electron cut)

The edge electron was required to be the "bad" electron and the non-edge CC electron was required to be the "good" electron (satisfying normal electron quality cuts described in the data selection section). In Fig. 6.1, I plot the dielectron invariant mass of the selected events. I fit the distribution with an exponential function $e^{-Am_{ee}}$, giving a logarithmic slope $A = -0.064 \pm 0.022$ GeV. For comparison I also plot the exponential function with the slope determined for the "bad" electron C-C events (the slope is -0.038 GeV). We see that two exponents are statistically different, and I used the slope determined from "bad" electron $\widetilde{C}$-C sample as the QCD background shape in this analysis.

The fraction of background events is determined from an invariant dielectron mass distribution fit (Section 7.2.3) for the Z boson mass. The fraction (in the $70 < M_{ee} < 110$ GeV range) is calculated to be :

$$f^Z_{QCD} = (3.7 \pm 3.6)\%$$

For comparison, the QCD background for C-C Z's is $(2.2 \pm 1.3)\%$.

I also study the shape of the QCD background to $\widetilde{\text{C}}$-E events. I select the sample of dielectron events with the edge electron satisfying "bad" electron quality cuts and the EC electron satisfying "good" electron cuts. I plot the dielectron invariant mass distribution in Fig. 6.2. The shape of the background M_{ee} distributions from "bad" electron C-E and "bad" electron $\widetilde{\text{C}}$-E samples are close to each other. I fit the "bad" electron C-E M_{ee} with a fourth degree polynomial function. The fit $\chi^2 = 20/15$. I then fit the "bad" electron $\widetilde{\text{C}}$-E M_{ee} with the "bad" electron C-E parametrization function and allow only overall normalization factor to vary. The "bad" electron C-E parametrization fits the "bad" electron $\widetilde{\text{C}}$-E data well with $\chi^2 = 8.6/18$. Therefore, I took the Z QCD background shape for the $\widetilde{\text{C}}$-E sample to be the same as for C-E Z's and use the appropriate fitted normalization.

6.2 W boson background

The background to the edge W events has three components. The first is the QCD multijet background in which a jet fakes an electron. The second is Z events in which the non-edge electron is poorly reconstructed and contributes to the $\not{E}_T$. The last is the $W \rightarrow \tau\nu_\tau$ process. The $W \rightarrow \tau\nu_\tau$ events are

QCD Background in Z sample

Top figure (ID 1):

ID	1
Entries	154
Mean	78.33
RMS	14.01
χ^2/ndf	12.88 / 12
Constant	7.057
Slope	$-0.6362E-01$

invariant mass cc−cc 1cr

Bottom figure (ID 2):

ID	2
Entries	154
Mean	78.33
RMS	14.01
χ^2/ndf	15.93 / 12
Constant	4.863
Slope	$-0.3800E-01$

invariant mass cc−cc 1cr
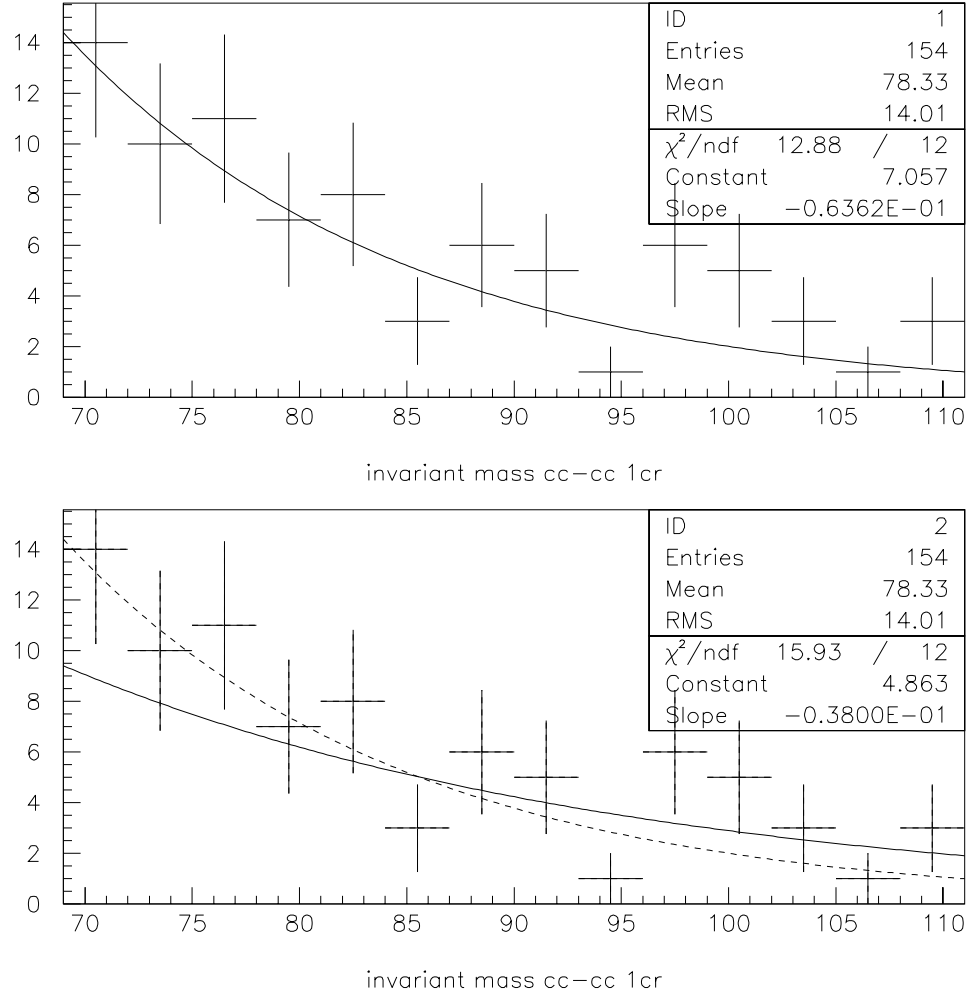
Figure 6.1: QCD Z background. The points are the data dielectron invariant mass from the "bad" electron $\widetilde{C}$-C sample. The solid line on the top figure is the fit with the exponential function. The dotted line on the bottom figure is the same fit and solid line is the exponential function with the "bad" electron C-C QCD background parameters.
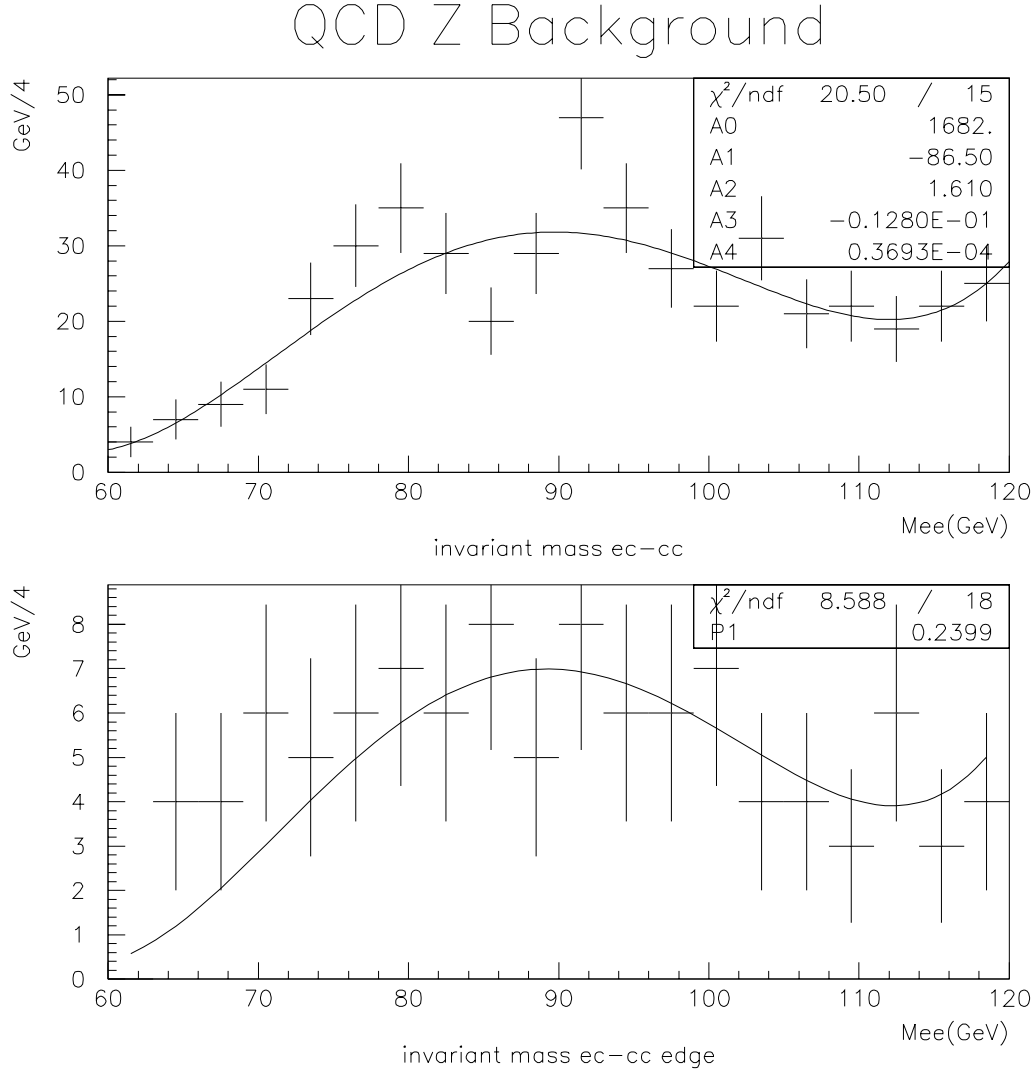
Figure 6.2: QCD Z background. The points are the data dielectron invariant mass from the "bad" electron C-E (top figure) and $\tilde{C}$-E (bottom figure) samples. The solid line on the top figure is the fit with a fourth degree polynomial function. The solid line on the bottom figure is the fit with the above polynomial function when all its parameters are fixed to the above values and only the total normalization is a fit parameter.

included in the CMS Monte Carlo [19, 20] used to generate large samples of W events.

The fraction of the background from Z events is the same as in non-edge W events [7], because the poorly reconstructed electron in both cases is the non-edge electron:

$$f_{Z \to ee}^{W} = (0.42 \pm 0.08) \ \%$$

The shape of the background could be different because of the edge electron EM resolution. However, if I set $f_{Z \to ee}^{W}$ to zero, the fitted W mass changes by 10 MeV, and a possible variation of background shape would lead to an even smaller effect. In the analysis, I assumed the background shape to be the same as in non-edge W's.

In order to estimate the QCD background I employed the same technique as in the W EC analysis [8]. I used a sample of low $\not{E}_T$ events selected with EM1_ELE_MON trigger. The sample is dominated by QCD multijet events at low $\not{E}_T$. I applied the same W candidate cuts as descibed above except that $\not{E}_T$ had to be less than 15 GeV, and also I applied the anti-electron selection criteria (no track match is required and H-matrix $\chi^2 > 100$) to select "bad" electrons and normal electron quality cuts to select "good" electrons. I then take the ratio of the number of jets passing the "bad" electron cuts to the

the number of jets passing the "good" electron cuts. We don't expect this ratio to depend on $\not{E}_T$ of the event so we assume that the ratio in the W sample is the same. I selected 610 "bad" electron candidates and 509 "good" electrons which infers that the ratio between "bad" and "good" electrons in the W sample is $r_{\frac{bad}{good}} = \frac{610}{509} = 1.20$. I also selected 69 "bad" electron events in the W sample which gives $\frac{69}{r_{\frac{bad}{good}}} = 58$ QCD background events in the W sample. It means that the fraction of QCD background events in the signal sample is

$$f_{QCD}^W = \frac{58}{3853} = (1.5 \pm 0.2) \ \%$$

This can be compared to $f_{QCD}^W = (1.3 \pm 0.2)\%$ for non-edge W's. In Figs. 6.3, 6.4, 6.5 I plot the transverse mass, electron E_T, and $\not{E}_T$ distributions of QCD background events ("bad" electron events) for edge and non-edge electron events. The distributions are statistically indistinguishable and I assumed that the QCD background shape for edge electron events is the same as used in the non-edge W analysis.

QCD W Background
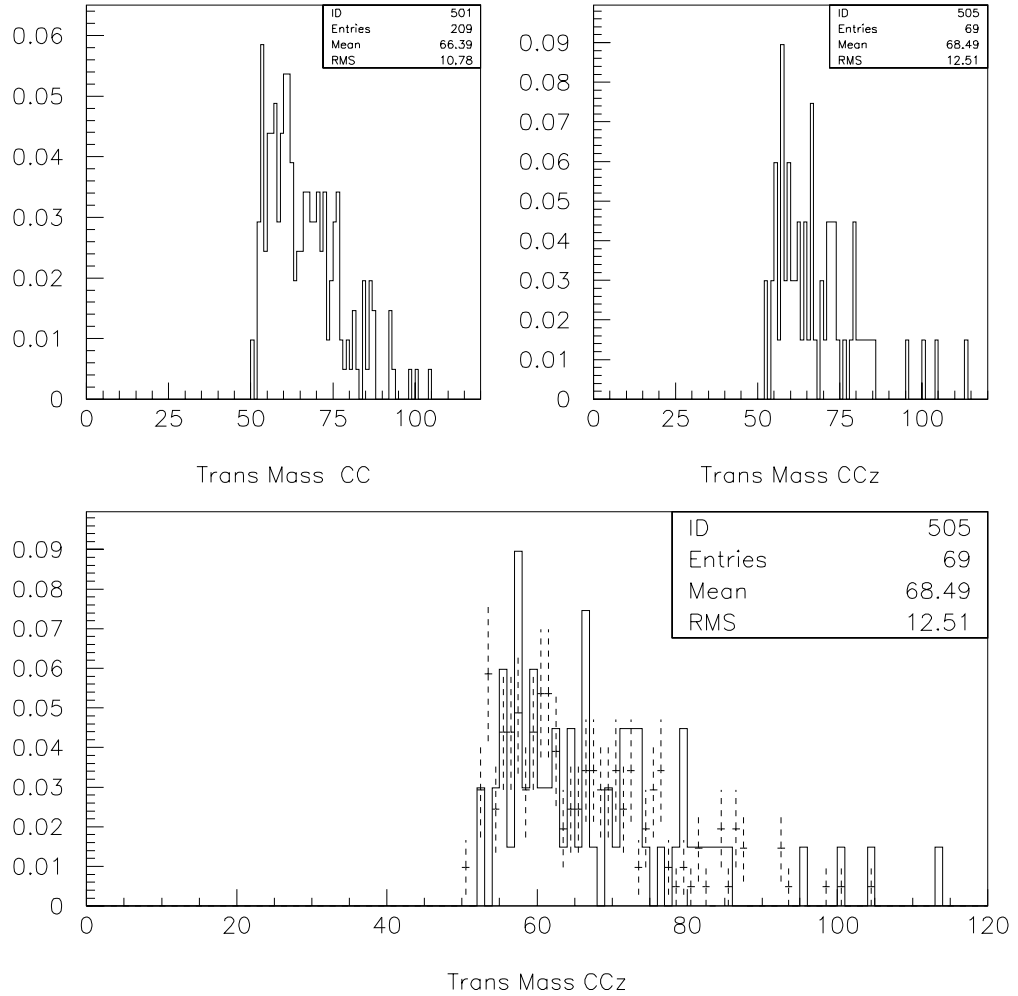
Figure 6.3: QCD W background. The top left figure is the transverse mass from the W sample for non-edge "bad" electron events. The top right figure is for edge "bad" electron events. The figure at the bottom is both distributions (solid line is the edge "bad" electrons and points are the non-edge "bad" electrons) normalized by the number of events.
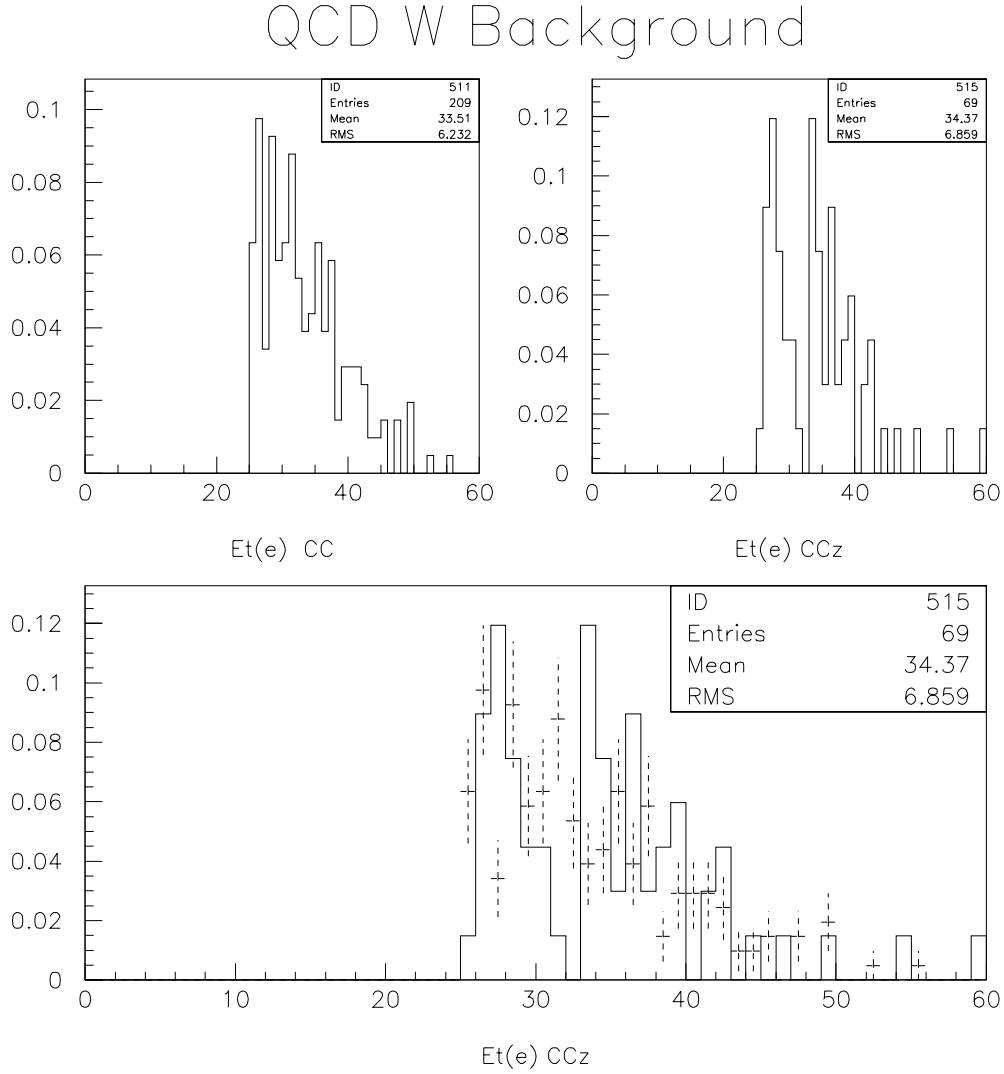
Figure 6.4: QCD W background. The top left figure is the electron E_T from the W sample for non-edge "bad" electron events. The top right figure is E_T for edge "bad" electron events. The figure at the bottom is both distributions (solid line is the edge "bad" electrons and points are from non-edge "bad" electron) normalized by the number of events.
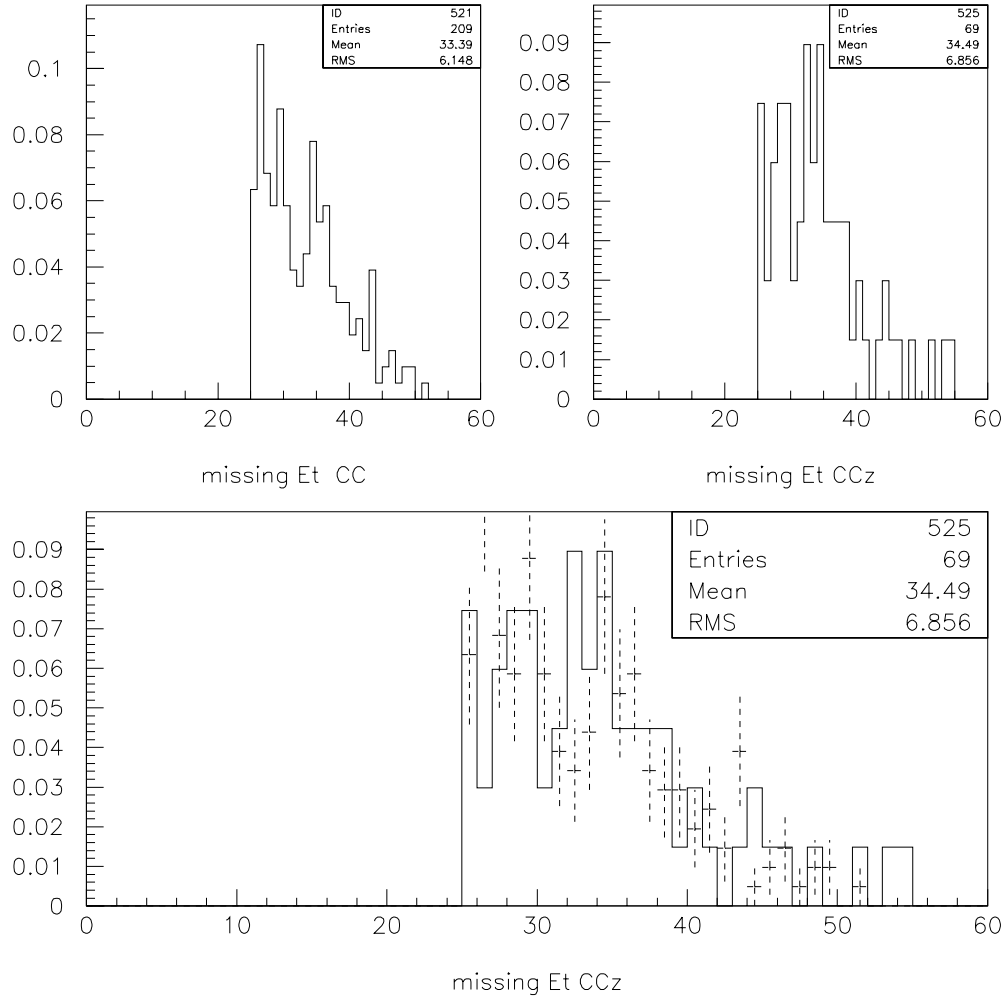
Figure 6.5: QCD W background. The top left figure is the $\not{E}_T$ from the W sample for non-edge "bad" electron events. The top right figure is $\not{E}_T$ for edge "bad" electron events. The figure at the bottom is both distributions (solid line is the edge "bad" electrons and points are for non-edge "bad" electrons) normalized by the number of events.

Chapter 7

Energy Response and

consistency checks

7.1   Introduction

This chapter addresses the critical issue of the edge electron energy response and resolution. Edge electrons have significantly different energy response and resolution than non-edge electrons. In this chapter I first explain the energy response model for the edge electrons, then describe the determination of the response and resolution functions. At the end I examine cross-checks that demonstrate the validity of their determination.

91

7.2 EM Energy Response

7.2.1 Difference between Edge and Non-Edge EM response

Due to statistical nature of the development of the EM shower, the amount of energy deposited in the calorimeter by the same energy particles fluctuates and can be described by a statistical distribution. The EM response is thus a function relating energy of the charged particle passing through the EM calorimeter to the energy measured by the EM calorimeter on average. The function describing the shape of this distribution is called EM resolution.

The EM response of the CC calorimeter differs for edge electrons and non-edge electrons. I will discuss it in more detail later in this section, but the presence of non-instrumented material and distorted electric field at the module edges contribute to the difference. For non-edge electrons we describe the EM response as a linear function of the "true" electron energy, using an EM scale, α_{CC}, and an EM offset, δ_{CC}:

$$E_e^{meas} = \alpha_{CC}\, E_e^{true} + \delta_{CC} \qquad (7.1)$$

The energy resolution is described by sampling (s_{CC}), constant (c_{CC}), and noise terms (N_{CC}) as following:

$$\sigma_E/E = s_{CC}/\sqrt{E} \oplus c_{CC} \oplus N_{CC}/E, \qquad (7.2)$$

where $\oplus$ means addition in quadrature. I first tried to use the same kind of parametrization for the edge electron and wrote the EM response and resolution in terms of α_{edge} and c_{edge}:

$$E_e^{meas} = \alpha_{edge}\, E_e^{true} + \delta_{edge}$$

$$\sigma_E/E = s_{edge}/\sqrt{E} \oplus c_{edge} \oplus N_{CC}/E$$

where $s_{edge} = s_{CC} = 0.13$ and is taken from the test beam studies [47]. The c, s and N terms represent errors due to the energy loss in the non-instrumented material, sampling fluctuations and noise contributions respectively. The EM scale α_{edge} was determined by fitting the Z ($\tilde{\text{C}}$-C) dielectron mass distribution using a set of CMS generated templates at different Z boson masses. The EM scale α_{edge} is ratio of the best fit Z mass to the LEP value of 91.1869 GeV.

In Fig. 7.1 I show the EM scale versus distance to the EM module edge.

The events in each bin were selected from the Z event sample by requiring one and only one electron to be in that bin and the other to be elsewhere, but not in the edge bin. This way each subsample resembles the edge sample, where only one of the electrons is at the edge and the other is not. Events with both electrons in the same bin were not used at all because these events would require a separate set of MC templates (with both electrons energies depending on the bin's EM scale). The figure shows a clear difference between edge and non-edge electrons. The EM scale for edge events is about 2% lower than for non-edge events. Even when we use this modified edge EM scale to generate the W mass templates, the fitted edge W mass is significantly different from the non-edge W mass (Fig. 7.1). The non-edge events do not have any clear dependence on the distance to the edge.

The EM resolution shows a similar kind of behavior. In Fig. 7.2, I plot the EM resolution for single electron σ_{EM} in bins of the electron's distance to the edge. I extract it from a Breit-Wigner convoluted with a Gaussian fit to the Z mass distribution. The edge bin's σ_{edge} is significantly higher than the average non-edge σ_{CC}.

The observed difference of the EM response of the edge electron indicates a need for a correction. The EM scale (α_{edge}) and EM resolution constant
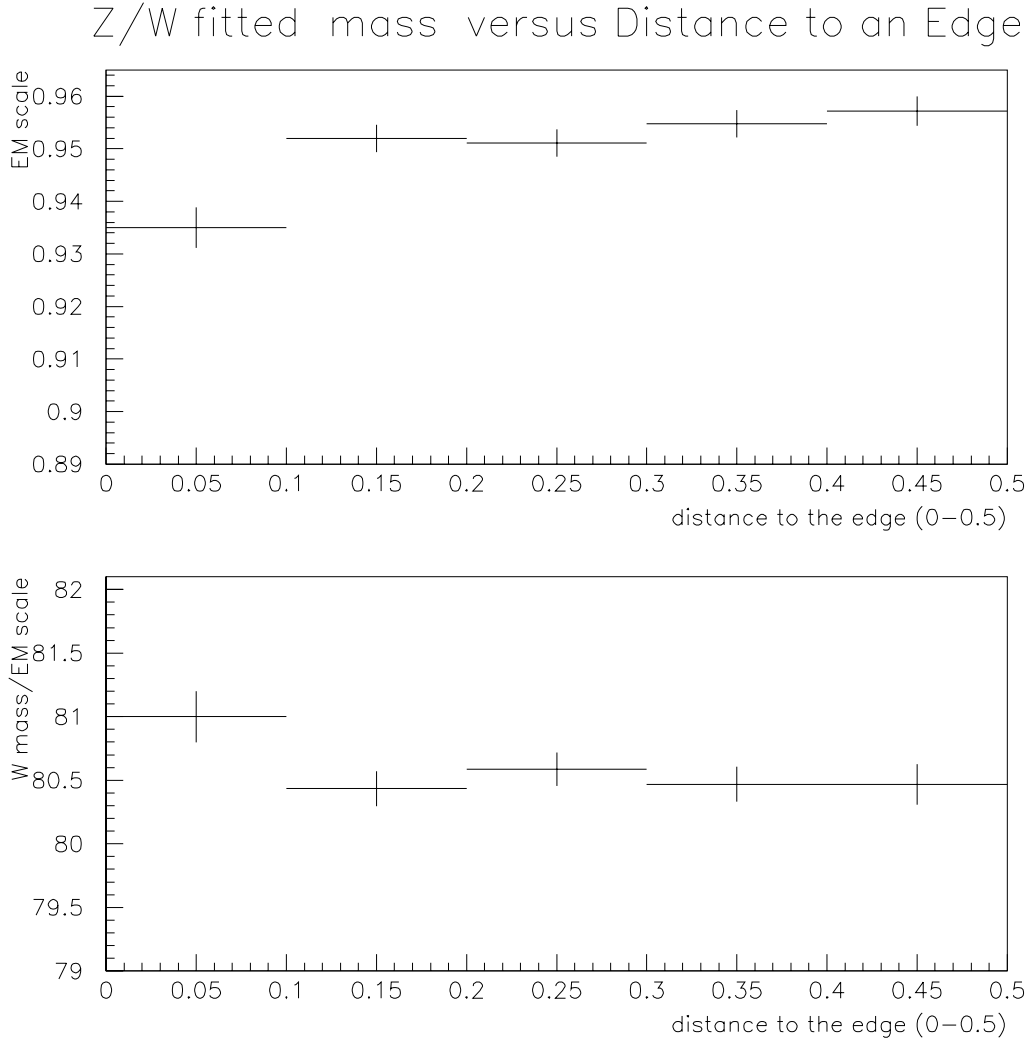
Figure 7.1: Variation of the EM scale across the CCEM module. The distance $d = 0.5$ corresponds to the middle of the CC module. The scales were obtained from the fit of the Z mass distribution with the CMS mass templates, using EM resolution function from Eq. 7.2. The figure at the bottom is the fitted W boson mass. The EM scales from the top figure were used to generate MC W mass templates.
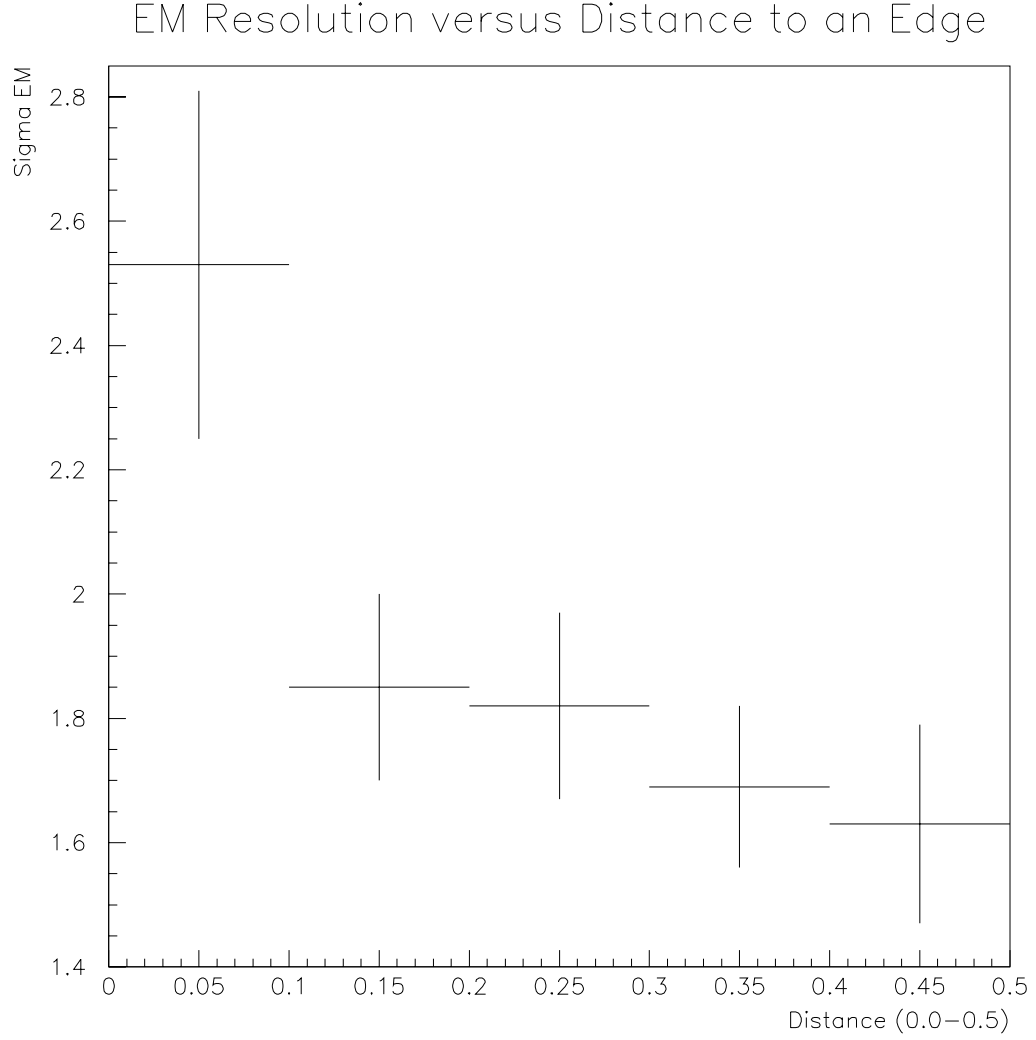
Figure 7.2: EM resolution across the CCEM module. The plotted EM resolution σ_{EM} is extracted from the fit to the Z event sample broken into bins of the electron's distance to the CC module edge. I fit with a Breit-Wigner function convoluted with a single Gaussian. The σ_{EM} was the fit parameter. The Z events in the edge bin were fit with the single Gaussian too.

W/Z Fit, EDGE

ID	150
Entries	470
Mean	86.61
RMS	6.865

$\chi^2 = 29.523/19$

$M_z = 91.003 +- 0.184$

M(ee) CC

ID	150
Entries	3853
Mean	68.66
RMS	8.875

$\chi^2 = 56.535/29$

$M_w = 80.603 +- 0.201$

MT(ev) CC
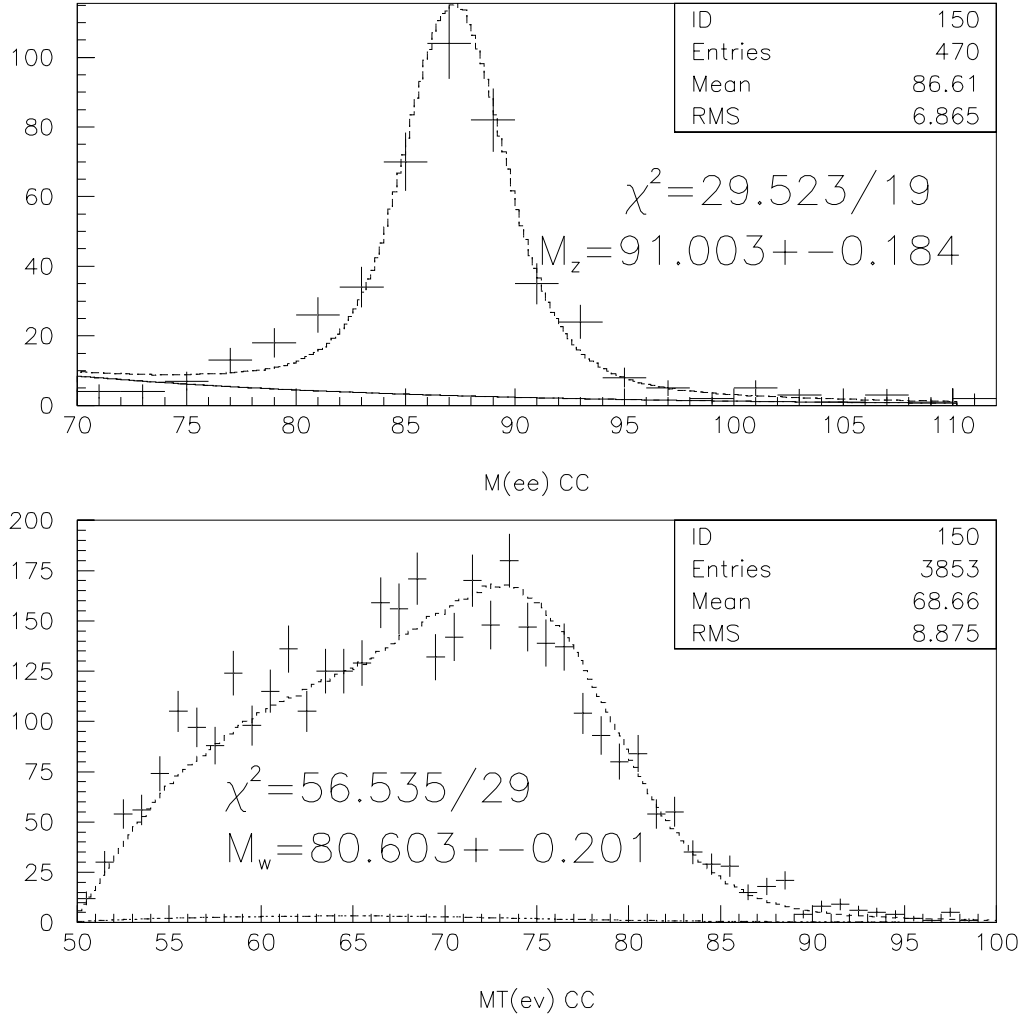
Figure 7.3: Z/W mass fits to the edge electron events. I fit Z invariant dielectron mass and W transverse mass distributions with the MC mass templates generated with the single Gaussian EM resolution function.

term (c_{edge}) are not the same as α_{CC} and c_{CC} in the C-C [7] analysis and have to be re-evaluated from the $\widetilde{C}$-C Z data. However, the problem appears to be more severe though than just a difference in α_{edge} and c_{edge} values. Figure 7.3 shows the dielectron mass from the $\widetilde{C}$-C events shown with the best fitted MC(CMS) mass template generated with the non-edge electron EM resolution function. There is an excess of events on the lower Z mass peak shoulder that the fit can not describe. Also, the W fit quality is poor with $\chi^2 = 56.5$ for 29 degress of freedom (Fig. 7.3).

In fact there is no EM scale and resolution that would give a satisfactory fit to the observed data. This leads us to believe that the EM response has to be described in a different way than used in the C-C [7, 8] analysis, and that a simple Gaussian response is not adequate. In fact the response more nearly resembles the sum of two Gaussians with two different central and RMS values, as noted in Section 4.1 and Fig. 7.4. To see the excess events on the lower Z mass shoulder I subtracted the contribution from the Gaussian with C-C scale and resolution convoluted with BW from the $\widetilde{C}$-C distribution. I used C-C events to get the shape of the Z mass distribution. In Fig. 7.4a, I plot the observed Z mass distribution from C-C and $\widetilde{C}$-C events. The distributions are normalized so that the maximum number of
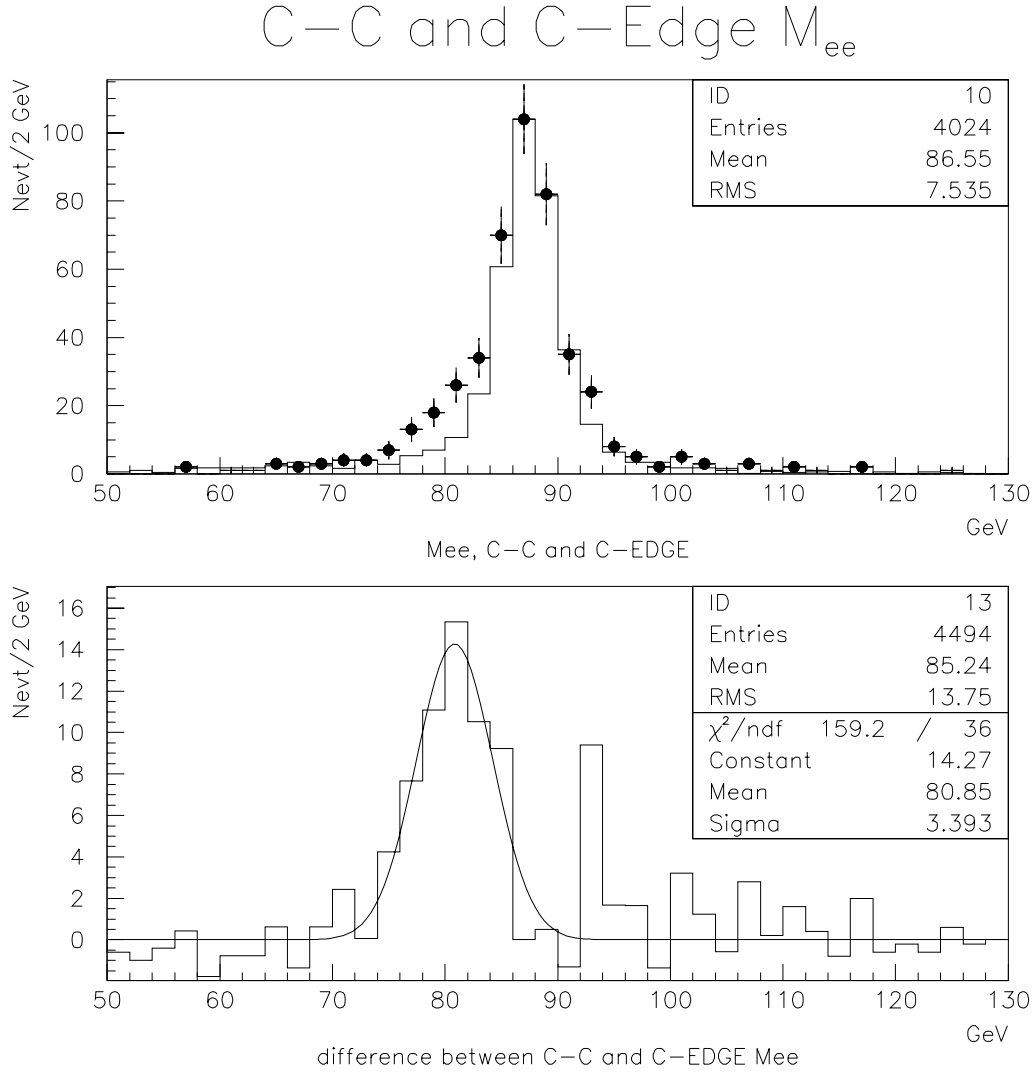
Figure 7.4: Dielectron invariant mass. Z mass from non-edge CC events (solid line) and from Edge-CC events (points). The Edge-CC distribution is scaled so that number of events in the peak bin is the same as in the CC-CC distribution. The figure at the bottom is the difference of the Edge-CC and CC-CC histograms on a bin-to-bin basis, fitted with a Gaussian.

99

events (the peaks of both figures) have the same values. In Fig. 7.4b, I have subtracted the C-C distribution from the $\widetilde{\text{C}}$-C distribution. One sees that what is left is well represented by a Gaussian function. We conclude that the $\widetilde{\text{C}}$-C Z mass can be described as a sum of two Gaussians where the width and the mean of one Gaussian coincides with the C-C Gaussian. Figure 7.5 shows the double Gaussian fit to the $\widetilde{\text{C}}$-C Z mass. The fitted function is a sum of two Gaussians convoluted with a Breit-Wigner. The mean and RMS of the narrow Gaussian are fixed to the appropriate values taken from the C-C analysis [7], and the mean and the RMS of the second, broad, Gaussian are the fit parameters, as was the relative normalization between two Gaussians. The background shape used was obtained in the previous section and the background normalization was a fit parameter. The fit describes the data very well with χ^2 of 12 for 23 degrees of freedom.

7.2.2 Parametrization of EM response

In trying to understand the nature of the double Gaussian EM response, I have studied the dependence of the parametrization on the H-matrix χ^2, isolation, EM fraction and track match significance variables defined above. As a measure of the number of extra events on the lower Z mass shoulder
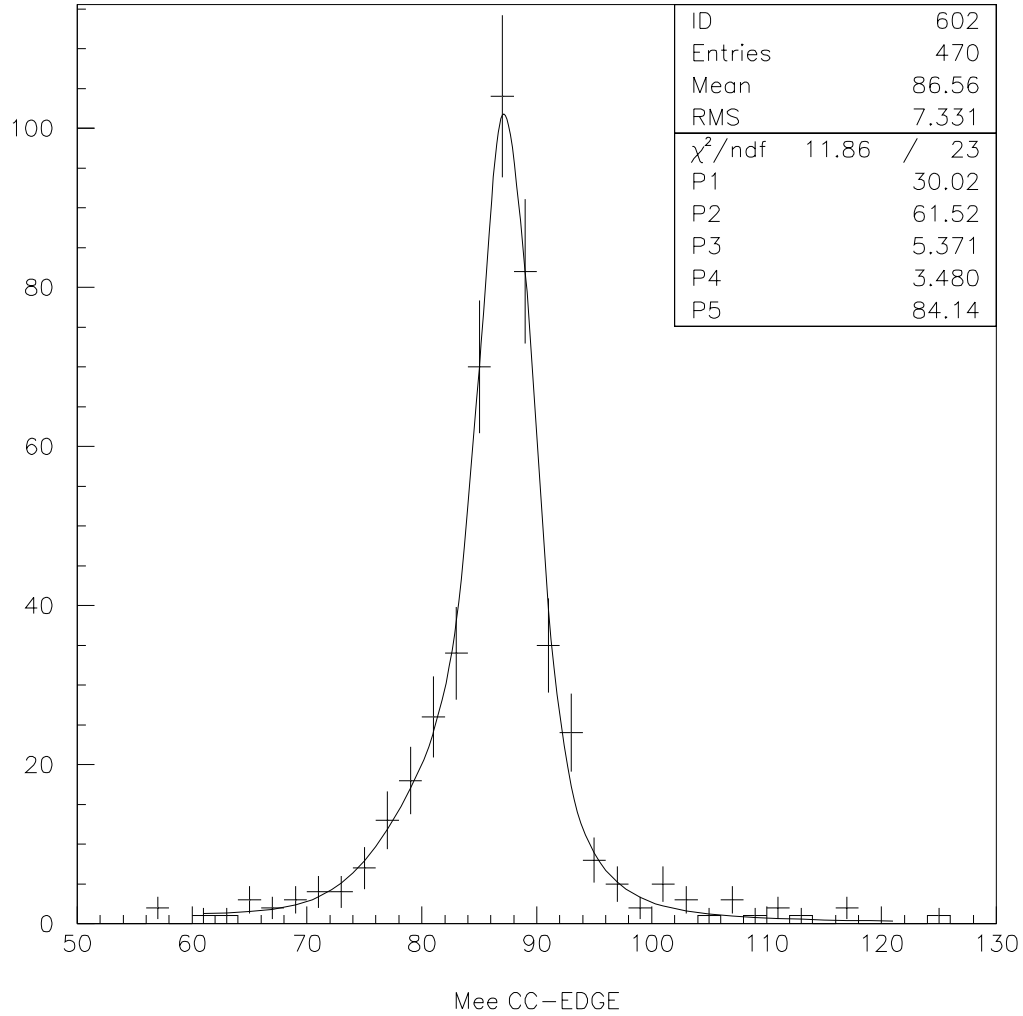
Figure 7.5: The fit to the $\widetilde{C}$-C Z mass distribution with the Breit Wigner convoluted with the sum of two Gaussian functions. The mean and the RMS of one of the Gaussian has been fixed to the C-C values.

I used the fraction of events in a second Gaussian to the total number of events.

For the EM fraction study, I used the $\widetilde{\mathrm{C}}$-C Z sample and required the edge electron to have the EM fraction in the appropriate EM fraction bin, but applied no such constraint on the other electron. I plot the dielectron mass distribution for each bin, and fit them with a Breit-Wigner convoluted with two Gaussians. I then plot the fitted fraction of events in the second Gaussian (f_{edge}) in bins of the EM fraction. I repeat the analysis to get similar plots in bins of H-matrix χ^2, isolation (ISO) and track match significance (σ_{track}). In Figs. 7.6–7.9 I show the fitted mass distributions and in Fig. 7.10 the observed dependences of f_{edge} on each variable.

The statistical uncertainty on the number of events in the broad Gaussian is rather large, but we still can make an observation that two variables may influence the edge EM response. One is the EM fraction and the other is the isolation. The fraction f_{edge} tends to drop with increasing EM fraction. I fit the dependence with a line to see if the slope is statistically different from zero. The slope $\frac{\partial f_{edge}}{\partial \mathrm{EMF}}$ is 17 ± 2.6.

The number of events in the broad Gaussian tends to increase with the worsening of the electron isolation (Fig.7.10 top right plot) but the fit returns

Figure 7.6: I fit the whole $\widetilde{C}$-C Z sample with a Breit-Wigner convoluted with two Gaussians and determine values of the 5 parameters : overall normalization, background normalization, the mean and the RMS of the narrow Gaussian and the mean and the RMS of the broad Gaussian. I fix these parameters and introduce four auxiliary fit paramaters : scale factor of the overall normalization (P1), scale factor of the fraction of events in the broad Gaussian (P4), scale factor for the mean of the both Gaussians (P2) and the background normalization (P3). The fit with these new parametrization of the whole $\widetilde{C}$-C Z's returns P1=P2=P4=1.0 by the design. The plots show the fits with this parametrization of the $\widetilde{C}$-C Z's in bins of the isolation.

Figure 7.7: I fit the whole $\tilde{\mathrm{C}}$-C Z sample with a Breit-Wigner convoluted with two Gaussians and determine values of the 5 parameters : overall normalization, background normalization, the mean and the RMS of the narrow Gaussian and the mean and the RMS of the broad Gaussian. I fix these parameters and introduce four auxiliary fit paramaters : scale factor of the overall normalization (P1), scale factor of the fraction of events in the broad Gaussian (P4), scale factor for the mean of the both Gaussians (P2) and the background normalization (P3). The fit with these new parametrization of the whole $\tilde{\mathrm{C}}$-C Z's returns P1=P2=P4=1.0 by the design. The plots show the fits with this parametrization of the $\tilde{\mathrm{C}}$-C Z's in bins of the χ^2.

Figure 7.8: I fit the whole $\widetilde{C}$-C Z sample with a Breit-Wigner convoluted with two Gaussians and determine values of the 5 parameters : overall normalization, background normalization, the mean and the RMS of the narrow Gaussian and the mean and the RMS of the broad Gaussian. I fix these parameters and introduce four auxiliary fit paramaters : scale factor of the overall normalization (P1), scale factor of the fraction of events in the broad Gaussian (P4), scale factor for the mean of the both Gaussians (P2) and the background normalization (P3). The fit with these new parametrization of the whole $\widetilde{C}$-C Z's returns P1=P2=P4=1.0 by the design. The plots show the fits with this parametrization of the $\widetilde{C}$-C Z's in bins of the EM fraction.
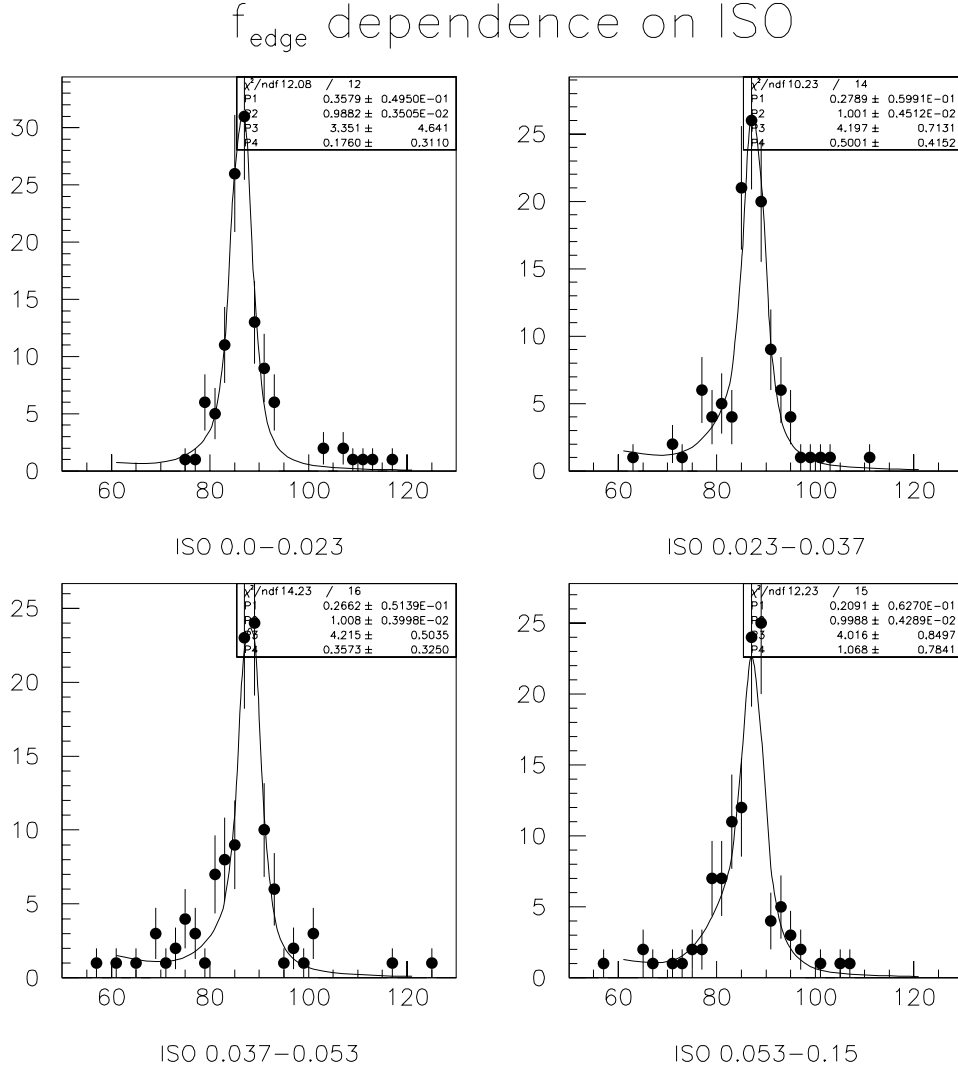
f_{edge} dependence on σ_{trk}

Figure 7.9: I fit the whole $\widetilde{C}$-C Z sample with a Breit-Wigner convoluted with two Gaussians and determine values of the 5 parameters : overall normalization, background normalization, the mean and the RMS of the narrow Gaussian and the mean and the RMS of the broad Gaussian. I fix these parameters and introduce four auxiliary fit paramaters : scale factor of the overall normalization (P1), scale factor of the fraction of events in the broad Gaussian (P4), scale factor for the mean of the both Gaussians (P2) and the background normalization (P3). The fit with these new parametrization of the whole $\widetilde{C}$-C Z's returns P1=P2=P4=1.0 by the design. The plots show the fits with this parametrization of the $\widetilde{C}$-C Z's in bins of the σ_{track}.

106

the slope of 8.4 ± 8.4, and is thus not statistically significant.

The H-matrix χ^2 has little effect on the edge EM response (Fig. 7.10 bottom right plot). The fitted slope is 0.0029 ± 0.01 and is perfectly consistent with zero. The variation of f_{edge} in bins of σ_{track} is also not significant (Fig. 7.10 bottom left plot) with the slope of 0.1 ± 0.2. We do not expect σ_{track} to have any influence on the EM resolution unless the existance of the second Gaussian is in part due to the tracking system. The figures indicate that the EM calorimeter response, and not the tracking measurement, is the source of the asymmetrical Z mass distribution.

The summary of the above observations is: "edge" electrons have a lower EM fraction, and thus a lower energy deposited in the CCEM than "normal" electrons.

There are two ways the EM energy can be lost. The first is when the electron deposits more energy in the first fine hadronic calorimeter layer rather than in the four EM layers. An electron might miss some of the EM layers' material because it goes through the gap between EM modules. The second possibility is that energy deposited in the EM layers is not fully measured because not all of the charge produced in the calorimeter reaches the signal boards. Below I discuss both of these possibilities and the implications.
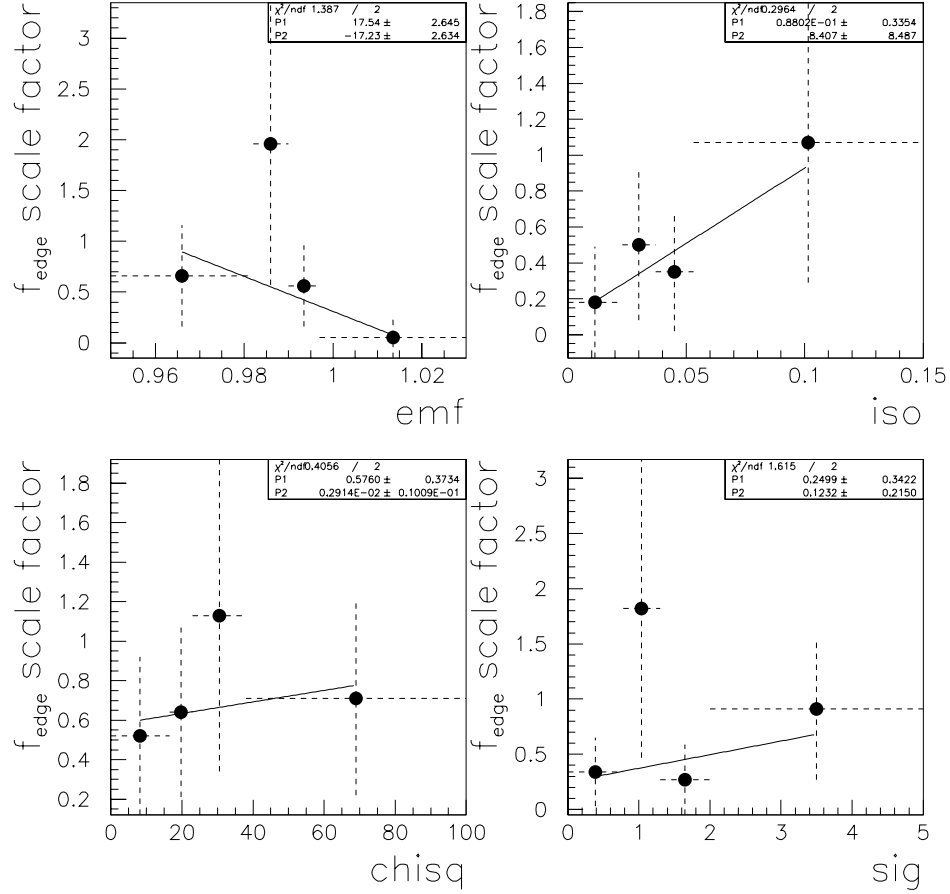
Figure 7.10: The variation of the fraction of events in the broad Gaussian (f_{edge}) as a function of EM fraction, isolation, χ^2 and σ_{track}. The y axis shows how much f_{edge} is different from the value for the overall $\widetilde{C}$-C Z sample. A factor of 1 corresponds to the same fraction as in all $\widetilde{C}$-C Z events. I also show the linear fit, with parameter P2 being the slope of the line. P2 is statistically different from zero only in the EM fraction plot.
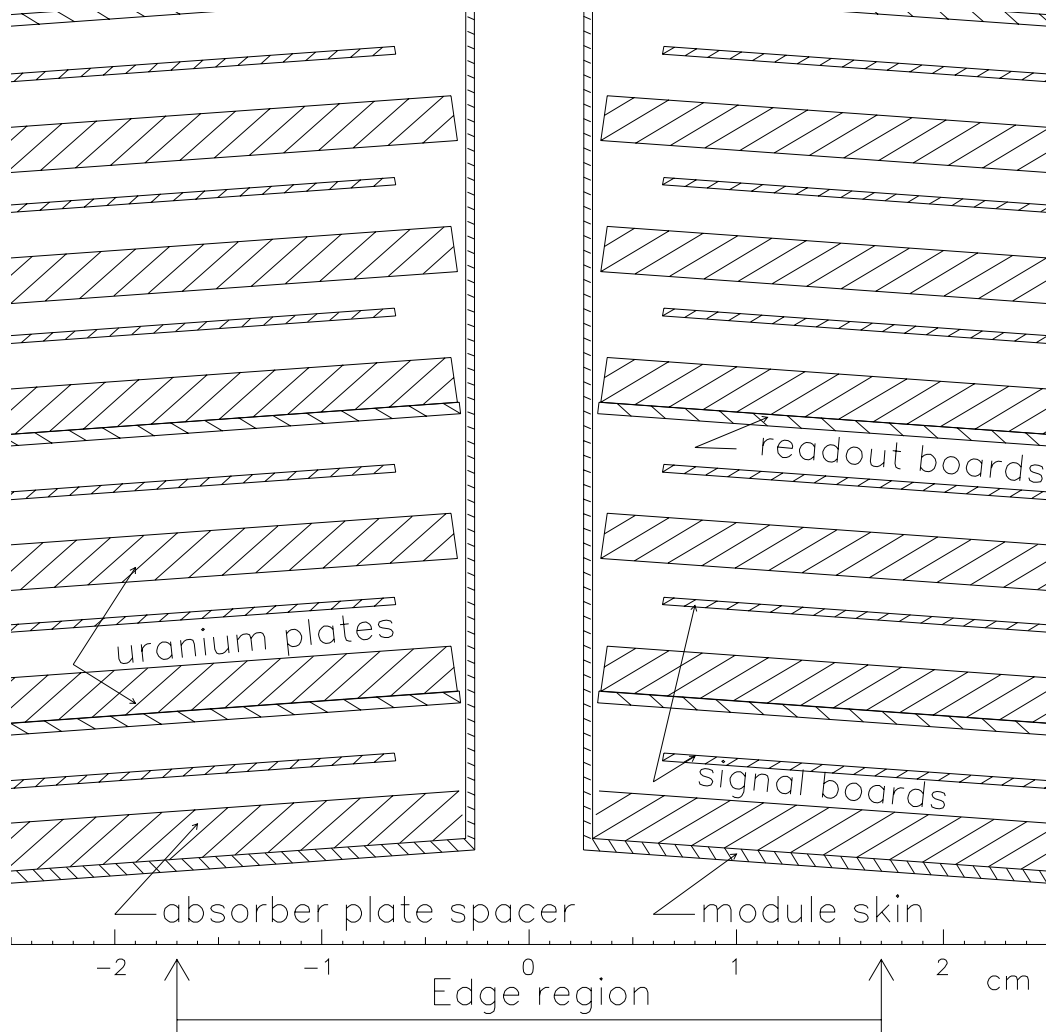
Figure 7.11: A view of the two neighbor CCEM modules. The signal boards extend upto the skin but the resistive coat is set back by 1/8 of an inch. On the drawing, I show not the actual width of the boards but only the part covered with the conductive epoxy. The modules are supported by two end plates mounted at each end of them. The end plates are 1/8 inch wider then the module and that's why there is a gap between the modules. The end plates are not shown on the drawing.

The central calorimeter consists of 32 modules, each approximately 18 cm wide at its inner radius. The module is enveloped by a stainless steel support "skin", which is about one millimeter thick (Fig. 7.11). The signal boards extend almost to the skin, but the resistive coat is offset by 1/8 of an inch and the electric field is distorted near the board's edges resulting in poor charge collection and charge loss. The edge region (10% of the full module at either side) is about 1.8 cm wide. The Moliere radius (R_m) of the CCEM is 1.9 cm. On average, 90% of the electron's shower energy is contained inside a cylinder with radius R_m ([18], [24]) and 70% within a cylinder of half the Moliere radius.

The electron that hits the 10% edge region will produce an EM shower, part of which is in the area of poor charge collection, and that results in some of the produced charge being lost. The measured energy in such a case would be lower than the "true" energy of the electron. However, the size of the edge region is about one Moliere radius and on average the shower's core is narrow and the amount of the deposited energy drops fast in the lateral direction. As noted, on average 70% of a shower is contained within 1/2 of the R_m which is perfectly inside the good field region. So there is a significant probability the electron's shower is contained within that region. This results in an EM

response no different from non-edge electrons. For such an electron the EM scale and the EM resolution are the same as for a non-edge electron.

If energy is lost in the first scenario, the edge electron has a lower EM fraction because it showers later due to the lack of material at the module edge, and the electron loses less energy in the CCEM. As a result the electron loses more energy in the first layer of the fine hadronic calorimeter. However, that would not lead to a lower electron's energy being measured. The EM resolution for such electrons would be worse, but we should not see an excess of events on the lower Z mass shoulder due to this effect only.

In the second scenario, the electron's energy deposited in the calorimeter is partly lost in the regions with distorted electric field. If energy is lost, then the more it is lost the smaller the measured EM fraction becomes. The EM fraction decreases because the amount of energy in the EM calorimeter decreases, while energy in the fine hadronic calorimeter is not affected. The azimuthal center of the fine hadronic calorimeter's modules are aligned with the gap between the EM modules, so "edge" electrons hit the middle of FH1 layer. The higher the EM fraction the more probable it is that the electron showered "normally" and all of the charge produced by its shower is collected.

The above considerations suggests that the sample of edge electrons could

111

have contributions from three groups of electrons. The first consists of electrons whose shower's charge was totally collected by the signal boards. Such a group has the EM scale and the EM resolution consistent with the non-edge electron values.

The second group consists of the electrons whose shower was partly lost in the region of distorted electric field. This group has a lower value of the EM scale, worse EM resolution, and lower EM fraction. We observe that the electron's H-matrix χ^2 is not affected though (Fig. 7.7). Such a behavior is consistent with the assumption that the electron from the second group passes through the same amount of material and has the same shower shape as non-edge electrons. The difference is that part of the charge produced by the shower particles is not collected at all, or not collected in time, by signal pads because of the distorted electric field lines at the edges of the EM modules.

The second group of edge electrons consists of electrons which lose different amounts of energy. Some of them happened to be closer to the edge or have broader shower and lost a significant amount of their energy (due to the distorted electric field) and some lost very little. To describe the EM response for this group one should sum over a continuous set of Gaussians

112

with different means and widths. However, empirically we see that this sum can be approximated with a single gaussian. The data (Fig.7.4) tells us that their average EM response function could be described with one additional Gaussian. Below I will discuss an extension to this parametrization which tries to vary the Gaussian's width depending on the amount of lost energy.

And, finally, the third group consists of electrons which mostly showered in the hadron calorimeter. However, as noted, this group would have the same EM scale as non-edge CC electrons but worse resolution, and we do not observed this in the data (and also it would be heavily suppressed by the selection cuts on the EM fraction and $\chi^2 < 200$).

The conclusion is that observed edge electrons have contributions from only the first and the second group of electrons, and a parametrization that could be used to describe the edge EM response has to describe both these groups. The double Gaussian is an attractive parametrization because it introduces only three more parameters (α_{edge}, c_{edge} and f_{edge}) and because data seems to suggest it. Figure 7.4 implies that the first Gaussian should have the same parameters as non-edge electrons (and describe the first group of the electrons) and the second Gaussian has to describe the second group

of edge electrons. The parametrization adopted is given by

$$
E_e^{meas} = \begin{cases} \alpha_{edge}\, E_e^{true} + \delta_{edge}, & \text{in } f_{edge} \text{ fraction of cases} \\[2mm] \alpha_{CC}\, E_e^{true} + \delta_{CC}, & \text{in } (1 - f_{edge}) \text{ fraction of cases} \end{cases} \tag{7.3}
$$

$$
\sigma_E/E = \begin{cases} s_{edge}/\sqrt{E} \oplus c_{edge} \oplus N_{CC}/E, & \text{in } f_{edge} \text{ fraction of cases} \\[2mm] s_{CC}/\sqrt{E} \oplus c_{CC} \oplus N_{CC}/E, & \text{in } (1 - f_{edge}) \text{ fraction of cases} \end{cases} \tag{7.4}
$$

In the general case, δ_{edge} does not have to be the same as δ_{cc}. But as I show later in the thesis (Section 8.1), the value of δ_{edge} is consistent with δ_{cc} and thus I take $\delta_{edge} = \delta_{cc}$. I keep the sampling term the same too ($s_{edge} = s_{CC}$), and discuss the reason in Section 7.2.4. The N term arises from uranium radioactivity and electronics noise, and should be independent of location in the module.

To check that the first Gaussian does indeed have the same parameters as the non-edge electron's Gaussian I fitted the Z boson dielectron mass distribution with a double Gaussian convoluted with a Breit Wigner, in which both Gaussians' mean and width were the fit parameters (Fig. 7.12). The fitted value of the RMS and mean of the first (narrow) Gaussian are consistent with those for non-edge electrons (see parameter values and their errors in

Fig. 7.12).

I have also made an attempt to invent other parametrizations. The parametrization should be such that the single Gaussian non-edge parametrization (Eqs. [7.1] and [7.2]) are obtained as limiting cases. For instance, the double Gaussian parametrization (with the response parameters in equations [7.3],[7.4]) transforms into the single Gaussian as the fraction of events in the second Gaussian reaches zero. The parametrization has to be asymmetric in energy because the excess of events over a single Gaussian appears to be on the low mass side of the Z mass distribution. And the parametrization has to have as few parameters as possible. Moreover, since we already have a suitable double Gaussian parametrization with three new parameters, any other parametrization should have no more than three parameters. And lastly, the parameterization has to have some physical justification. I tried to modify a Gaussian function to satisfy the above criteria. The parametrization of a Gaussian plus a small function would always bring us back to the double Gaussian because that what we see in the data. I tried the following parametrization to describe the second group of electrons, not as a separate term in the EM response, but rather as a modification of the function itself. The more an electron loses its energy in the gap between modules, the worse
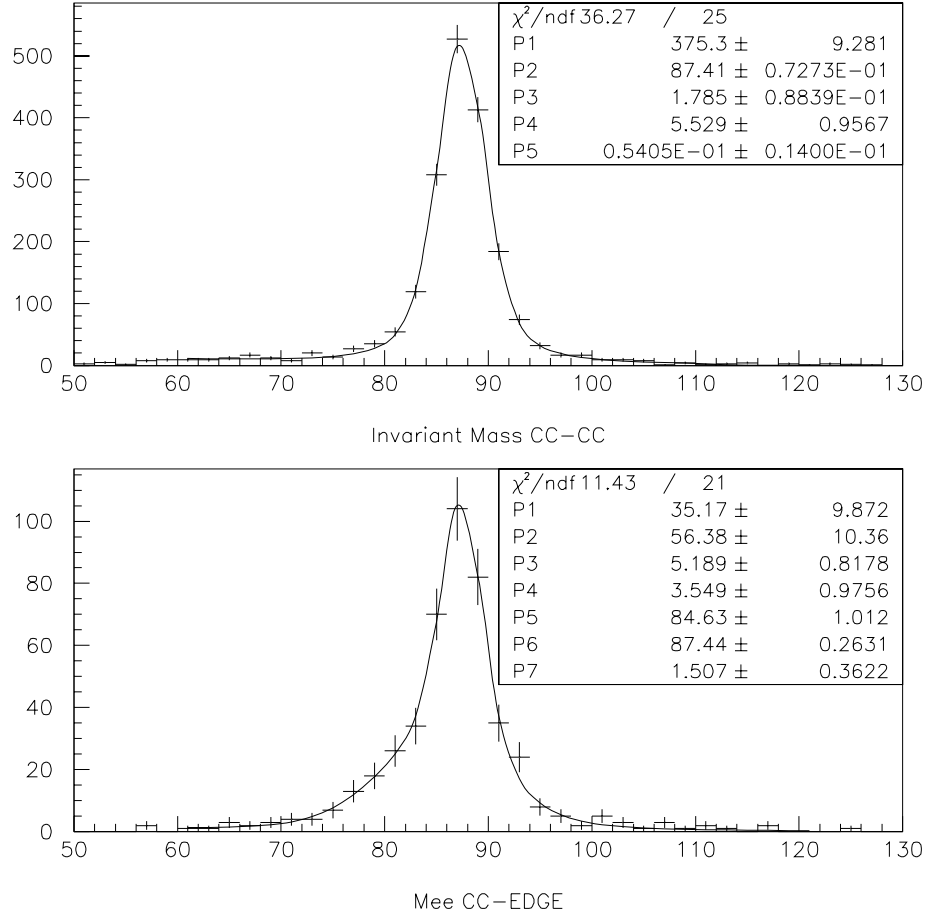
Figure 7.12: Top figure shows Z C-C events fitted with a single Gaussian convoluted with a Breit Wigner function. Parameter P2=87.41 is the mean of the Gaussian and P3=1.79 is the RMS. Figure on the bottom shows Z $\tilde{\text{C}}$-C events fitted with a sum of two Gaussians convoluted with a Breit Wigner function. Both Gaussians' mean and RMS were free fit parameters. P6=87.44 and P7=1.51 are the mean and RMS of one (narrow) Gaussian, and P5=84.63 and P3=5.2 are the mean and RMS of the other Gaussian. The parameters of the narrow Gaussian are consistent with the non-edge single Gaussian.

its resolution becomes. Below is a "running" Gaussian that could describe this:

$$G(E) = \text{const} \cdot \exp^{\left[\frac{(E-E_{\text{true}})^2}{2\,\sigma^2(E-E_{\text{true}})}\right]} , \qquad (7.5)$$

with $\sigma(\Delta E)$ running as $\sigma(\Delta E) = \sigma_0 - S \cdot \Delta E$, where $S = \begin{cases} S_0, & \text{if } \Delta E \leq -T \\ \\ 0, & \text{if } \Delta E > -T \end{cases}$.

After a certain threshold T, the RMS starts growing linearly with the deviation from the "true" energy. This parametrization has two parameters, the slope S_0 and cutoff paramerer T. In order to calculate S_0 and T, I have to implement the EM resolution parametrization in the CMS MC, generate Z mass templates and fit the $\widetilde{C}$-C events for the parameters. I tried a simpler approach first and rewrote the energy parametrization as a function of the Z boson mass ($G(M) = \text{const} \cdot e^{\frac{(M-M_{\text{true}})^2}{2\,\sigma^2(M-M_{\text{true}})}}$), convoluted with a Breit-Wigner, and fitted the Z mass. The fit, shown in Fig. 7.13, is quite satisfactory. It enhances the low mass region, leaving the upper side almost unchanged as expected. But when I tried to put Eq. 7.5 into CMS as an energy response function ($G(E)$) I fail to find any set of S_0 and T that would satisfactorily reproduce the $\widetilde{C}$-C Z mass distribution, and I had to discard that parametrization.

117

ID	602
Entries	470
Mean	86.56
RMS	7.331
χ^2/ndf 16.78 / 24	
P1	368.7
P2	−0.2221
P3	2.387
P4	3.458

Mee CC−EDGE
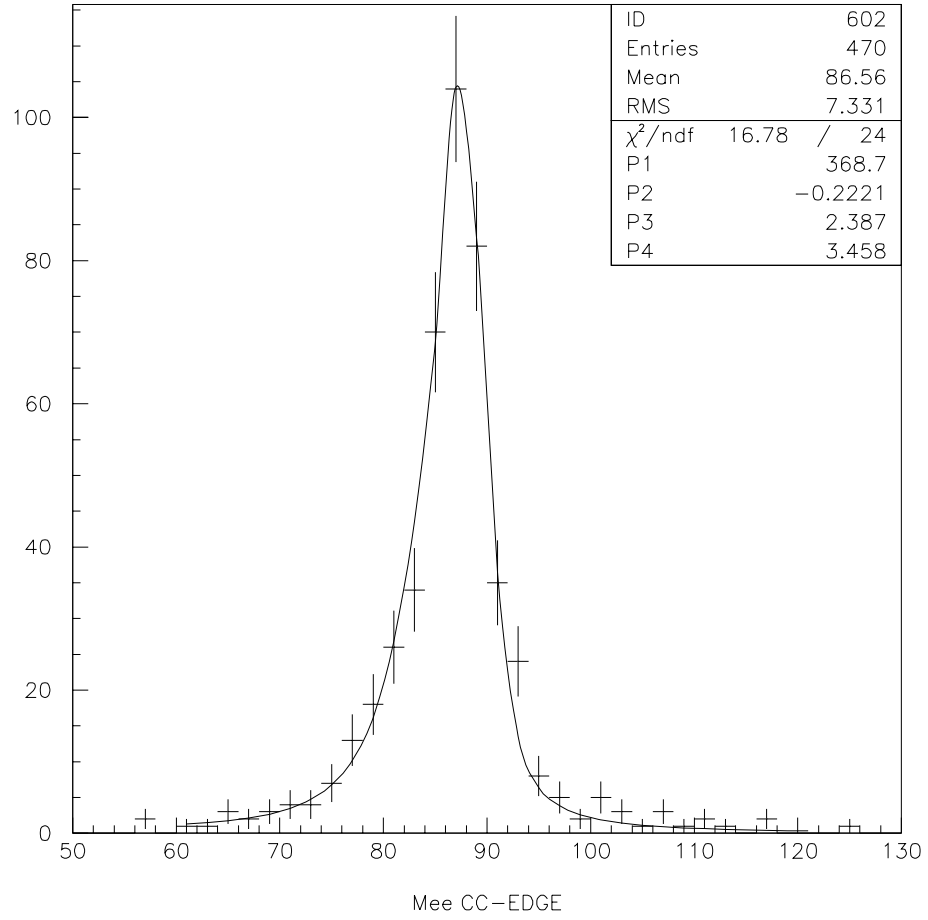
Figure 7.13: Z $\widetilde{\text{C}}$-C sample. Z mass distribution and a fit with the "running" Gaussian parametrization (Eq. 7.5), convoluted with a Breit Wigner function.

118

Another modification would be to vary the Gaussian amplitude with energy, like $G(E) = F(E - E_{true}) \cdot e^{\frac{(E - E_{true})^2}{2\,\sigma^2(E - E_{true})}}$. But the function $F(\Delta E)$ would require at least one, or most probably, more parameters and thus would have no benefit over a double Gaussian, and I did not pursue that path.

The double Gaussian parametrization (Eqs. [7.3],[7.4]) is the only one found that has relatively few parameters and describes the observed data. It needs three parameters α_{edge}, c_{edge} and f_{edge} and it is the parametrization that I chose to use in the analysis.

We have studied the response of the CCEM near the edge of the modules using a full GEANT simulation. The simulation is not exact, in that the details of the signal board resistive coat, and the module skins and inter-module gaps are not present in the MC. Qualitatively however, the response for electrons in the edge region in the MC is similar to what is seen in the data; there is a shoulder at slightly lower mass in addition to the peak at the mass observed for non-edge electrons, and the fraction of events in the lower mass gaussian is similar to that seen in the data (Fig. 7.14).
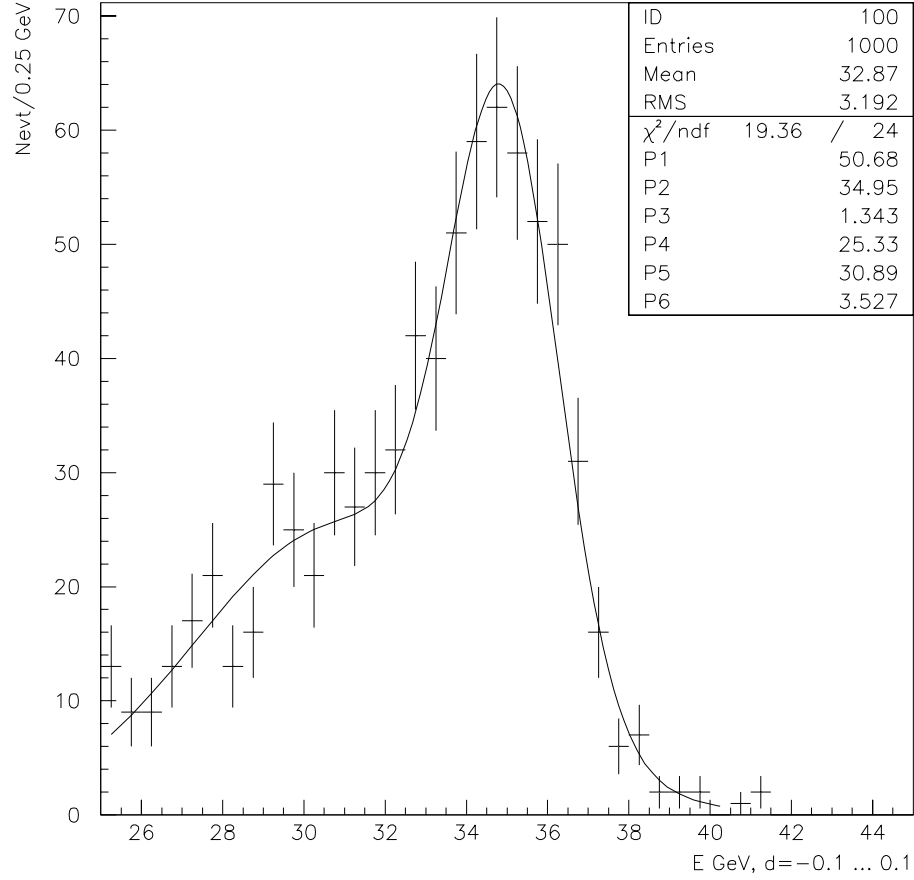
Figure 7.14: Monte Carlo simulation of the edge EM response. The sample of 40 GeV electrons distributed uniformly across the edge region was generated using GEANT MC. The edge region was not exactly simulated (details of the signal board resistive coat are absent). The EM response could be fit with a sum of two gaussians. The collected energy is lower than 40 GeV but this simulations yields low EM response for non-edge electrons as well.

120

7.2.3 Determination of edge electron EM scale and resolution parameters

I have modified the CMS Monte Carlo to include the above parametrization (Eqs.[7.3,7.4]) of the EM response of the edge electrons. Parameters α_{edge}, c_{edge} and f_{edge} have been added, along with α_{narrow} and c_{narrow} to describe the parameters of the first Gaussian. In the fits, α_{narrow}, c_{narrow} have been fixed to the values α_{cc}, c_{cc} for non-edge electrons. The electron's energy gets smeared according to the second $(\alpha, c)_{edge}$ Gaussian with probability f_{edge}, and by the first $(\alpha, c)_{cc}$ Gaussian with probability (1-f_{edge}).

I fit the Z mass distribution with the Z Breit-Wigner line shape convoluted with the response function based on the two gaussian parametrization. The mean α_{edge}, c_{edge} and fraction of events in the second Gaussian are the fit parameters. I obtain a value of 0.31 for f_{edge}, to be used as a seed value for the fits below for α_{edge} and c_{edge}.

Using the CMS Monte Carlo I generate a 2 dimensional grid in bins of α_{edge} and c_{edge}. For each point in the grid, a dielectron mass distribution is generated for the given α_{edge} and c_{edge}, with the generated Z mass equal to the LEP value. Each distribution is a histogram in bins of dielectron

mass. For each α_{edge}, c_{edge} bin I calculate the likelihood function between the high statistics MC histogram and the data histogram. I normalize the MC dielectron mass histogram to the number of events in data. For the likelihood calculation I assume that the number of data events in each mass bin is distributed according to a Poisson distribution with mean equal to the number of MC events in each mass bin. The likelihood is given by:

$$ L = \prod_{i=1}^{N} \frac{\mu_i^{r_i} \, e^{-\mu_i}}{r_i!} \quad , $$

where N is the number of bins in the mass histogram, μ_i is the number of MC events in the ith bin, and r_i is the number of data events in the same bin.

For each α_{edge}, c_{edge} bin I have a $-\log(L)$ value. I find the α_{edge}, c_{edge} that corresponds to the minimum value of $-\log(L)$. Fortunately, α_{edge} and c_{edge} are nearly uncorrelated (Fig. 7.15) and I can fit for each of them separately (having found an approximate minimum in the 2 dimensional space). I generate a 1D grid in bins of α_{edge} or c_{edge} and fit the $-\log(L)$ with parabola to find α_{edge} or c_{edge}, and their errors.

In the above 2D fits, I use a seed value of f_{edge}=0.31, generate a 1D
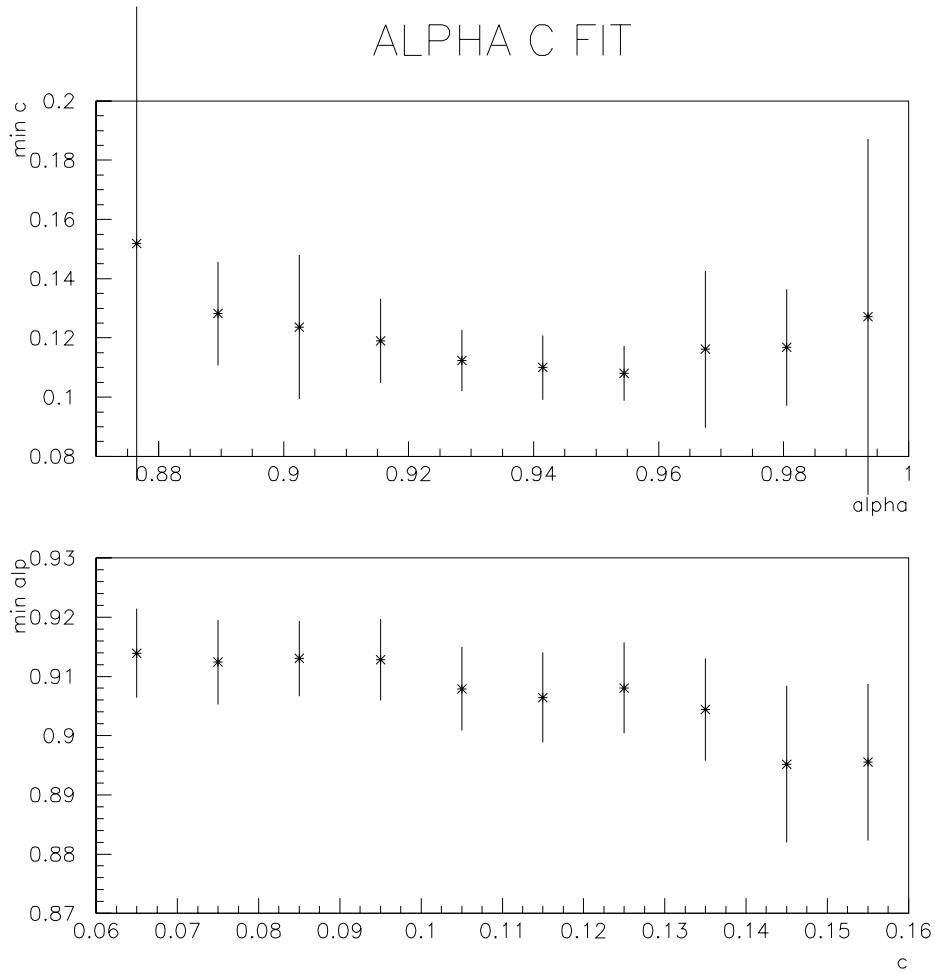
Figure 7.15: Z $\widetilde{C}$-C events. Maximum likelihood fit of the Z invariant dielectron mass distibution with CMS grids in 2 dimensional $(\alpha_{edge}, c_{edge})$ space. The top plot shows c_{edge} corresponding to the maximum likelihood as a function of α_{edge}. The bottom plot shows α_{edge} corresponding to the maximum likelihood as a function of c_{edge}. Points correspond to a change in the parameter when -log(likelihood) increases by one half. If the parameters were completely uncorrelated both plots would be flat.

grid, and fit for α_{edge} and c_{edge}. To account for a correlation between f_{edge}, α_{edge} and c_{edge}, I use the determined α_{edge}, c_{edge} values, generate a 1D grid in bins of f_{edge}, and fit for the fraction using the above procedure. I then use the newly determined f_{edge}, and refit for α_{edge} and c_{edge}. I iterate until the fit converges, and the fitted f_{edge}, α_{edge} and c_{edge} stabilize. The fit converged after one iteration to:

$$\alpha_{edge} = 0.912 \pm 0.018$$
$$c_{edge} = 0.101^{+0.028}_{-0.018} \qquad (7.6)$$
$$f_{edge} = 0.346 \pm 0.076$$

Figures 7.16 and 7.17 show the fits. Using the $(\alpha, c, f)_{edge}$ values from Eq. 7.6, I then generate the dielectron mass templates in bins of Z mass and using maximum likelihood methods fit for the Z mass (Fig. 9.1). It comes out to be:

$$M_Z = 91.199 \pm 0.203 \text{ GeV}, \ \chi^2 = 10/19$$

The fit didn't exactly give the input LEP value of 91.1869 GeV (though it is statistically consistent with the LEP value) for M_Z, but it did not have to. The number of parameters in the edge EM resolution model (Eq. 7.4) is actually more than 3. It is five – three edge parameters $(f, \alpha, c)_{edge}$ plus
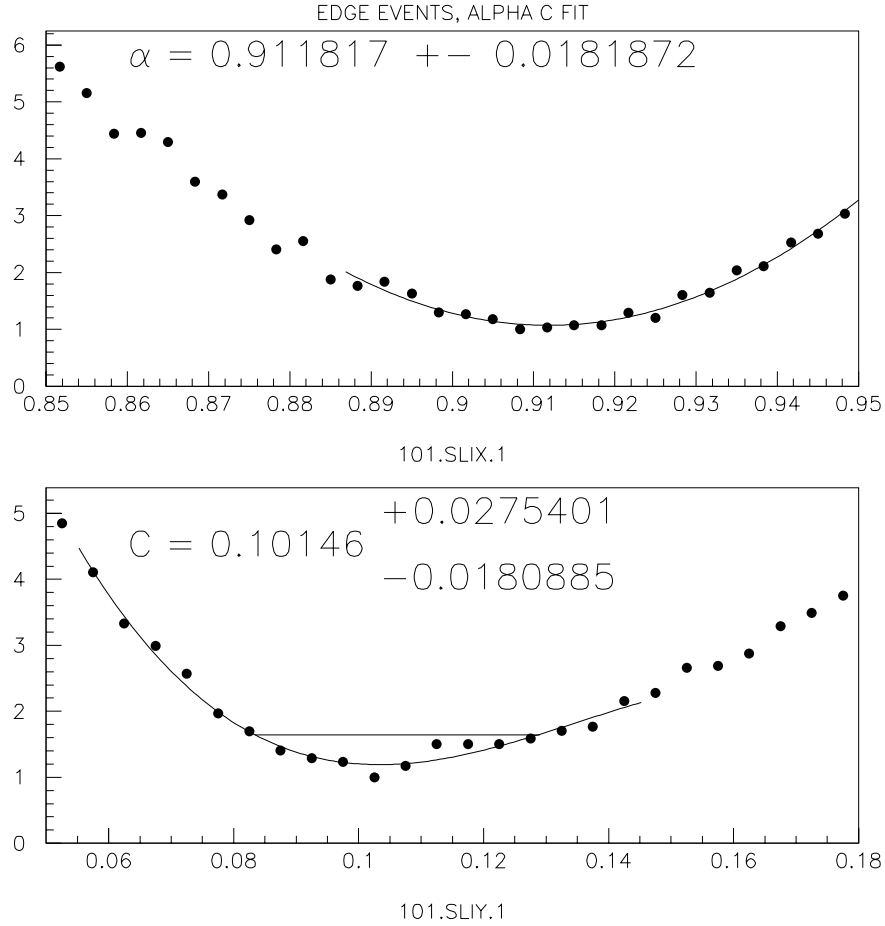
Figure 7.16: $Z\ \widetilde{C}$-C events. Z invariant dielectron mass distibution maximum likelihood fit with CMS grids for α_{edge} and c_{edge}. The top plot shows -log(likelihood) as a function of α_{edge} fitted with a parabola. The bottom plot shows -log(likelihood) as a function of c_{edge}, fitted with the third degree polynomial. The line shows the minimum $\pm$ 0.5 log(likelihood) range.
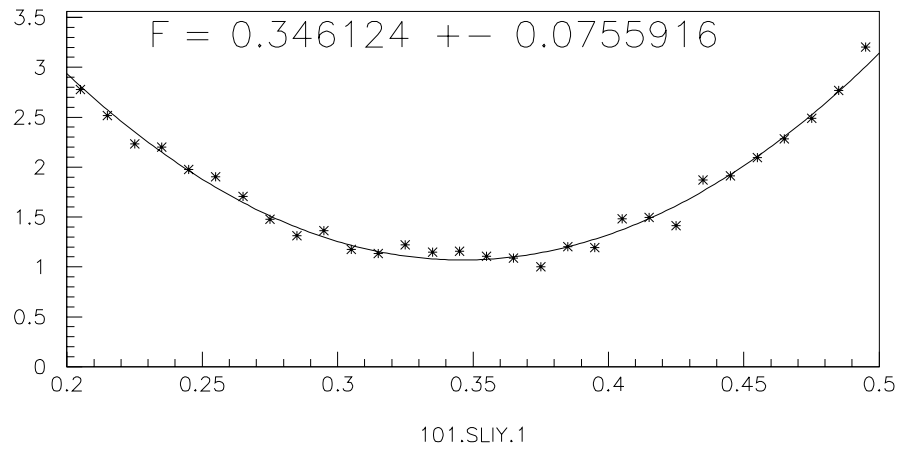
Figure 7.17: Z $\widetilde{\text{C}}$-C events. Z invariant dielectron mass distibution maximum likelihood fit with CMS grids for f_{edge}. The plot shows -log(likelihood) as a function of f_{edge} fitted with parabola.

α_{cc} and α_{narrow}. When I fit for the edge EM response parameters I vary only three edge parameters and find a local minimum in the 5 dimensional likelihood space. The global minimum is slightly shifted because the $\widetilde{C}$-C Z sample's α_{cc} and α_{narrow} are only statistically the same as α_{cc} from the C-C Z sample. So the global minimum is only statistically equal to the local minimum.

7.2.4   EM resolution constant term

The EM resolution of the edge electrons is worse than that of non-edge electrons and we chose to adjust c_{edge} to describe it. But the EM resolution consists of three terms (noise, constant and sampling terms), and increasing the sampling term could describe a broader resolution as well. The difference in changing the sampling term rather than the constant term is that it would lead to a different energy dependence of the resolution. In order to see that c_{edge} and not the sampling term has to be adjusted, we divided the Z sample into two samples – one with the edge electron's transverse energy $E_T(e) < 41$ GeV and the other with $E_T(e) > 41$ GeV. The value 41 GeV, was chosen because it roughly divides the sample in half. The average energy in the first sample is $< E_T(e) >= 36$ GeV, and $< E_T(e) >= 47$ GeV in the

second. I didn't change any of the edge parameters (α_{edge},c_{edge},f_{edge}) because I assume they are energy independent.

I generated Z mass templates using values from Eq. 7.6 and fitted for the Z mass. The fitted Z masses (Fig. 7.18) are:

$$M_Z = 91.101 \pm 0.319 \text{ GeV}, \ \chi^2 = 4.5/14, \quad E_T(e) < 41 \text{ GeV}$$

$$M_Z = 91.064 \pm 0.270 \text{ GeV}, \ \chi^2 = 12/16, \quad E_T(e) > 41 \text{ GeV}$$

They are in very good agreement with each other and the LEP value. So there is no evidence that the sampling term of the edge electron is different from that for the non-edge electron.

7.3 Consistency checks

7.3.1 Other data samples

As a consistency check I selected events that were not used in the determination of the edge electron EM parameters, but that do depend on them. As independent samples I used $\widetilde{\text{C}}$-$\widetilde{\text{C}}$ events (both electrons at the edge) and $\widetilde{\text{C}}$-E events (one electron from the EC calorimeter and the other from
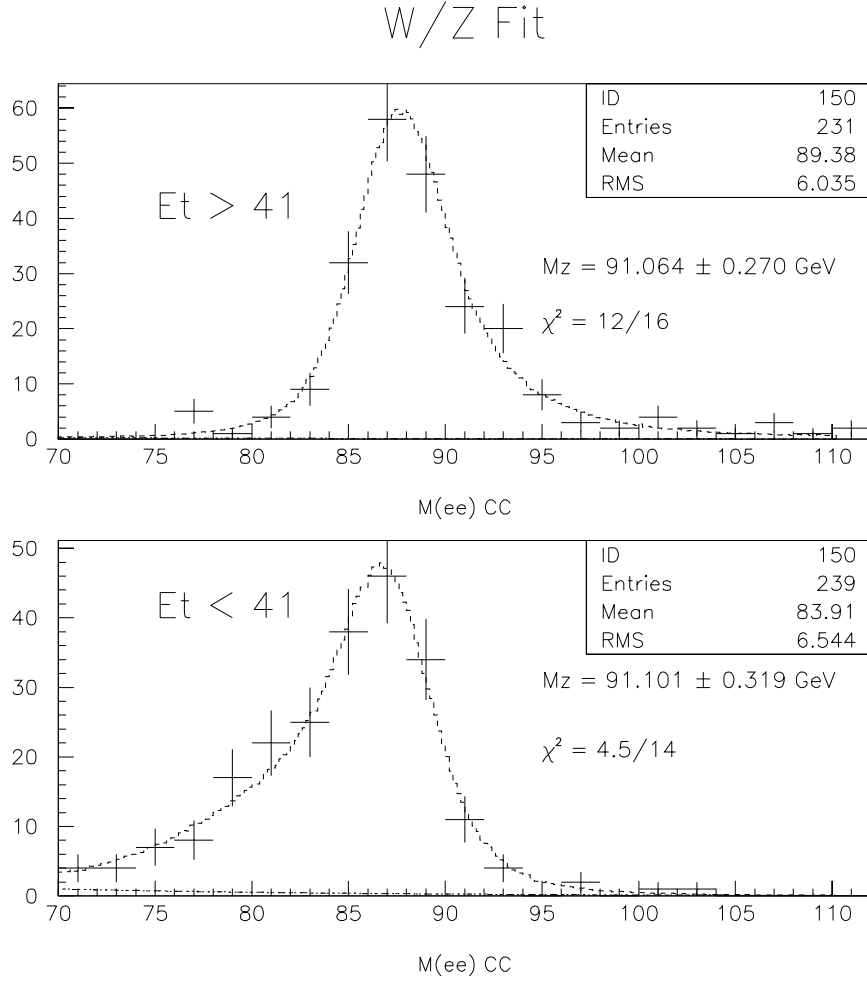
Figure 7.18: Z $\widetilde{\text{C}}$-C events. Z invariant dielectron mass distibution if edge electron's E_T is more than 41 GeV (top figure) or less than 41 GeV (bottom figure) fitted with CMS mass templates.

the edge). I used the parameters from Eq. 7.6, and generated MC Z mass distributions, and compared them to the independent data samples.

First, applying the above data selection criteria I selected events with both electrons at the edge of the CCEM modules. We have 47 such events. I used the edge EM resolution parameters from Eq. 7.6, generated Z mass templates, and fit for the Z mass. Due to small statistics, I rebinned the mass distribution with double the bins size. The resulting fitted Z mass is (Fig. 7.19):

$$M_Z = 90.375 \pm 0.328 \text{ GeV}, \ \chi^2 = 8.5/6 \tag{7.7}$$

in adequate agreement with the LEP value of 91.1869.

Then, I selected $\widetilde{\text{C}}$-E events. One electron was required to be in the EC calorimeter and the other at the edge of the CCEM modules. I selected 154 events. As above, I used the same edge parameters as in Eq. 7.6. The EM parameters of the EC electron were taken from the EC W mass analysis [8], and have not been modified. I fit for the Z mass, and find the fitted value in the good agreement with the LEP value (Fig. 7.20 top):

$$M_Z = 91.097 \pm 0.416 \text{ GeV}, \ \chi^2 = 9.8/13$$

130
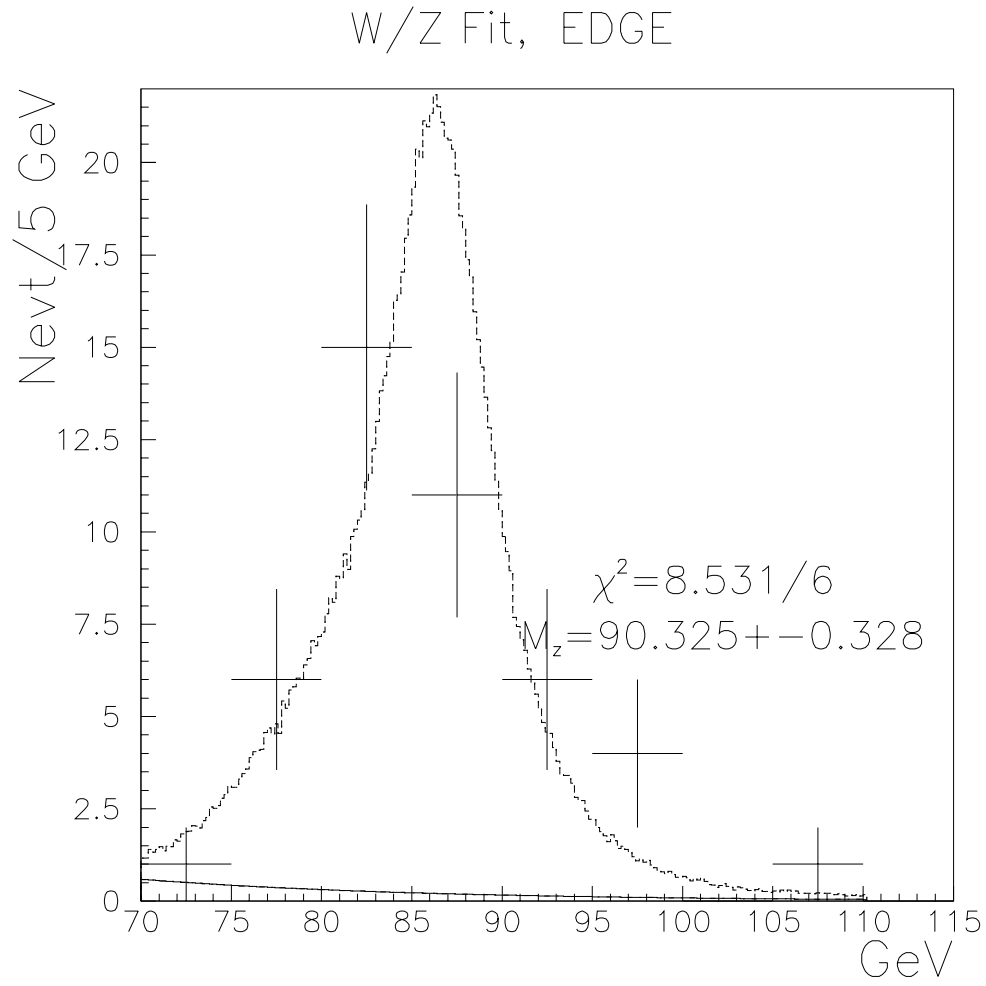
Figure 7.19: $\widetilde{C}$-$\widetilde{C}$ Z dielectron invariant mass distribution and the fit with the CMS templates generated with parameters from Eq. 7.6.

131
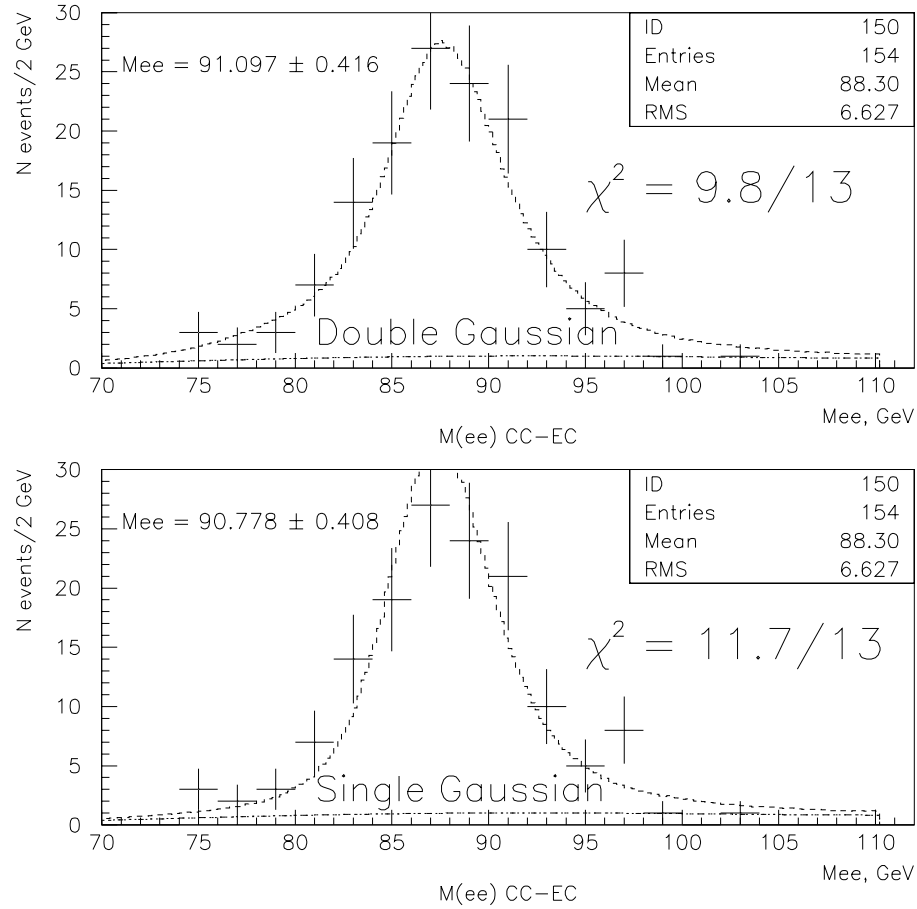
Figure 7.20: $\widetilde{C}$-E Z dielectron invariant mass distribution and the fit with the CMS templates generated with a double Gaussian EM resolution (top figure), or a single Gaussian EM resolution (bottom figure).

To see the effect that the broad Gaussian produces, I also fitted the $\widetilde{\text{C}}$-E Z

events using non-edge CC electron parameters. The fit quality is worse, and

Fig. 7.20(bottom) shows that the MC does not describe the data as well (but

χ^2 is still reasonable):

$$M_Z = 90.778 \pm 0.408 \text{ GeV}, \ \chi^2 = 11.7/13$$

7.3.2 Subsamples in EM fraction

As an important cross check I have divided the $\widetilde{\text{C}}$-C sample into two groups

based on the EM fraction and fit for the Z and W masses for each group. We

have seen above (Section 7.2.2) that f_{edge} depends on EMF, so we want to

be assured that our analysis, which sums over all EMF values, is defensible.

The choice of splitting the sample according to the EM fraction is motivated

by the observed dependence of f_{edge} on the EM fraction (Figs. 7.8, 7.10). The

first group has events with the edge electron's EM fraction less than 0.99 (Fig.

7.21). The second – with edge EM fraction more than 0.99. The EM fraction

sometimes is more than 1 when the signal measured in the first fine hadronic

calorimeter layer is below the average pedestal. No EM fraction requirement

133
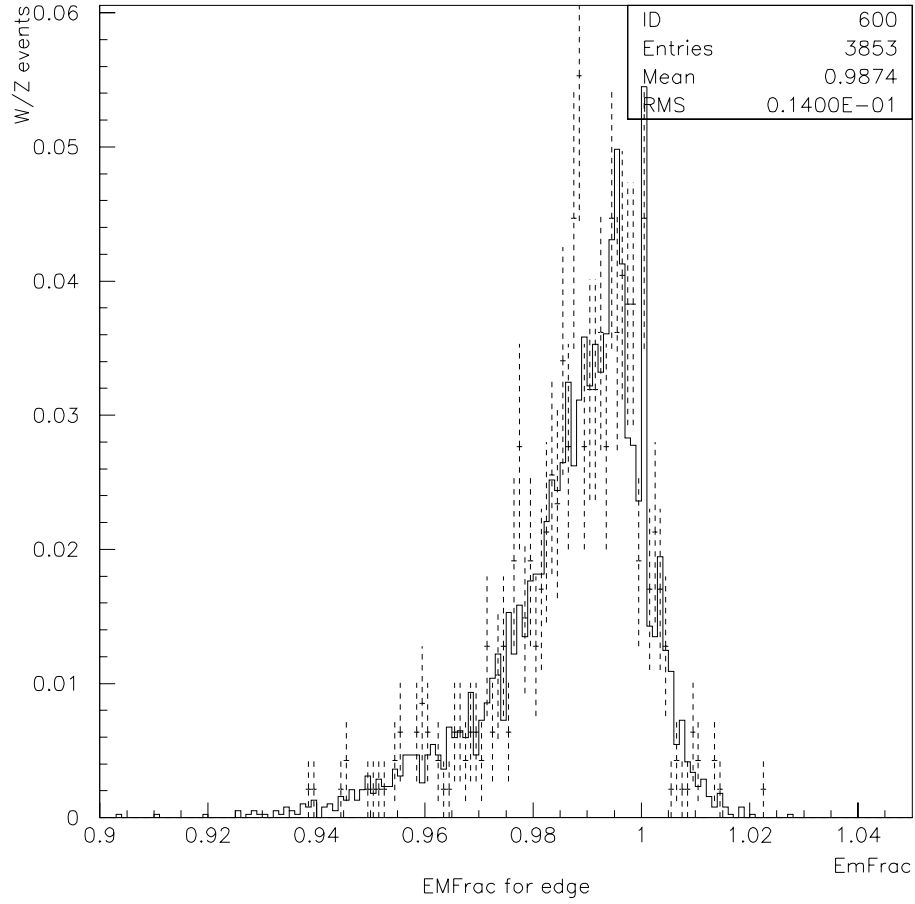
Figure 7.21: Edge W (solid line) and $\widetilde{\mathrm{C}}$-C Z (points) EM fraction distributions.

was applied to the non-edge CC electron. As one would expect, the EM edge parameters are very sensitive to the EM fraction. The higher the edge EM fraction, the closer the parameters of the second Gaussian are to the non-edge parameters. High EM fraction means that most of the electron energy has been collected in the EM part of the calorimeter, and less EM shower energy is lost in the poor charge collection part of the calorimeter. Thus it means that the edge electron difference from non-edge electron diminishes at high EM fraction.

I observe that the non-edge EM parameters change with EM fraction too. The EM fraction of the non-edge electron in the above two groups was not restricted to any EM fraction range. However, since 70% of the edge electrons have an EM scale and resolution the same as non-edge electrons I have to investigate the EM fraction dependence of the non-edge EM parameters too. And so I divided the C-C sample into two EM fraction groups. One C-C electron was required to have an EM fraction less(more) than 0.99, and the other could have any EM fraction. I generated Z mass templates, and fitted low and high EM fraction events separately for the Z mass. The Z masses come out different (Figs. 7.22,7.23) from the LEP value, and I determined the necessary extra correction to the EM scale for the low/high EM fraction

135

non-edge electron.

$$\text{correction to EM scale} = 0.9983 \pm 0.0010, \qquad \text{EM fraction} > 0.99$$

$$\text{correction to EM scale} = 1.0032 \pm 0.0014, \qquad \text{EM fraction} < 0.99$$

Then, I have to find new EM edge parameters $(\alpha_{edge}, c_{edge}, f_{edge})$ for the low and high EM fraction edge electrons. As mentioned above, the assumed model of edge EM response requires that the parameters of the narrow Gaussian be the same as non-edge electron's. That is why I have corrected α_{narrow} by the above correction factors. Then I repeated the procedure from the above section to determine α_{edge}, c_{edge} and f_{edge}. I generated 1D grids in bins of α_{edge}, c_{edge}, or f_{edge}, and iterated until the fit converged. I found the following edge parameters for the low EM fraction:

$$\alpha_{edge} = 0.922 \pm 0.025$$
$$c_{edge} = 0.163 \pm 0.026 \qquad (7.8)$$
$$f_{edge} = 0.45 \pm 0.08$$

and for high EM fraction:

W/Z Fit CC events, HIGH EMFRAC

$\chi^2 = 13.878/18$

$M_z = 90.998 + -0.094$

ID	150
Entries	1256
Mean	86.66
RMS	6.176

M(ee) CC

$\chi^2 = 25.58/29$

$M_w = 80.126 + -0.085$

ID	150
Entries	17834
Mean	68.84
RMS	8.371

MT(ev) CC
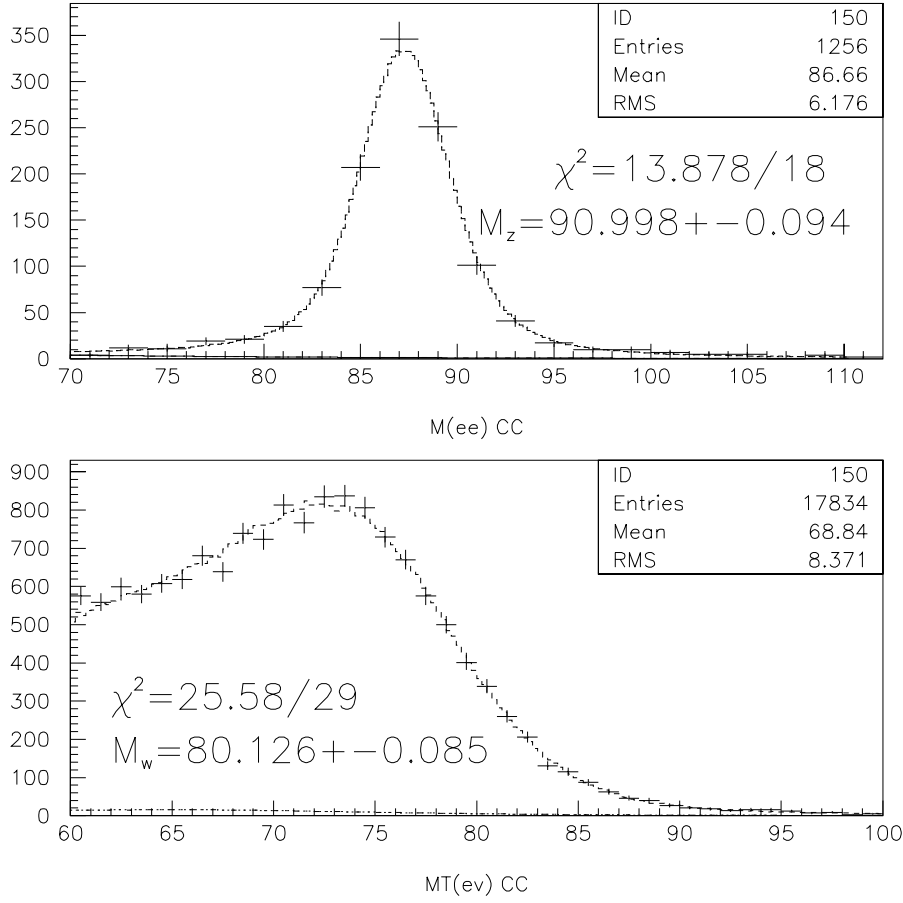
Figure 7.22: Top figure. C-C Z sample, Z mass distribution with one of the electron's EM fraction no less than 0.99. Bottom figure is the non-edge transverse W mass distribution with the electron's EM fraction > 0.99. The dotted line on both figures is the fit with the CMS mass templates.

W/Z Fit CC events, LOW EMFRAC

Top plot statistics box:

ID	150
Entries	756
Mean	87.13
RMS	6.507

$\chi^2 = 9.127/18$

$M_z = 91.447 +- 0.126$

M(ee) CC

Bottom plot statistics box:

ID	150
Entries	9841
Mean	69.19
RMS	8.671

$\chi^2 = 38.974/29$

$M_w = 80.904 +- 0.125$

MT(ev) CC

Figure 7.23: Top figure. C-C Z sample, Z mass distribution with one of the electron's EM fraction no more than 0.99. Bottom figure is the non-edge transverse W mass distribution with the electron's EM fraction < 0.99. The dotted line on both figures is the fit with the CMS mass templates.

138

$$\alpha_{edge} = 0.888 \pm 0.024$$

$$c_{edge} = 0.047 \pm 0.027 \qquad (7.9)$$

$$f_{edge} = 0.25 \pm 0.06$$

Using the above values, I fit for the Z mass and W mass . The low EM fraction sample yields (Figs. 7.24,7.25):

$$M_Z = 91.432 \pm 0.305 \text{ GeV}, \ \chi^2 = 7/17$$

$$M_W = 80.226 \pm 0.341 \text{ GeV}, \ \chi^2 = 65/29$$

and the high EM fraction events yields:

$$M_Z = 90.959 \pm 0.250 \text{ GeV}, \ \chi^2 = 12/13$$

$$M_W = 80.842 \pm 0.288 \text{ GeV}, \ \chi^2 = 35/29$$

$$M_Z^{\text{HIEMF}} - M_Z^{\text{LOEMF}} = -0.473 \pm 0.394 \text{ GeV}$$

$$M_W^{\text{HIEMF}} - M_W^{\text{LOEMF}} = +0.616 \pm 0.446 \text{ GeV}$$

The high and low EM fraction subsample Z masses agree well with each

139

W/Z Fit, LOW EMFRAC, EDGE
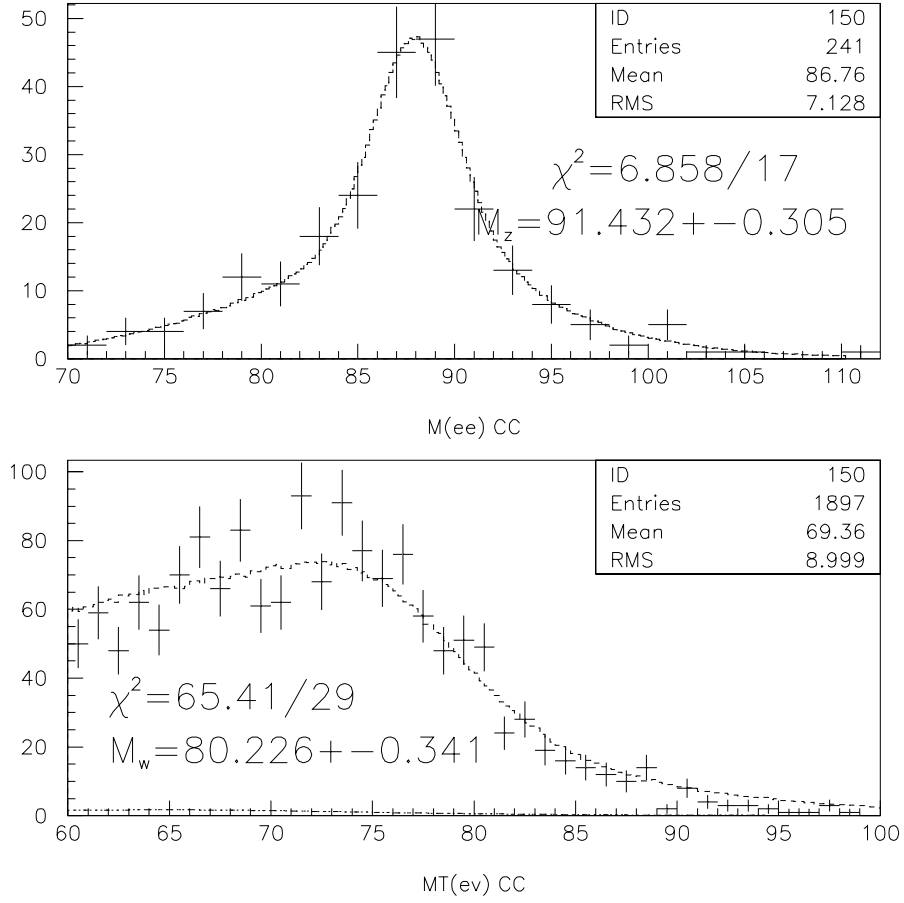
Figure 7.24: Top figure. $\widetilde{C}$-C Z sample, Z mass distribution with the edge electron's EM fraction no more than 0.99. Bottom figure is the edge transverse W mass distribution with the electron's EM fraction < 0.99. The dotted line on both figures is the fit with the CMS mass templates.
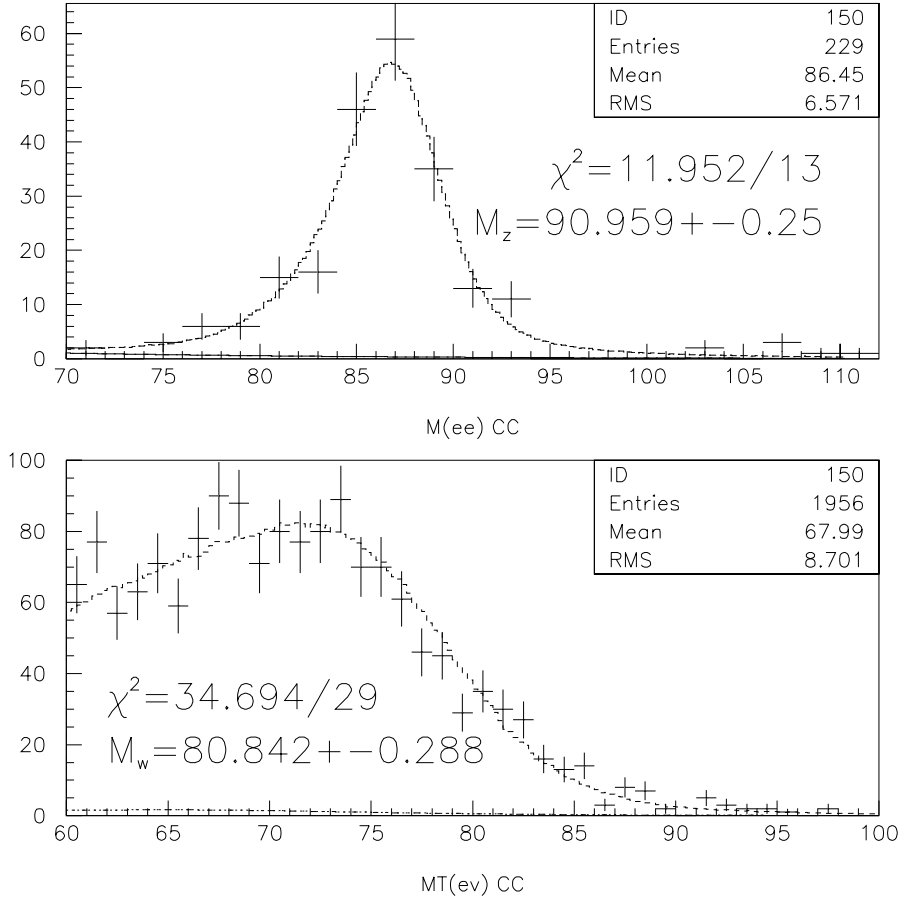
Figure 7.25: Top figure. $\widetilde{C}$-C Z sample, Z mass distribution with the edge electron's EM fraction no less than 0.99. Bottom figure is the edge transverse W mass distribution with the electron's EM fraction > 0.99. The dotted line on both figures is the fit with the CMS mass templates.
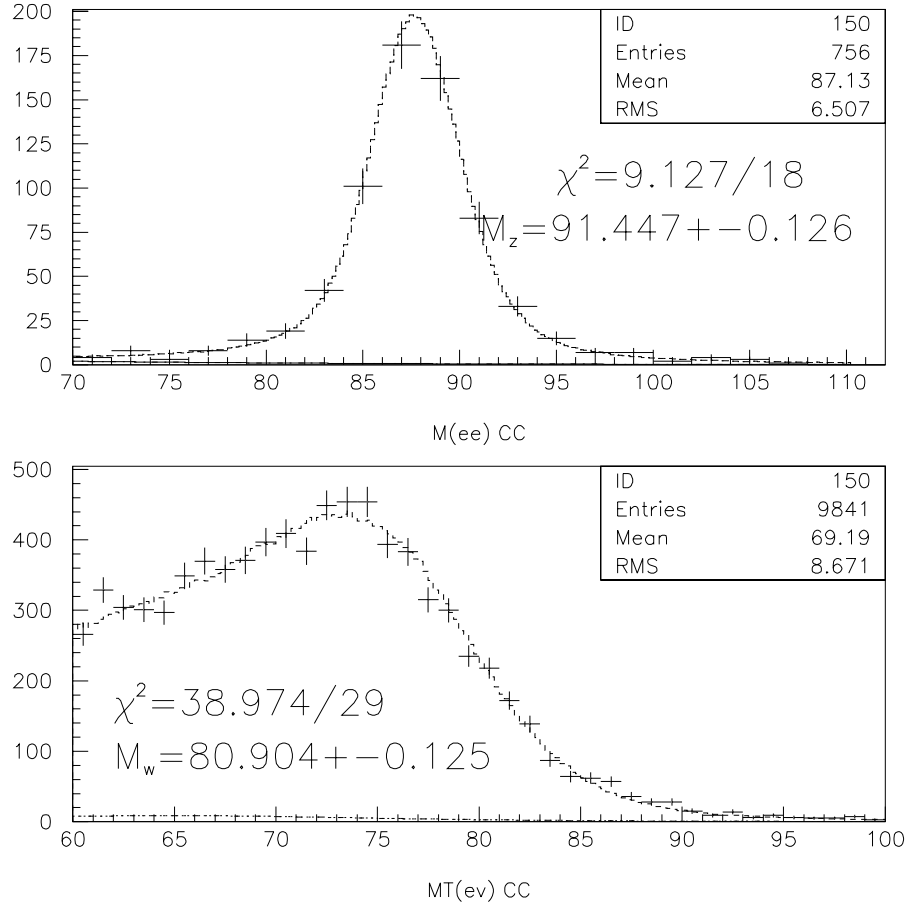
other, and with the LEP Z mass. The W mass measurements agree within errors too. It should be noted that the above errors are statistical only. The rough estimate is that adding systematic errors will almost double the total error, which makes the M_W results completely consistent between the low and high EM fraction bins.

The EM scale and resolution parameters depend on the electron EM fraction. We measure their values averaged over the electron EM fraction distribution. However, we demonstrated that we get the same W mass for low and high EM fraction samples. If averaging over the EM fraction range introduced some bias on the W mass measurement, we would not have obtained the same values of the W masses from distinctively different EM fraction samples. Therefore, it is acceptable to present analysis for all EM fraction sample if electrons from W and Z bosons have the same EM fraction distributions, as we observe to be the case.

7.3.3   Subsamples in distance to the module edge

As another consistency check I divided the C-C Z and W samples into four bins of distance to the edge of the module (Table 7.1). The fifth bin consists of the edge events. I correct the EM scale of one of the Z electrons, and fit

the W events for the W mass. I then plot the fitted W boson mass in bins of the distance.

	Distance to the edge
Edge bin	$0.0 < d_i < 0.1$ .or. $0.9 < d_i < 1.0$
Bin 1	$0.1 < d_i < 0.2$ .or. $0.8 < d_i < 0.9$
Bin 2	$0.2 < d_i < 0.3$ .or. $0.7 < d_i < 0.8$
Bin 3	$0.3 < d_i < 0.4$ .or. $0.6 < d_i < 0.7$
Bin 4	$0.4 < d_i < 0.6$

Table 7.1: Distance to the CC module edge of the electron in the C-C and $\widetilde{\mathrm{C}}$-C events. d is a fraction of a module width.

Each bin covers 20% of the CC module (Table 7.1). For the Z event to fall into any of the above bins one of the Z electrons had to be in the bin, and the other electron could be anywhere but in the same bin or the edge bin. This way each event falls into two bins at the same time because both its electrons are in some bins but never in the same bin. The edge bin sample is completely independent from the rest of the samples. For each bin, I call the electron that satisfies the bin criteria a tagged electron. I have generated Z mass templates and re-adjusted the EM scale of the tagged electron to make the fitted Z mass be equal to the LEP value. All four scales are consistent with the CC scale, and there is no remaining correlation with the distance to the edge (Fig. 7.27). Table 7.2 and Fig. 7.26 shows the fitted Z masses

143

before the CC EM scale (α_{cc}) re-adjustment. The errors are statistical only (Table 7.2 and Fig. 7.26).

Figure 7.26: Variation of the fitted Z mass across the CCEM module. The distance $d = 0.5$ corresponds to the middle of the CC module.

	Edge	Bin 1	Bin 2	Bin 3	Bin 4
Z mass (GeV)	91.199	91.089	91.048	91.240	91.341
Uncertainty (GeV)	0.203	0.123	0.124	0.120	0.135

Table 7.2: Z mass in bins of distance to the edge.

Then I divided the W event sample into the same five bins as well. Each bin has an independent set of events because each W event has only one electron. I used the EM scales calculated above, and fit for the W mass.

144

Fig. 7.27 shows the resulting W masses and also the W mass from the edge events. All W masses are consistent with each other (Table 7.3). The errors in the figure and table are statistical errors added in quadrature with errors on the EM scale. We see no evident W mass dependence on the electron's distance to the edge.

	Edge	Bin 1	Bin 2	Bin 3	Bin 4
W mass (GeV)	80.596	80.434	80.587	80.468	80.467
Uncertainty (GeV)	0.234	0.138	0.132	0.137	0.161

Table 7.3: W mass in bins of distance to the edge.

As a final cross check, I further subdivided the W edge sample into four sub-samples in bins of d_{edge} within the edge bin itself. I used the parameters from Eq. 7.6, and I didn't change or adjust them for each bin. I do not have enough events to constrain the edge parameters for each bin. However, the edge EM parameters that we determined (α_{edge}, c_{edge}, f_{edge}) are averaged over all edge electrons. Therefore, we could expect that averaging over some part of the edge region yields different values of those parameters. There is no evidence of the second gaussian in the EM response of the non-edge electrons and there should be a smooth transition between edge and non-edge regions. It does not introduces any bias to the W mass, however, if Z

145

and W azimuthal distributions are the same. The fitted W mass (Fig. 7.28) shows that at the available statistical level there is no observable dependence between the resulting W mass and the electron's distance to the edge. I would expect to see the dependence if more statistics were available.
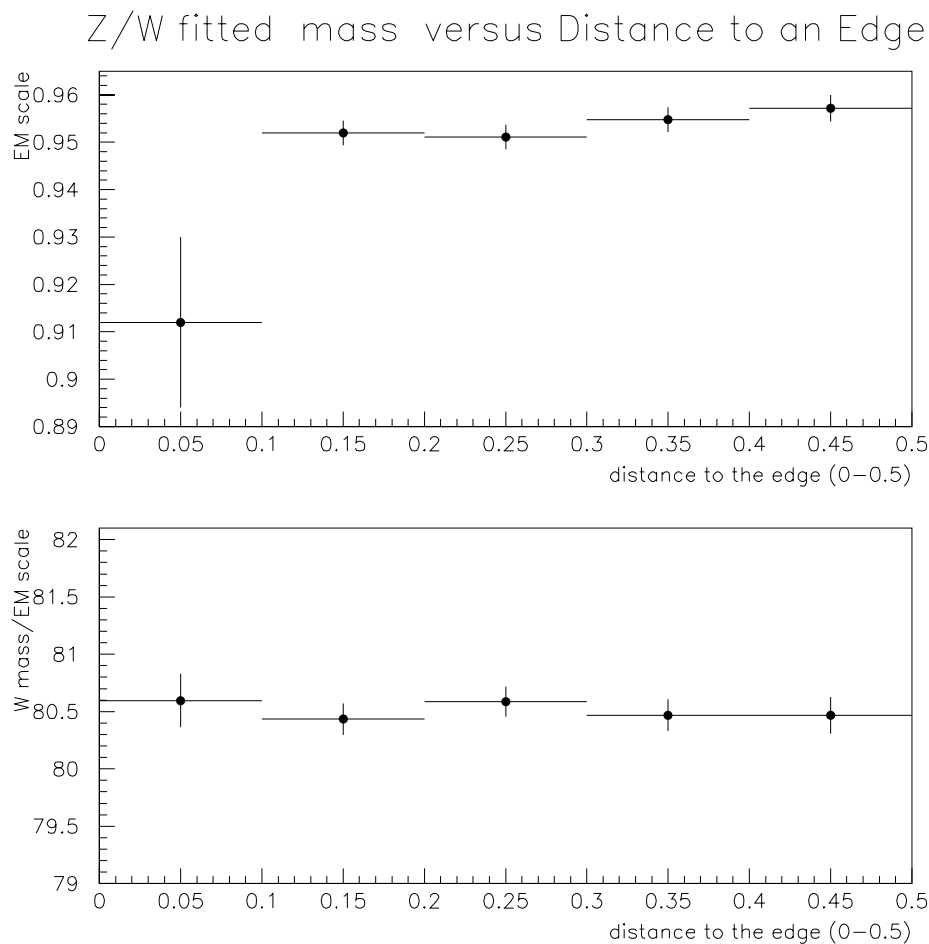
Figure 7.27: Variation of the EM scale across the CCEM module. The distance $d = 0.5$ corresponds to the middle of the CC module. For the edge bin $(d < 0.1)$ α_{edge} is plotted as the EM scale. The figure at the bottom is the fitted W boson masses. The EM scales from the top figure were used to generate MC W mass templates. I used a double Gaussian EM resolution for the CMS templates generation.
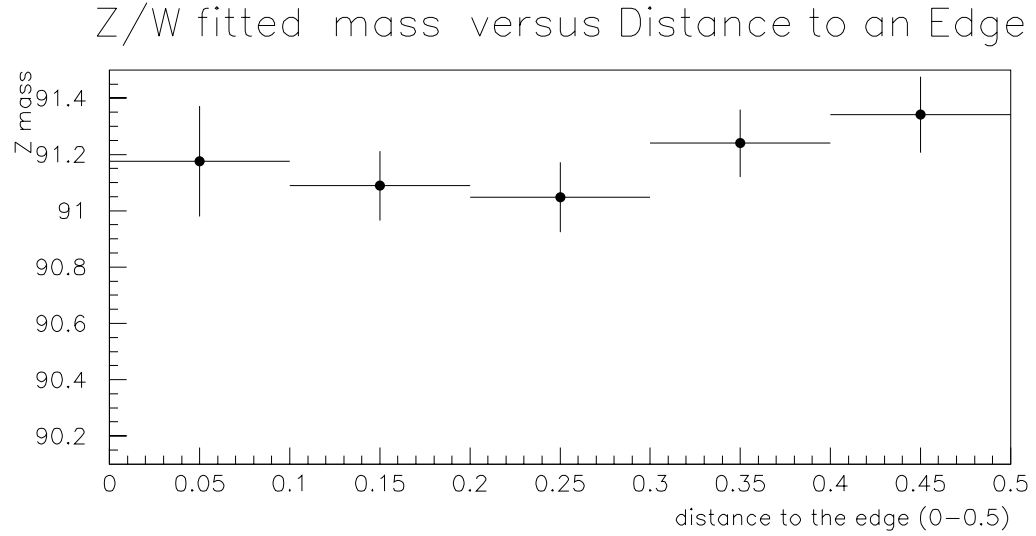
147
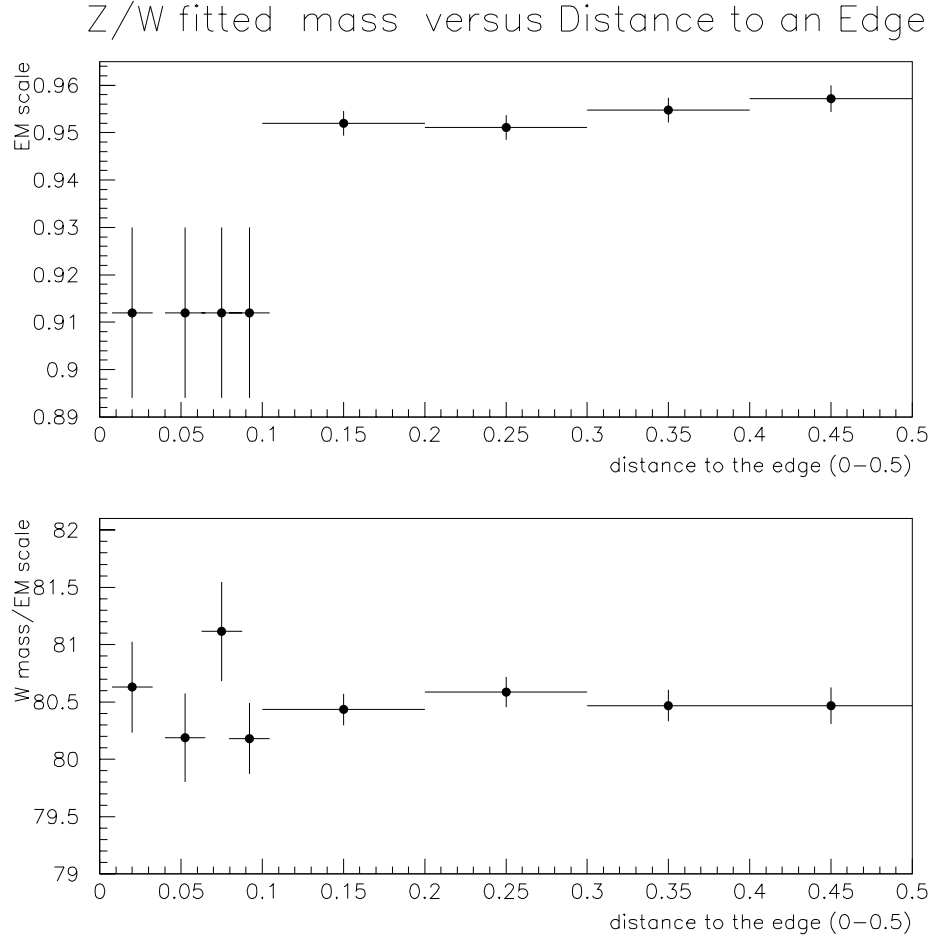
Figure 7.28: Variation of the EM scale across the CCEM module. The distance $d = 0.5$ corresponds to the middle of the CC module. The figure at the bottom is the fitted W boson masses. The EM scales from the top figure were used to generate MC W mass templates.

Chapter 8

Other parameters

8.1 EM offset

The electron's response in the CC calorimeter is parametrized as a linear function (Eq. [7.1]) and the determination of the EM scale has been already discussed in detail. Unlike the scale α, the EM offset δ should not depend on the properties of the material of the EM calorimeter but rather on the amount of material the particle crosses before reaching the calorimeter. The material is distributed uniformly in ϕ, and the edge electrons on average should lose the same amount of energy there as the non-edge electrons. I determine here the EM offset using $\widetilde{C}$-C events, and check that it is consistent with the C-C

149

analysis value.

The EM response function for the non-edge electrons is given by Eq. [7.1] and for the edge electron by Eq. [7.3]. We first correct the edge and non-edge electron energies by the non-edge offset ($\delta_{CC} = -160$ MeV [7]) and seek a residual EM offset for the edge electrons $\delta_{edge\ residual}$. From Eqs. [7.1,7.3], with the above correction and $M_{ee} = 2E_{cc}E_{edge}(1 - \cos\omega)$ we have:

$$< M_{ee} >= \alpha\, M_z^{LEP} + < f > \delta_{edge\ residual} \tag{8.1}$$

where α is an effective EM scale equal to $0.34\sqrt{\alpha_{cc}\alpha_{edge}} + 0.66\alpha_{cc}$; ω is the angle between the two electrons; M_{ee} is the measured dielectron mass; and E^{cc} is the energy of the non-edge electron. The function f is $\frac{E^{cc}(1-\cos\omega)}{M_{ee}}$. The factors 0.34 and 0.66 in the α equation are f_{edge} and (1-f_{edge}).

The average M_{ee} is a linear function of f, with the slope equal to the residual edge EM offset. I plot the dielectron invariant mass in bins of f. Figure 8.1 shows that the slope is consistent with zero, with $\chi^2 = 8.9/9$. This means that δ_{edge} is consistent with the δ_{cc}, because the electrons' energies have been corrected already by the δ_{cc} offset. Since I do not see any evidence that the edge electron's EM offset is different from the non-edge electron, I have
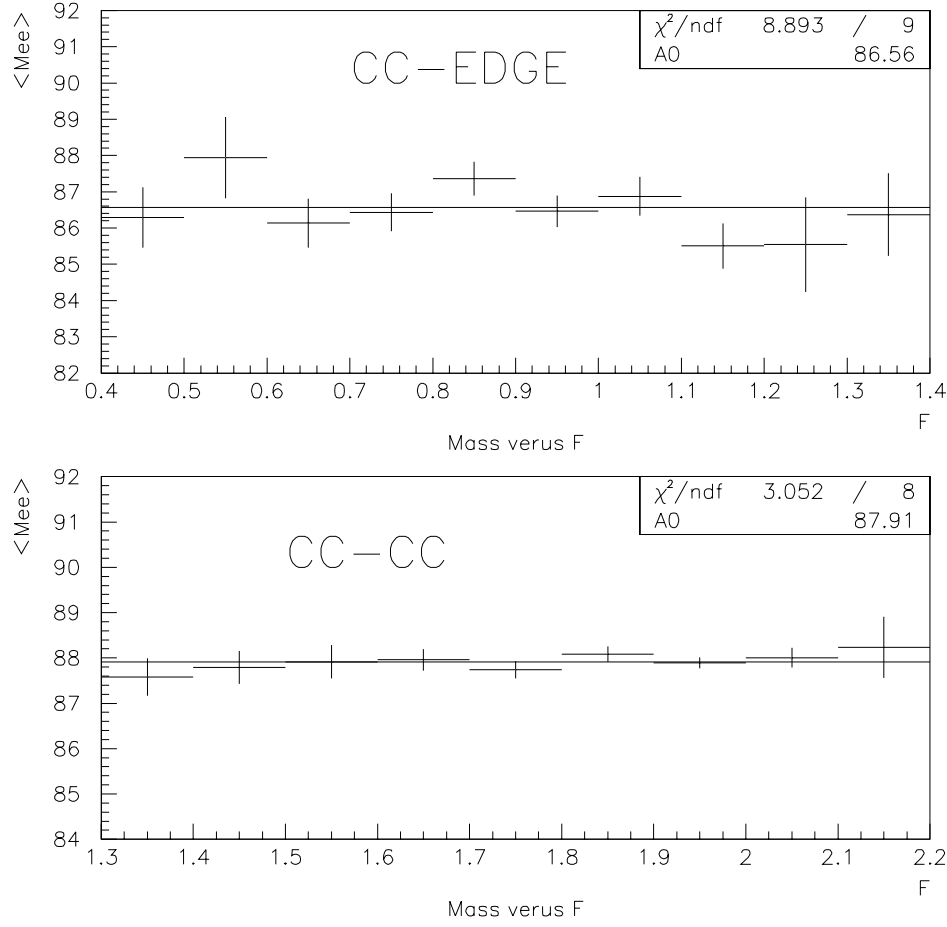
Figure 8.1: Average dielectron invariant mass as a function of f (Eq. 8.1) fit with the $< M_{ee} >=$ const function, for the $\widetilde{C}$-C Z sample (top figure) and C-C Z sample (bottom plot). The slope of the line would be equal to any residual EM offset. Both data distributions are consitent with zero residual offset.

assumed that edge electrons and non-edge electrons have identical offsets.

8.2 Underlying event energy correction

Some part of the recoil energy is deposited in the same calorimeter cells as the electron, and is automatically included in the electron's energy. This energy has to be added to the recoil and subtracted from the electron. In fact, the energy that has to be added to the recoil is not the same as the energy that needs to be subtracted from the electron due to the zero suppression in the calorimeter readout. This is true for non-edge and edge electrons. If it were not for the electron, the cell under the electron shower might not have had enough energy deposited by the recoil to exceed the readout threshold and would have been zero suppressed. The difference between the energy subtracted from the electron and added to the recoil has been estimated to be 212 ± 25 MeV [7].

The energy added to the recoil depends on the recoil momentum component in the electron window, the electron's η, and the luminosity. If the recoil momentum is $\vec{U}$, and the recoil component parallel to the electron's direction is $U_{||}$, then the energy which has to be subtracted from the electron

ΔE and added to the recoil is $\Delta U_{\parallel}$.

The amount of recoil energy deposited under the electron depends on the distribution of the energy flow of the recoil, and is independent of the electron's ϕ. The core of the electron's shower is contained in a 0.2x0.2 cone in $\eta - \phi$ space. The total cone where the electron's energy is measured is 0.5x0.5. The size of the EM module ϕ is 0.2 rad. Every cone under the edge or non-edge electron's shower contains more than one EM module edge. Thus the effect that the module's edge has on the amount of recoil energy deposited under the electron ($\Delta U_{\parallel}$) should be the same for edge and non-edge electrons, and in the analysis, I assumed the same $\Delta U_{\parallel}$ correction as in the non-edge analysis.

8.3 $U_{\parallel}$ efficiency

When significant recoil energy lies close to the electron direction, it broadens the electron's EM shower and in some cases can cause the electron to fail some quality cuts which leads to a $U_{\parallel}$-dependent loss in efficiency. Electron isolation is the variable that is most sensitive to the value of $U_{\parallel}$. Most of the inefficiency caused by large $U_{\parallel}$ is due to the electron failing the isolation

cut. The $U_\parallel$ efficiency has been estimated in the CC W mass analysis and is represented as a function of $U_\parallel$. The efficiency is constant up to a certain positive value of $U_\parallel = u_0$, and drops linearly after that with slope s_0. The absolute scale of the efficiency is not important, but the dependence on $U_\parallel$ is. Therefore, I compare the isolation distribution of the central and edge electrons to see if there is any difference in their dependence on $U_\parallel$.

The isolation of an electron is basically the fraction the electron's energy outside the cone of radius $R = 0.2$. R is the distance in $\phi - \eta$ space ($R = \sqrt{\Delta\phi^2 + \Delta\eta^2}$).

$$ISO = \frac{E(R < 0.4) - E^{EM}(R < 0.2)}{E^{EM}(R < 0.2)} \tag{8.2}$$

where $E(R < 0.4)$ is sum of the energy deposited in the cells of the CC EM calorimeter and hadronic calorimeter within the radius 0.4 from the electron's shower centroid. $E^{EM}(R < 0.2)$ is the energy deposited in the four EM layers inside the $R < 0.2$ cone.

In Fig. 8.2 I plot the ISO distribution of edge and non-edge electrons, normalized by the number of events. The average ISO of the non-edge CC electron is +0.38 in comparison to the +0.41 of the edge electron, or 1.08±0.15 lower than the edge electron isolation. Though the difference is not statistically significant, we still decided to investigate a possible dependence.

ID	4969
Entries	4024
Mean	0.3778E−01
RMS	0.2564E−01

coef=1.0

ISO

ISO sig for cc

ID	4969
Entries	4024
Mean	0.4037E−01
RMS	0.2681E−01

coef=1.08 ± 0.15

ISO

ISO sig for cc
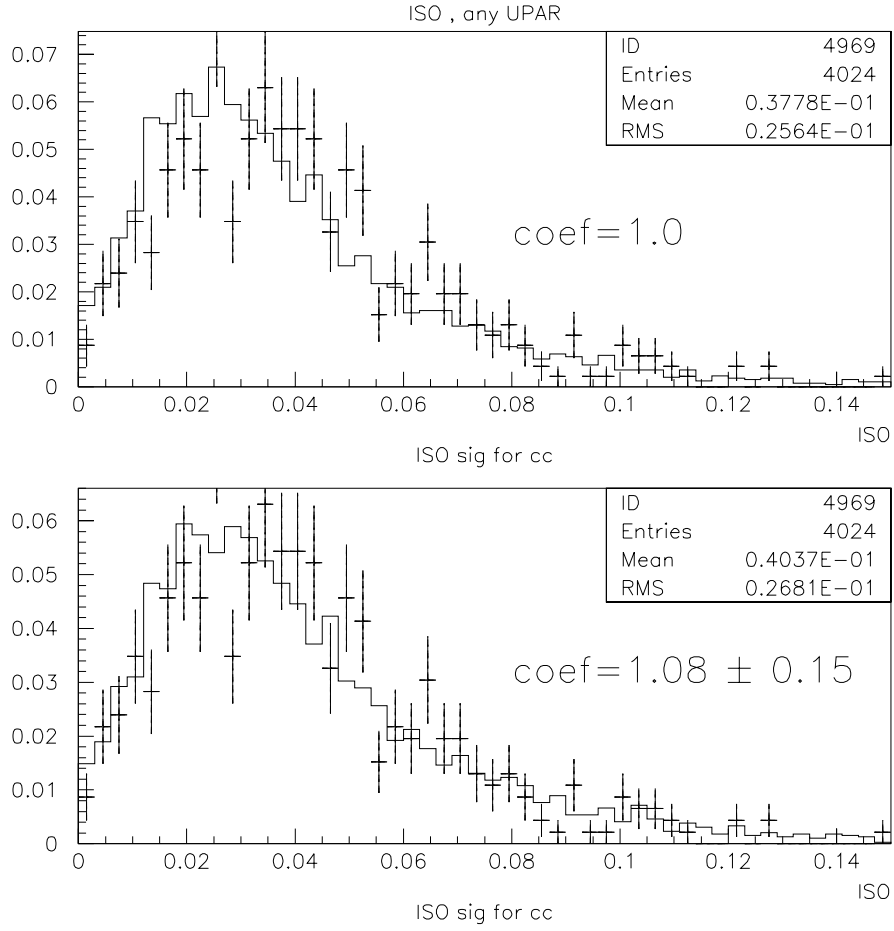
Figure 8.2: Edge (points on both figures) and non-edge (solid line on both figures) electron's isolation distributions. On the bottom figure the non-edge ISO is multiplied by 1.08 to obtain the same average ISO as the edge electron average ISO.

Part of the reason for the difference is that the $E^{EM}(R < 0.2)$ counts only energy in the EM calorimeter, and edge electrons have lost some of their energy in the region of distorted electric field. The $E(R < 0.4) - E^{EM}(R < 0.2)$ can be rewritten as $E^{HAD}(R < 0.4) + E^{EM}(0.2 < R < 0.4)$. $E^{EM}(0.2 < R < 0.4)$ is the same for the edge and non-edge electrons. $R > 0.2$ is 1 CC module away from the shower centroid and the position of the centroid (inside the edge region or outside) does not matter any more. So the numerator is the same, and the denominator is smaller, which leads to higher ISO of the edge electrons. However, I found that a smaller $E^{EM}(R < 0.2)$ accounts only for 35% of the difference between average ISO for $\widetilde{C}$-C and C-C Zs. Another source of the higher ISO could be the worse EM resolution of the edge electrons. The $E^{EM}(R < 0.2)$ distribution is broader, and it affects the ISO shape.

Higher ISO means lower electron identification efficiency. But the overall efficiency is irrelevant, and only the dependence on $U_{\parallel}$ matters.

To see if the $U_{\parallel}$ efficiency is affected I plot the normalized ISO of the electrons when $U_{\parallel}$ in the event is larger, or smaller, than 0. As above I calculated the factor by which the non-edge ISO has to be scaled to became equal to the edge ISO. The factor is 1.08 ± 0.21 for $U_{\parallel} < 0$ GeV, and is

156

1.06 ± 0.19 for $U_{\parallel} > 0$ GeV. Statistically these two factors are the same, which indicates no shape distortion of the $U_{\parallel}$ efficiency distribution. So I use the same $U_{\parallel}$ efficiency for the edge electrons as for non-edge electrons in the analysis.

8.4   Radiative event corrections

Due to the different EM response in the CC edge, the radiated photon has to be handled differently for edge and non-edge electrons. When a photon is merged with the edge electron in the MC, its energy is added to the electron and then the total energy is smeared by the edge EM response and resolution functions. The coalescence radius is $R = 0.3$. The radiated photon can be within the coalescence radius of the edge electron, but outside the edge region. In this case, the photon should presumably be smeared by the non-edge EM resolution function. Smearing by the edge EM resolution function results in a smaller energy contribution from the radiated photon.

If the photon is closer than a certain $\Delta\phi$ (the difference between electron's and photon's azimuthal angle) to the electron it is within the edge region and should be smeared with the edge EM response function. If it is farther than

$\Delta\phi$ it should be smeared with the non-edge EM function. But in the MC we still smear it with the edge EM function, which results in a smaller, by ΔE, contribution from the photon's energy. Figure 8.3 shows ΔE as a function of the cutoff $\Delta\phi$. From the Figure, the energy difference at half the edge band ($\Delta\phi = 0.01$) is 3.5 MeV, which results in 1-2 MeV shift in the W mass. This was deemed negligible, and the MC has not been modified. In the analysis, we smear radiated photons with the edge EM response and resolution function.

8.5 W and Z EM fractions

The edge EM response parameters Eq. [7.6], vary somewhat with the EM fraction (Figs. 7.8, 7.10). So it is important that the Z and W event samples have the same EM fraction distributions. Figure 7.21 shows that there is no statistically significant difference between them, so no corrections have to be made, and the edge parameters (Eq. [7.6]) determined with the Z events can be used to describe the EM response in the W events.

158

ΔE Single − Double Gauss versus cut in Δφ
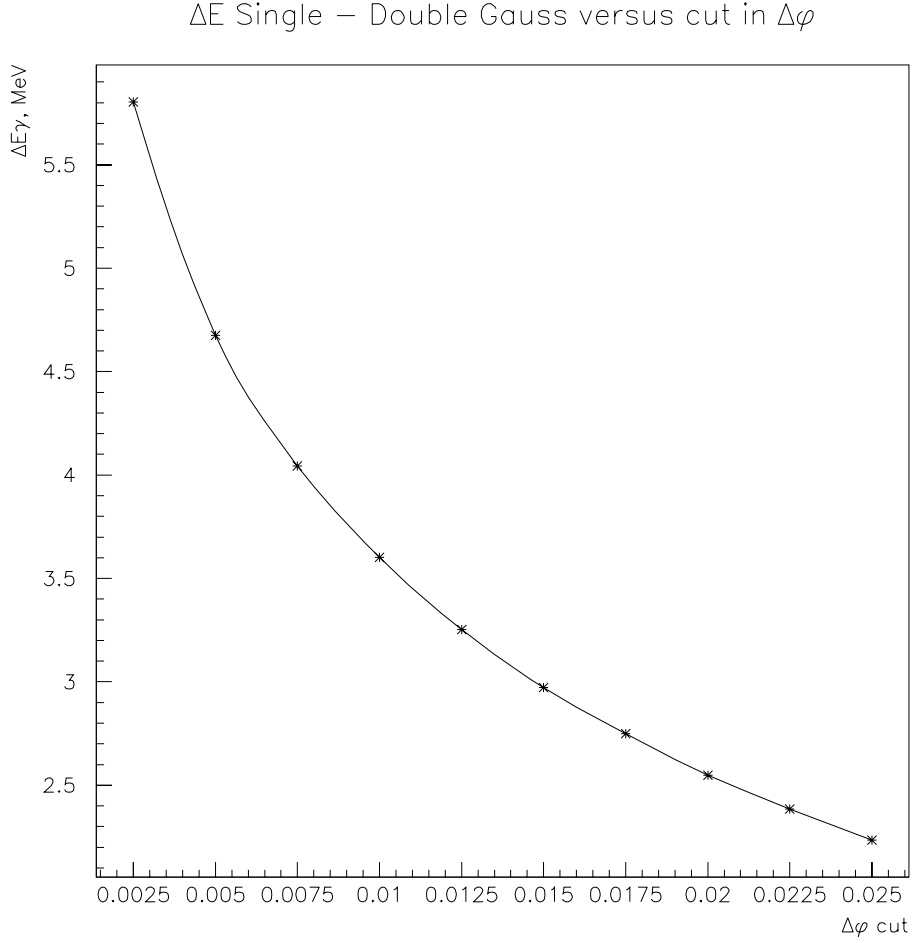
Figure 8.3: Radiative events correction. If the radiated photon is more than $\Delta\phi$ away from the edge electron the photon energy has to be smeared in the MC with the non-edge EM resolution function and added to the electron's energy. If it were still smeared with the edge EM resolution function the average photon's energy contribution to the electron's energy would be smaller by ΔE. I plot ΔE as a function of $\Delta\phi$. The points on the plot are obtained using CMS MC simulations.

8.6 Recoil response and resolution

The recoil does not depend on the position of electron in the calorimeter. Therefore, the recoil response and the resolution are the same as described in the C-C W paper [7].

8.7 Alignment and electron angular resolution

The alignment of the CDC and CC calorimeter is described in the CC W analysis[7].

The calorimeter centroid position and the vertex position are used to define a track's ϕ.

$$\tan\phi = \frac{y_{cal} - y_{vtx}}{x_{cal} - x_{vtx}}$$

x_{vtx}, y_{vtx} of the primary vertex position is known with good precision from the beam position. The calorimeter ϕ resolution does change across the EM module [18]. It is best when the electron's position is at the edge of the cell's pads. For 50 GeV electrons, the spatial resolution is about 20% better at the edge of a pad, compared to the middle of the pad. However, the effect of the

better angular resolution on the W mass is included in the energy resolution because the electron's energy and angular resolutions both contribute to the width of the Z mass distribution, with the angular resolution being a smaller correction. Small variations of angular resolution get accomodated by a change in the energy resolution.

The calorimeter centroid z position and track centroid z position are used to define a track's θ. The calorimeter z resolution is the same for edge and non-edge electrons because there is no edge in z. The track's z in the CDC is measured with delay lines. The average drift time in the W and Z edge events is different from non-edge events (because as noted in the Section 2 the middle of the CDC modules is aligned with the CCEM modules edges), but the difference in the arrival time between two ends of the delay line is not affected. So the CDC z resolution is the same for edge and non-edge electrons.

8.8 Trigger efficiency

The electron EM2_EIS_HI trigger efficiency as a function of the electron's E_t (turn-on curve) has been taken to be the same as in the CC W analysis.

The possible effect on the edge electron is a 5% reduction in the electron's energy in 34% of the events, which can at most lead to a 300 MeV shift in the electron's energy for a 20 GeV electron. Such a shift has negligible effect on the trigger efficiency.

The $\not{E}_T$ trigger turn-on curve does not depend on the position of the electron and is the same as in [7].

8.9 Theoretical model

We used the same theoretical model to describe the production and decay of the W boson as in previous W mass analyses. The error on the W mass due to uncertainties on parton luminosity, the choice of the PDF function, uncertainty due to the W boson p_t distribution model remains unchanged.

Chapter 9

Mass fits and error analysis

9.1 Mass fits

I extract the W boson mass by fitting distributions of various quantities with corresponding Monte Carlo templates. As in the EC and CC analyses, I use distributions of W transverse mass $(m_t(W))$, electron transverse momentum $p_t(e)$, and neutrino transverse momentum $p_t(\nu)$. I generate a set of MC distributions of each of the above quantities for different central values of W boson mass, called MC mass templates. I use the maximum likelihood method described in Section 4.2 for the W mass fit. The background is added to the MC templates with the fraction from Chapter 6. The fits yield (see

163

Fig. [9.2,9.3,9.4]):

$$M_W = 80.596 \pm 0.234 \text{ GeV}, \quad \chi^2 = 45/29 \quad m_t(W) \text{ fit.}$$

$$M_W = 80.733 \pm 0.263 \text{ GeV}, \quad \chi^2 = 38/39 \quad p_t(e) \text{ fit.} \qquad (9.1)$$

$$M_W = 80.511 \pm 0.311 \text{ GeV}, \quad \chi^2 = 45/39 \quad p_t(\nu) \text{ fit.}$$

Errors are statistical only. The fitting windows are:

$$60 < m_t(W) < 90 \text{ GeV}, \quad m_t(W) \text{ fit}$$

$$30 < p_t(e) < 50 \text{ GeV}, \quad p_t(e) \text{ fit} \qquad (9.2)$$

$$30 < p_t(\nu) < 50 \text{ GeV}, \quad p_t(\nu) \text{ fit}$$

Figs. [9.5,9.6,9.7] show the sensitivity of the fitted W mass to the choice of the fitting windows. Changing the fitting window results in a deviation of the fitted W mass from the values in Eq. 9.1 due to statistical fluctuations. In the Figures, the points show the observed deviation, while the shaded area indicates the 68% probability contour. The dashed line represents the statistical error of the nominal fit. Most of the data points are contained inside the shaded area. The contours were obtained by generating an ensemble of MC W samples (each of the same size as edge W sample), fitting them for

164

W/Z Fit, EDGE

ID	150
Entries	470
Mean	86.61
RMS	6.865

$\chi^2 = 10.447/19$

$M_z = 91.199 +- 0.203$

M(ee) CC

ID	100
Entries	201
Mean	91.16
RMS	0.7361
χ^2/ndf 6.677 / 152	
P1	1.238
P2	0.2030
P3	91.20
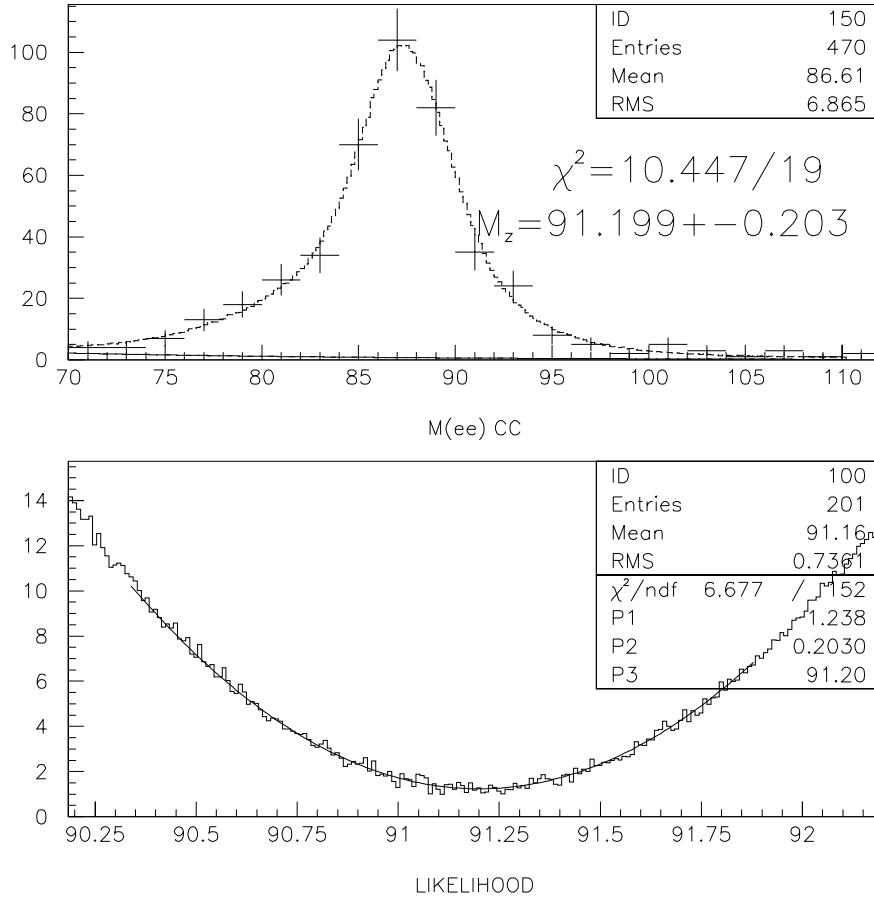
LIKELIHOOD

Figure 9.1: $\widetilde{C}$-C Z mass and fit -log(likelihood) distribution. Z mass is fitted with CMS templates.
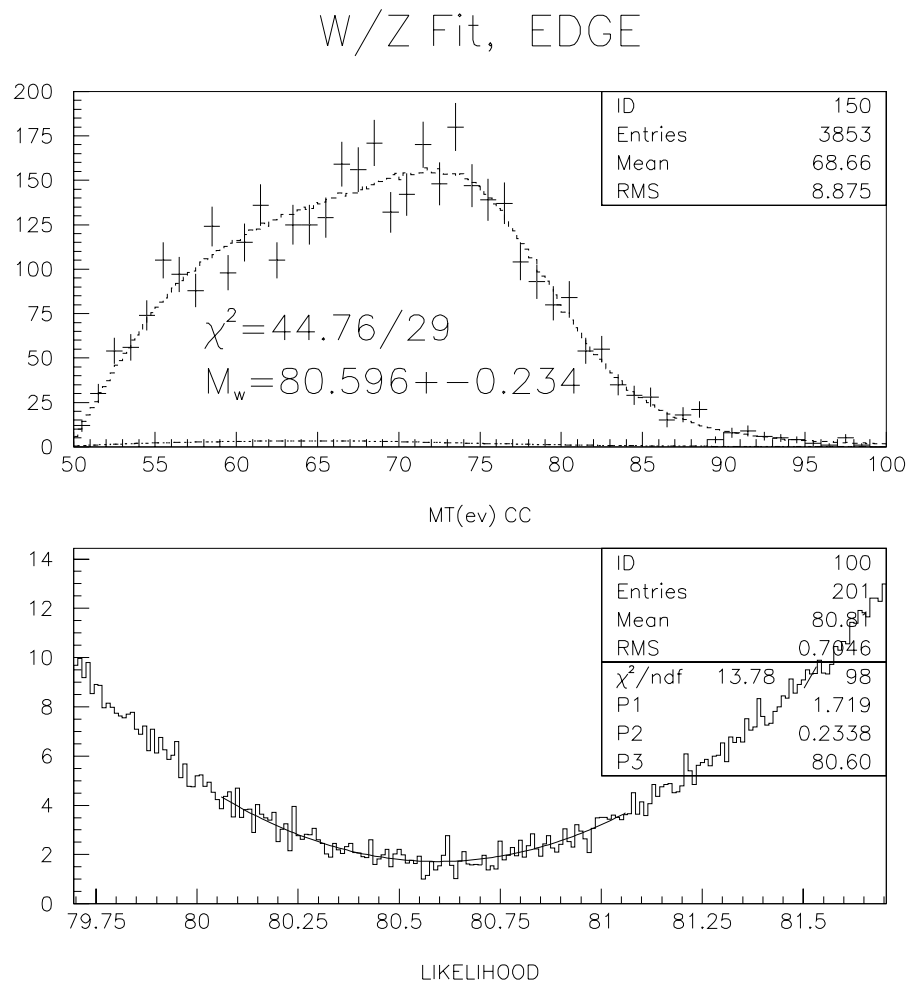
Figure 9.2: Edge W transverse mass distributions, fitted with CMS templates and the fit -log(likelihood).
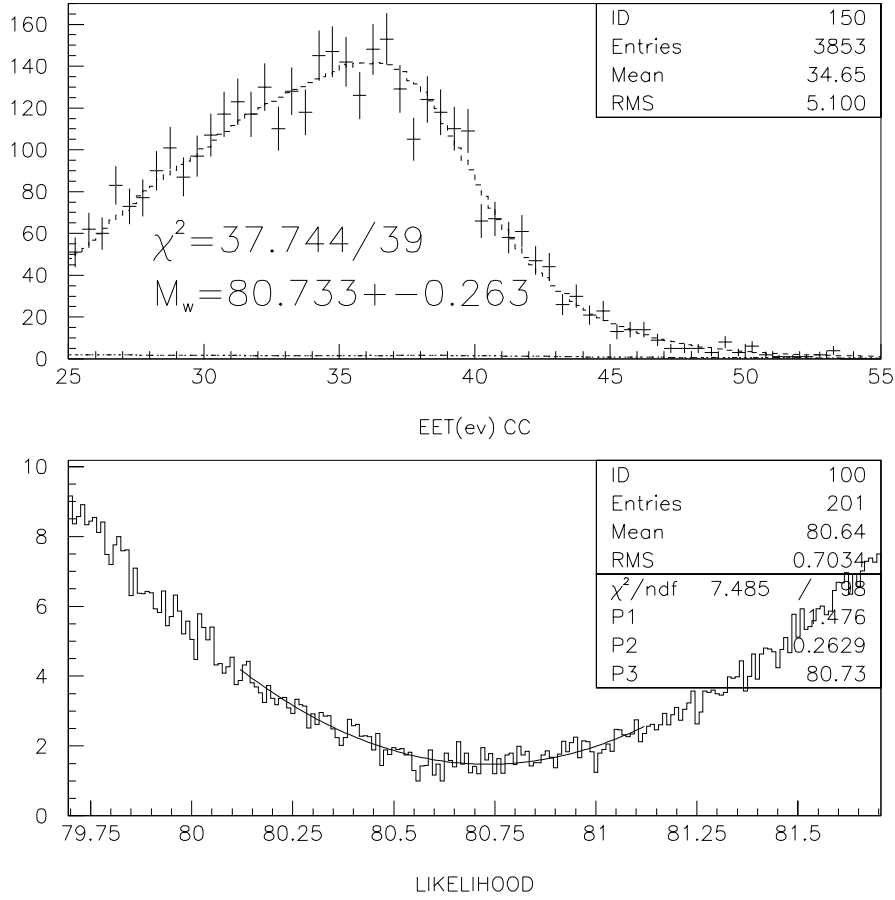
Figure 9.3: Edge W sample. Electron's $p_t(e)$ distribution fitted with the CMS templates and the fit -log(likelihood).
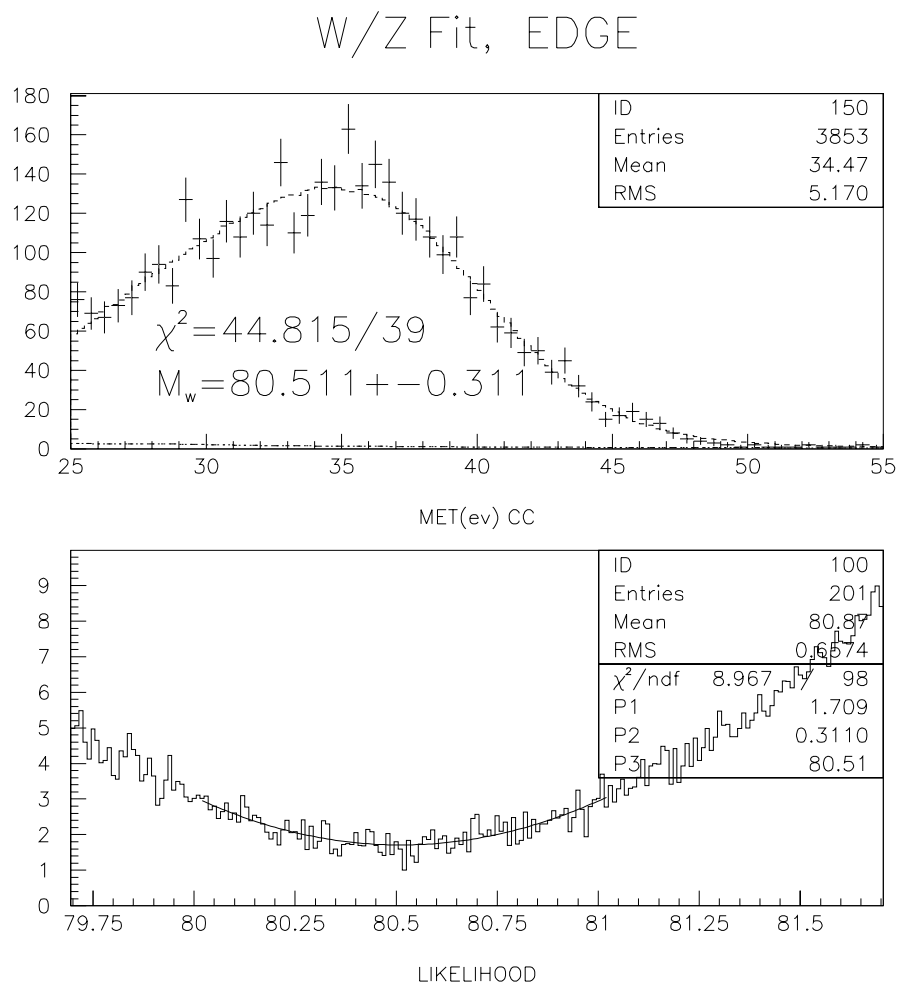
Figure 9.4: Edge W sample. Missing E_t distributions fitted with the CMS templates and the fit -log(likelihood).

the W mass and, for each fitting window, determining a fitted W mass interval containing 68% of samples. The neighboring points are not independent because we fit the same set of events but just changing the fitting window.

9.2   Systematic error analysis

The fitted W mass is a function of all the parameters used in the MC model. It also is a function of the experimental data (W statistics). I combine all the parameters into the parameter vector $\vec{P}$. Data is one of the parameters which I call w_{edge}. The full list of the parameters is presented below.

- W mass statistics w_{edge} (statistical error)

- EM scales α_{cc} and α_{edge}

- EM offset δ_{cc}

- CDC scale β_{cdc}

- EM resolutions (constant terms) c_{cc} and c_{edge}

- Fraction of events with "edge" EM resolution f_{edge}

- recoil response α_{had}, representing jointly α_{rec} and β_{rec}

169
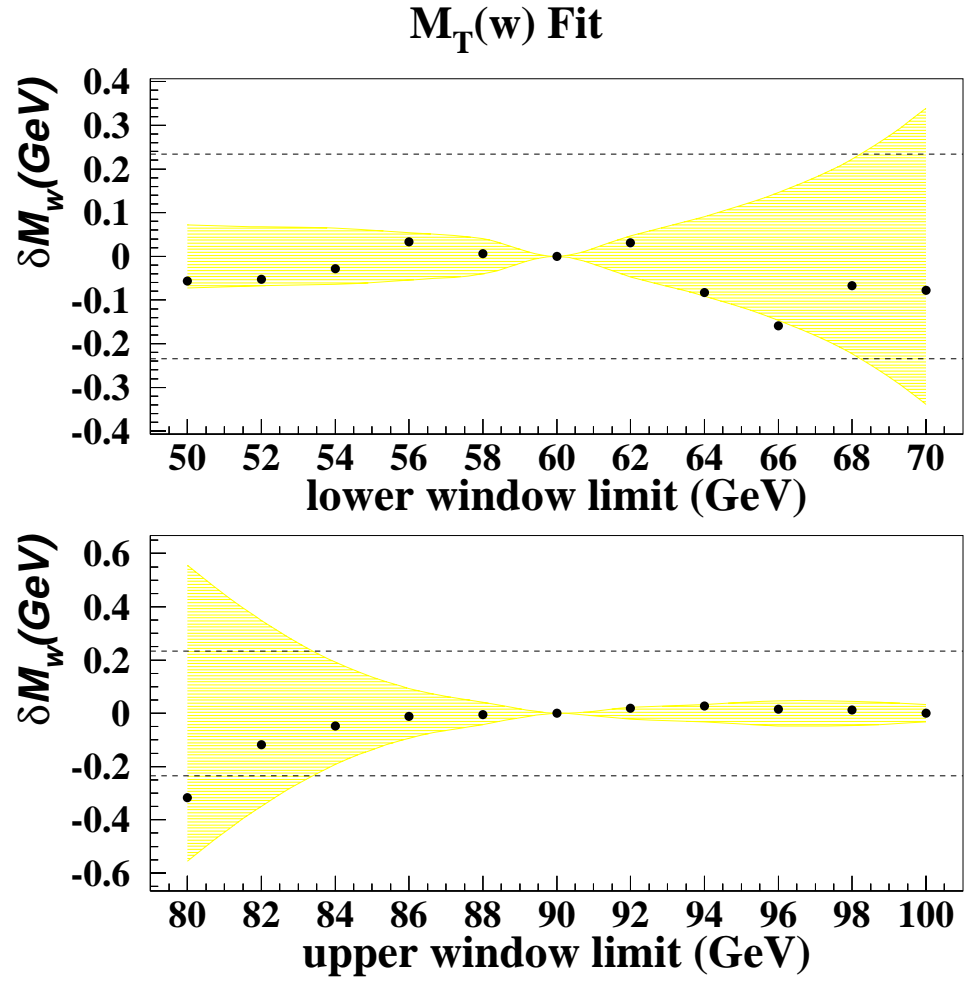
Figure 9.5: Variation of the fitted W mass with the $m_t(W)$ fit window limit.
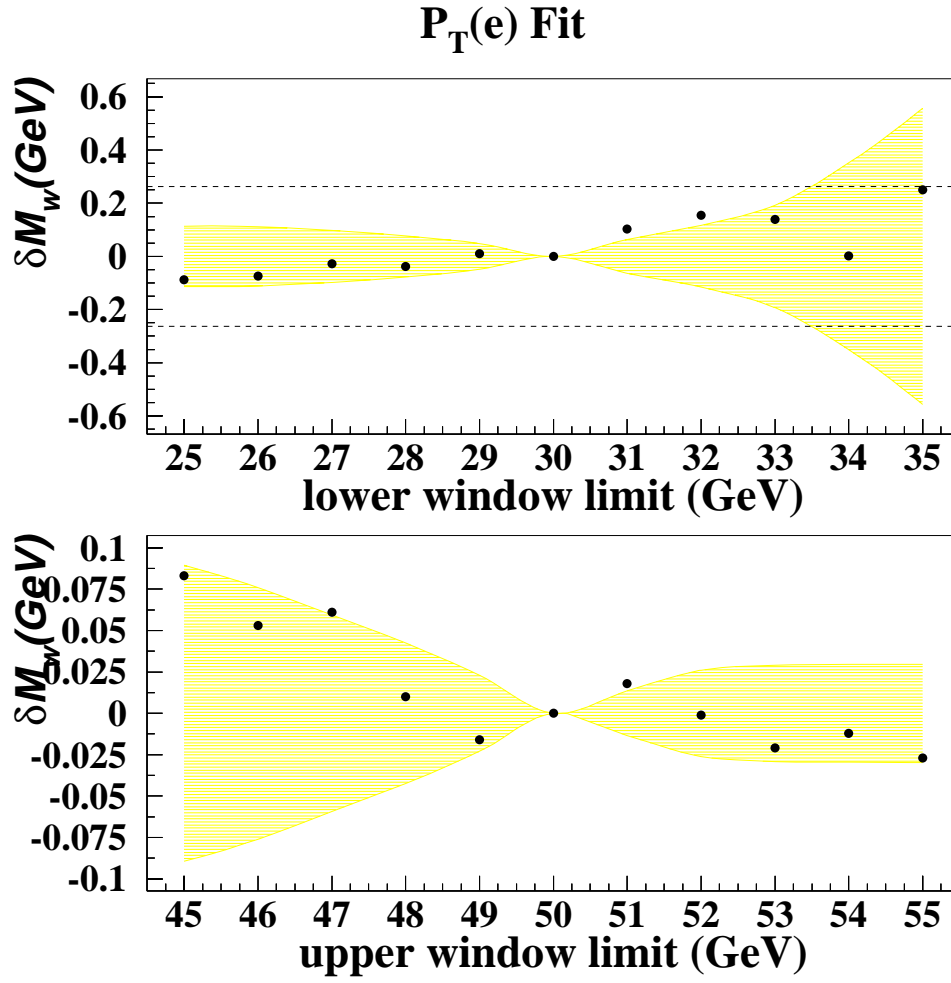
Figure 9.6: Variation of the fitted W mass with the $p_t(e)$ fit window limit.
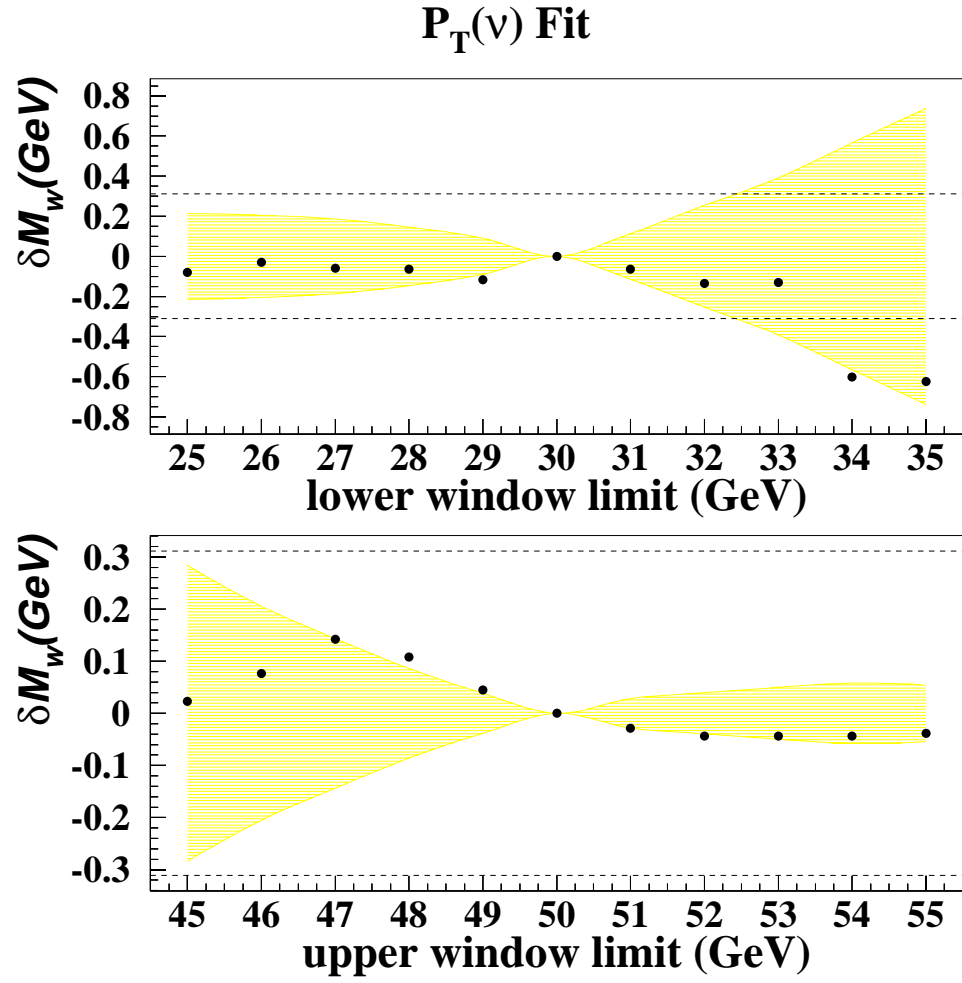
Figure 9.7: Variation of the fitted W mass with the $p_t(\nu)$ fit window limit.

- recoil resolution c_{had}, representing jointly the sampling term s_{rec} and α_{mb}

- $U_{\|}$ correction u_{cc}

- $U_{\|}$ efficiency ε_{cc}, representing jointly the efficiency cutoff u_0 and slope s_0

- background b_{cc}

- radiative corrections as a function of coalescing radius r_0 and also an uncertainty due to events with two radiated photons.

- theoretical modeling t represented by a set of parameters: PDF uncertainty, W width $\Gamma(W)$, W P_T spectrum, parton luminosity β

The recoil response is parametrized by two correlated parameters α_{rec} and β_{rec} but it is represented by a single parameter α_{had} in the W parameter vector $\vec{P}$. The uncertainty on the W mass from α_{had} was calculated by adding in quadrature uncertainties from two uncorrelated variables along the main axes of the α_{rec}-β_{rec} error ellipse. The details are given in [7]. The uncertainty from the recoil resolution c_{had} was calculated in a similar way. The $U_{\|}$ efficiency is defined by two highly correlated parameters u_0 and s_0.

The uncertainty on the W mass due to the $U_{\parallel}$ efficiency was calculated by fixing u_0 and propagating the error from the slope s_0 only. All theoretical model parameters are assumed to be independent.

To get the uncertainty of the measured W mass, $\sigma(M)$, I propagate the uncertainty of the parameters into the uncertainty of the W mass with the method below.

The measured W mass M_W is a function F of parameters $\vec{P}$.

$$M_W = F(\vec{P_i})$$

I take the convention that the lower case Latin indices run over set of parameters, upper case Latin indices denote the set of measurements and Greek indices denote the set of W mass measurements. I also assume a summation over the repeated indices unless noted otherwise.

The variation ΔM is assumed to be a linear function of the vector of variation of the parameter ΔP_i. The variation ΔM_i due to a variation of the parameters P_i is (there is no implicit summation here)

$$\Delta M_i = \frac{\partial F}{\partial P_i}\Delta P_i \equiv D_i \Delta P_i$$

The full mass error is

$$\Delta M \equiv D_i \Delta P_i \quad \text{(with summation convention)}$$

where D_i is the vector of derivatives.

To obtain derivatives for each parameter P_i, I generated MC mass templates with the parameter P_i varied by one standard deviation, $\pm\sigma(P_i)$. To eliminate the effect from finite W statistics, I also generated a sample of W events with unchanged parameters for comparison. I fit the MC sample with templates for the W mass and get two values $M_W(P_i + \sigma(P_i))$ and $M_W(P_i - \sigma(P_i))$. The derivative D_i is then

$$D_i = \frac{M_W(P_i + \sigma(P_i)) - M_W(P_i - \sigma(P_i))}{2\,\sigma(P_i)}$$

The parameters P_i are not independent and, if their correlations are given by the covariance matrix E, then the error on the single W mass measurement is

$$\sigma(M) \equiv\, <\Delta M \Delta M^T> = D_i\, E_{ij}\, D_j \qquad (9.3)$$

175

The parameters used in the MC are constrainted by the set of measurements. Some of the measurements are correlated and not independent of each other, and some are uncorrelated. We take those measurements that use different data samples to be uncorrelated. For example the measurement of the non-edge CC Z mass is uncorrelated with the measurement of α_{edge} because these measurements are based on different data samples. Below is the full list of measurements that help constrain the parameters used in our MC model. In the parentheses I list all the parameters the measurement helps constrain.

- The Z mass fits for α_{edge}, using $\widetilde{\mathrm{C}}$-C Z's (α_{edge})

- The Z mass fits for c_{edge}, using $\widetilde{\mathrm{C}}$-C Z's (c_{edge})

- The Z mass fits for f_{edge}, using $\widetilde{\mathrm{C}}$-C Z's (f_{edge})

- The Z mass measurements M_Z^{cc-cc}, using C-C Z's
  (CDC scale β_{cdc}, δ_{cc}, radiative events correction, α_{cc}, two γ radiative event correction, parton luminosity β)

- CDC z calibration θ_{cdc} (CDC scale β_{cdc})

- CC EM offsets δ_{cc}, using C-C Z's (δ_{cc})

- Gaussian width fitted to the Z peak σ_Z^{c-c}, using C-C Z's (c_{ccem})

- p_t balance in Z events, using C-C Z's (α_{had})

- Width of p_t balance in Z events σ_{p_t}, using C-C Z's (c_{had})

- measurements of $U_{\parallel}$ correction $(U_{\parallel})$

- $U_{\parallel}$ efficiency $(U_{\parallel}$ efficiency)

- constraints on theoretical model (PDF uncertainty, W width $\Gamma(W)$, W p_T spectrum, parton luminosity parameter β)

The Z mass fits for α_{edge}, c_{edge} and f_{edge} are correlated with each other, and with the M_Z^{C-C} and σ_Z^{c-c} measurements. The rest of the measurements are assumed to be uncorrelated. Let's call the vector of measurements $\vec{Y}$ and its covariance matrix V_y (Eq. 9.6). Each of the measurements depends on, and thus constrains, one or more parameters. To find the parameters that describe the measured quantities, we have to do a fit to the data, minimizing χ^2:

$$\chi^2 = [\, Y_I - F_I(\vec{P}) \,]\, V_{y_{IJ}}{}^{-1} \,[\, Y_J - F_J[\vec{P}] \,] \qquad ,$$

where $V_{y_{IJ}}$ is the covariance matrix for the measurements discussed below. Assuming again that in the vicinity of the χ^2 minimum variation of $\vec{Y}$ is a

177

linear function of $\vec{P}$:

$$\Delta Y_j^I = \frac{\partial Y_I}{\partial P_j} \Delta P_j \equiv D_j^I \, \Delta P_j$$

the minimum of the χ^2 is reached when parameters $\vec{P}$ are equal to:

$$P_i = (D_i^J V_{y\,JK}^{-1} D_l^K)^{-1} D_l^M V_{y\,MN}^{-1} Y_N \equiv A_i^N Y_N \qquad , \qquad (9.4)$$

and then parameter covariance matrix E is given by

$$E_{ij} = A_i^K V_{y\,KL} A_j^L \qquad\qquad (9.5)$$

as the result of the propagation of the $\vec{Y}$ errors to $\vec{P}$ errors [24].

I calculate the derivative matrix D_J^I in the same way as above. I vary the measured quantity (such as Z mass) by one standard deviation, determine the change in the parameter, and take the inverse ratio as the derivative. If the measurement does not depend on a parameter then that corresponding derivative is zero. Most of the measurements listed above have only one non-zero derivative. The only measurement that depends on more than one parameter is the CC Z mass measurement. It depends on $\alpha_{cc}, \delta_{cc}, \beta_{cdc}, r_0$ and

178

the theoretical model.

As noted above, the measurements of α_{edge}, c_{edge} and f_{edge} are correlated. I calculate the correlation between them in a simular way to that described above. I vary one of the measurement's free parameters (P_i) by one standard deviation, which moves measurement Y_I by $\sigma(Y_I)$, generate a MC sample using a MC grid in bins of other parameters (generated with unchanged parameters), fit for the parameters, and measure the variation of its fitted value δY_J. The correlation is

$$V_{y_{IJ}} \equiv < \Delta Y_I \Delta Y_J > = -\frac{\sigma(Y_I)\delta Y_J}{\sigma(Y_I)\sigma(Y_J)}\sigma(Y_I)\sigma(Y_J) \equiv -\delta Y_J \sigma(Y_I) \qquad (9.6)$$

Table 9.1 shows these correlations.

Measurements	M_Z^{cc-cc} fit	σ_Z^{cc-cc} fit	α_{edge} fit	c_{edge} fit	f_{edge} fit
M_Z^{cc-cc} fits	1.	0.	-0.05	-0.06	0.11
σ_Z^{cc-cc} fit	0.	1.	0.003	-0.08	-0.15
α_{edge} fit	-0.05	0.003	1.	-0.06	0.14
c_{edge} fit	-0.06	-0.08	-0.06	1.	-0.49
f_{edge} fit	0.11	-0.15	0.14	-0.49	1.

Table 9.1: Correlation between edge and C-C Z sample measurements.

The above algorithm can be summarized by: fit the measurements for the vector of parameters, obtain the parameter covariance matrix as the result

of the fit, and propagate it to W mass uncertainty.

9.3   Systematic errors

Source	M_W, $m_t(W)$	M_W, $p_t(e)$	M_W, $p_t(\nu)$
Statistics	234	263	311
Edge EM scale (α_{edge})	265	309	346
CC EM scale (α_{cc})	128	131	113
CC EM offset (δ_{cc})	142	139	145
calorimeter uniformity	10	10	10
CDC scale	38	40	52
backgrounds	10	20	20
CC EM constant term c_{cc}	15	18	2
Edge EM constant term c_{edge}	268	344	404
Fraction of events (f_{edge})	8	14	22
Hadronic response	20	16	46
Hadronic resolution	25	10	90
$U_\parallel$ correction	15	15	20
$U_\parallel$ efficiency	2	9	20
parton luminosity	9	11	9
radiative corrections	3	6	0
2γ	3	6	0
PDF	0	64	9
$P_T(W)$ spectrum	10	50	25
W Width	10	10	10

Table 9.2: Edge W mass errors, in MeV.

In order to use the above formalism all I have to know are the different

derivatives of measured quantities with respect to parameters used in the

Monte Carlo model. I have calculated them, and used Eqs. 9.3 and 9.5 to estimate the total uncertainty of the edge electron W mass measurements:

$m_t(W)$ fit :

$M_W = 80.596 \pm 0.234(stat) \pm 0.370(syst) = 80.596 \pm 0.438$ GeV.

$p_t(e)$ fit :

$M_W = 80.733 \pm 0.263(stat) \pm 0.460(syst) = 80.733 \pm 0.530$ GeV.

$p_t(\nu)$ fit :

$M_W = 80.511 \pm 0.311(stat) \pm 0.523(syst) = 80.511 \pm 0.609$ GeV.

$$(9.7)$$

Table 9.2 contains the relative contributions to the total errors from each of the parameters individually.

9.4 Determination of EM scale for non-edge electrons

9.4.1 CC EM scale

The Z $\widetilde{\text{C}}$-C data sample brings new events which can be used to constrain not only edge parameters, but also to bring down the uncertainty of the non-edge
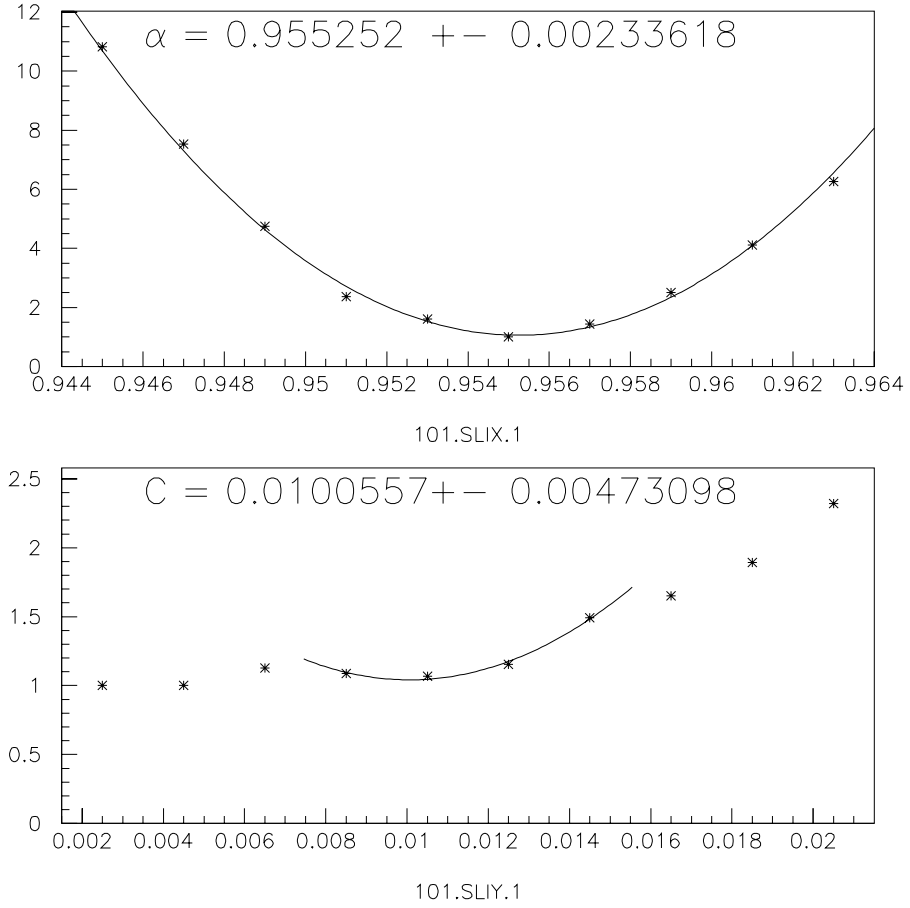
Figure 9.8: Z $\widetilde{C}$-C events. Z invariant dielectron mass distibution maximum likelihood fit with CMS grids for α_{cc} and c_{cc}. The top plot shows -log(likelihood) as a function of α_{cc}, fitted with a parabola. The bottom plot shows -log(likelihood) as a function of c_{cc}, fitted with a parabola.

EM parameters. I used the $\widetilde{\text{C}}$-C sample to put additional constraints on the non-edge EM scale α_{cc} and the non-edge EM resolution constant term c_{cc}. I used the same approach as in section 4.3. I generated a 1-dimensional grid of Z mass templates in bins of α_{cc} and c_{cc}, and fit for the parameters. The result is shown in Fig. 9.8.

$$\alpha_{cc} = 0.9552 \pm 0.0023$$

$$c_{cc} = 0.01 \pm 0.01$$

The log(likelihood) value is such that c_{cc} is consistent with being zero as well. Moreover, c_{cc} is meaningful only if it is positive, and that is why I have assigned an error equal to the value of the parameter itself.

The values from previous C-C Z's fits [7] are:

$$\alpha_{cc} = 0.9540 \pm 0.0008 \tag{9.8}$$

$$c_{cc} = 0.0115 \, {}^{+0.0027}_{-0.0036}$$

The measurements are correlated with each other and with the edge parameters measurements. The correlation has been calculated using the above

183

formalism and the values are presented in the Table 9.3.

Measurements	α_{cc} measurement	α_{edge} measurement
α_{cc} measurement	1.	-0.15
α_{edge} measurement	-0.15	1.

Table 9.3: Correlation between α_{cc} and α_{edge} measurements using $\widetilde{\text{C}}$-C Z sample.

9.4.2   EC EM scale

We have also available a small data set of Z $\widetilde{\text{C}}$-E events. They are less powerful in constraining α_{cc} or α_{ec} than the Z $\widetilde{\text{C}}$-C events because only one of two electrons is sensitive to either of two parameters, but they still can provide us with some improvement. As above, I generate a 1D grid of the Z mass templates and fit for α_{cc} and α_{ec}, and calculate the correlations between the two measurements to obtain:

$$\alpha_{cc} = 0.9559 \pm 0.0107$$

$$\alpha_{ec} = 0.9539 \pm 0.0085$$

184

The value from C-E and E-E Z's fits [8] is:

$$\alpha_{ec} = 0.95179 \pm 0.00187 \qquad\qquad (9.9)$$

Measurements	α_{cc} meas.	α_{ec} meas.	α_{edge} meas.
α_{cc} meas.	1.	-0.95	0.
α_{ec} meas.	-0.95	1.	0.
α_{edge} meas.	0.	0.	1.

Table 9.4: Correlation between α_{cc}, α_{edge} and α_{ec} measurements using $\widetilde{\text{C}}$-E Z sample.

The results are in Fig. 9.9 and Table 9.4.

9.4.3   Combining CC and EC EM scales measurements

I can combine the above EM scale measurements with the previous CC and EC EM scale measurements. The combined non-edge α_{cc} is :

$$\alpha_{cc} = 0.9541 \pm 0.00075 \qquad , \qquad\qquad (9.10)$$

up by 0.0001 from the published value (Eq. 9.8) and with the error reduced by 6%.
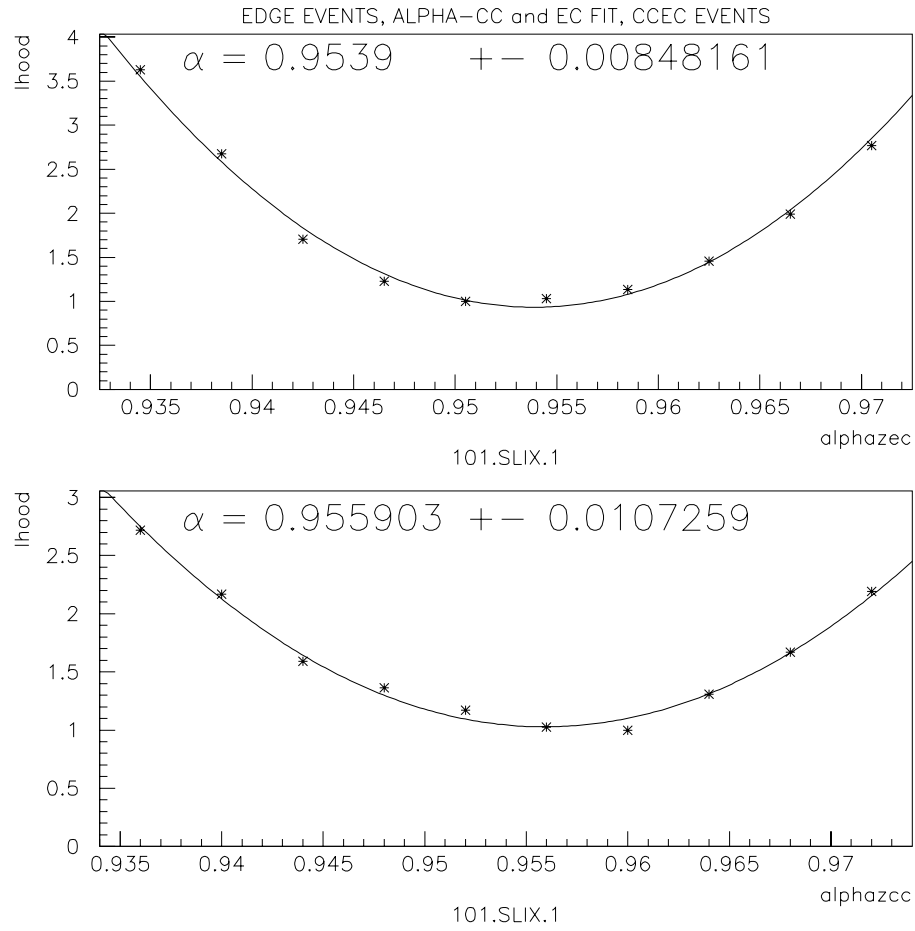
Figure 9.9: Z $\widetilde{C}$-E events. Z invariant dielectron mass distibution maximum likelihood fit with CMS grids for α_{cc} and α_{ec}. The top plot shows -log(likelihood) as a function of α_{ec}, fitted with a parabola. The bottom plot shows -log(likelihood) as a function of α_{cc}, fitted with a parabola.

The combined α_{ec} is :

$$\alpha_{ec} = 0.95189 \pm 0.00183 \qquad , \qquad (9.11)$$

increased by 0.0001 from the published value (Eq. 9.9) and with the error reduced by 2%.

The implications of these new measurements are not limited to error reduction only. It also means that because of the added $\widetilde{\text{C}}$-C and $\widetilde{\text{C}}$-E Z's statistics our knowledge of EM scales (CC and EC) has changed and we have to refit C and E W's using the new EM scale values. The refit W masses are:

$$M_W = 80.438 \pm 0.107 \text{ GeV, } \chi^2 = 0.12/2 \quad \text{(CC)}$$

$$M_W = 80.679 \pm 0.209 \text{ GeV, } \chi^2 = 4.0/2 \quad \text{(EC)}$$

To be compared with published results :

$$M_W = 80.446 \pm 0.108 \text{ GeV, } \chi^2 = 0.12/2 \quad \text{(CC)}$$

$$M_W = 80.691 \pm 0.227 \text{ GeV, } \chi^2 = 4.0/2 \quad \text{(EC)}$$

Chapter 10

Combination of DØ W mass measurements

There have been three previous analyses measuring the W boson mass with the DØ detector. One analysis using Run 1a data ($m_t(W)$ fit) and two measurements using Run Ib data – central electron analyses ($m_t(W)$, $p_t(e)$, $p_t(\nu)$ fits) and EC electron analysis ($m_t(W)$, $p_t(e)$, $p_t(\nu)$ fits). I can use the formalism presented in Chapter 9 and expand Eq. 9.3 to the case of multiple final measurements. I have a vector $\vec{M}$ of 10 W mass measurements:

- Run1a W mass measurement ($m_t(W)$ fit)

- 3 CC W mass measurements ($m_t(W)$, $p_t(e)$, $p_t(\nu)$ fits)

- 3 EC W mass measurements ($m_t(W)$, $p_t(e)$, $p_t(\nu)$ fits)

- 3 Edge W mass measurements ($m_t(W)$, $p_t(e)$, $p_t(\nu)$ fits)

All of them depend on a vector of parameters $\vec{P}$. The set of parameters has to be expanded to include EC and independent Run 1a parameters:

- Run 1a, CC, EC W mass statistical errors

- Run 1a systematical error independent from other W measurements

- EM scale α_{ec} and offset δ_{ec}

- FDC scale β_{fdc} and FDC-EC relative scale β_{ec}

- EM resolution constant terms c_{ecem}

- background b_{ec}

- $U_{\parallel}$ correction u_{ec}

- $U_{\parallel}$ efficiency ε_{ec}

and a list of measurements (and the parameters they constrain in brackets) that constrain them along with the above constraints from the Z $\widetilde{\text{C}}$-C and $\widetilde{\text{C}}$-E measurements.

- CC EM scales measurement with $\widetilde{\text{C}}$-C Z events (α_{cc})

- CC EM scales measurement with $\widetilde{\text{C}}$-E Z events (α_{cc})

- EC EM scales measurement with $\widetilde{\text{C}}$-E Z events (α_{ec})

- The Z mass measurements M_Z^{EE}, using E-E Z's

  (FDC scale β_{fdc}, δ_{ec}, radiative event corrections, α_{ec}, FDC-EC relative scale β_{ec}, EC $U_\parallel$ correction, two γ radiative event corrections, parton luminosity β)

- The Z mass measurements M_Z^{eccc}, using C-E Z's

  (FDC scale β_{fdc}, δ_{cc}, CDC scale β_{cdc}, α_{cc}, δ_{ec}, radiative event corrections, α_{ec}, FDC-EC relative scale β_{ec}, EC $U_\parallel$ correction u_{ec}, two γ radiative event correction, parton luminosity β)

- FDC radial calibration θ_{fdc} (FDC scale β_{fdc})

- FDC-EC relative radial calibration θ_{ec} (FDC-EC relative scale β_{ec})

- EC EM offset δ_{ec} (δ_{ec})

- Gaussian width fitted to Z peak σ^{ec-ec}, using E-E Z's (c_{ecem})

- Gaussian width fitted to Z peak σ^{cc-ec}, using C-E Z's (c_{ccem}, c_{ecem})

191

- measurements of EC $U_{\parallel}$ (EC $U_{\parallel}$ u_{ec})

- measurements of EC $U_{\parallel}$ efficiency ($U_{\parallel}$ efficiency ε_{ec})

Using Eq. [9.5] I calculated an expanded covariance matrix E and then propagated it into a 10 by 10 covariance matrix of W mass measurements E_M using the expanded version of Eq. [9.3]:

$$E_{M\alpha\beta} = D_i^{\alpha} E_{ij} D_j^{\beta} \tag{10.1}$$

where D_i^{α} is the matrix of derivatives. Each row is vector of derivatives of W mass measurement M_{α} to vector of parameters P_i.

$$D_i^{\alpha} \equiv \frac{\partial M_{\alpha}}{\partial P_i}$$

I then combine 10 W mass measurements by treating them as measurements of the single parameter M_W and fitting them minimizing χ^2:

$$\chi^2 = \sum_{\alpha,\beta=1}^{N} (M_{\alpha} - M_W) R_{\alpha\beta} (M_{\beta} - M_W) \tag{10.2}$$

where $R \equiv E_M^{-1}$ and indices α, β run over W mass measurements. The best

fit corresponds to

$$M_W = (\sum_{\alpha,\beta=1}^{N} R_{\alpha\beta} M_\alpha)/ \sum_{\alpha,\beta=1}^{N} R_{\alpha\beta} \qquad (10.3)$$

With uncertainty

$$\sigma(M_W) = (\sum_{\alpha,\beta=1}^{N} R_{\alpha\beta})^{-\frac{1}{2}} \qquad (10.4)$$

10.1   Results

The combination of the edge W mass measurements gives:

$$M_W = 80.574 \pm 0.405 \text{ GeV}, \ \chi^2 = 0.61/2 \quad \text{(Edge)}$$

The three EC measurements have produced a smaller error than in [8] due

to additional constraints on the CC and EC EM scales added in this analysis

from $\widetilde{\text{C}}$-C and $\widetilde{\text{C}}$-E Z's. The published W masses are:

$$M_W = 80.446 \pm 0.108 \text{ GeV}, \ \chi^2 = 0.12/2 \quad \text{(CC)}$$

$$M_W = 80.691 \pm 0.227 \text{ GeV}, \ \chi^2 = 4.0/2 \quad \text{(EC)}$$

With the constraints from $\widetilde{C}$-C and $\widetilde{C}$-E fits to the CC EM scale (but using *published* α_{cc} and α_{ec}), the three CC measurements give:

$$M_W = 80.446 \pm 0.107 \text{ GeV}, \ \chi^2 = 0.12/2 \quad \text{(CC)}$$

With the constraints from $\widetilde{C}$-C and $\widetilde{C}$-E fits for the CC and EC EM scales (using *published* α_{cc} and α_{ec}):

$$M_W = 80.687 \pm 0.209 \text{ GeV}, \ \chi^2 = 4.1/2 \quad \text{(EC)}$$

Refitting C and E W's using Eqs. [9.10, 9.11] and reduced α_{cc} and α_{ec} uncertainties (using *new* α_{cc} and α_{ec} values and reduced errors):

$$M_W = 80.438 \pm 0.107 \text{ GeV}, \ \chi^2 = 0.12/2 \quad \text{(CC)}$$

$$M_W = 80.679 \pm 0.209 \text{ GeV}, \ \chi^2 = 4.1/2 \quad \text{(EC)}$$

All non-edge measurements (smaller α_{cc} and α_{ec} uncertainties but *published* values) :

$$M_W = 80.489 \pm 0.085 \text{ GeV}, \ \chi^2 = 5.5/6 \quad \text{(CC \& EC \& RunIa)}$$

and with refitted C and E W masses(smaller α_{cc} and α_{ec} uncertainties and *new* values) :

$$M_W = 80.481 \pm 0.085 \text{ GeV}, \ \chi^2 = 5.5/6 \quad (\text{CC } \& \text{ EC } \& \text{ RunIa})$$

The W boson mass including all edge and non-edge measurements (but *published* α_{cc}, α_{ec} values):

$$M_W = 80.490 \pm 0.084 \text{ GeV}, \ \chi^2 = 6.3/9 \quad (\text{Run I})$$

and the final Run I DØ W boson mass including the edge electrons and refitted non-edge W events and *new* α_{cc}, α_{ec} values :

$$M_W = 80.483 \pm 0.084 \text{ GeV}, \ \chi^2 = 6.3/9 \quad (\text{Run I}).$$

This final result of this dissertation is to be compared with the last published Run I DØ W boson mass measurement:

$$M_W = 80.482 \pm 0.091 \text{ GeV} \quad (\text{published Run I}).$$

Thus this analysis achieves a 7 MeV improvement (8%) of the W mass uncertainty over the previous published result [8].

Chapter 11

Conclusions

We have presented a new measurement fo the W boson mass. We used previously unutilized $e\nu$ events, comprising 14% of the total Run 1b W boson statistics, with the decay electron measured by the central EM calorimeter. These events come from the edges of the DØ central calorimeter modules and are characterized by a different EM response. In this dissertation, we studied the detector response for these electrons and suggested a model that describes them.

We then performed a maximum likelihood fit to the $W \rightarrow e\nu$ events and

achieved the W mass uncertainty of

$$M_W = 80.574 \pm 0.405 \text{ GeV}$$

This value is consistent with the previous DØ and the world W mass measurements. The uncertainty is dominated by the systematic uncertainty on the parameters describing the EM response and the resolution of the edge electrons. We made further use of the calorimeter's module edges by utilizing $Z \to ee$ events with one of the electrons in the edge region. We performed the maximum likelihood fit to these Z events and extracted an improved EM scale and resolution for the non-edge central and also forward electrons. This measurement complements previous EM scale measurements performed in the DØ CC and EC W mass analyses. We have been able to reduce the systematic uncertainty of the non-edge CC and EC W mass measurements, leading to a smaller overall uncertainty on the combined Run I DØ W mass result :

$$M_W = 80.481 \pm 0.085 \text{ GeV}$$

Together with the edge W mass measurement, the new DØ W boson mass

value is

$$M_W = 80.483 \pm 0.084 \text{ GeV}$$

giving a 7 MeV improvement over the last published result.

This new result reduces the combined Tevatron W mass uncertainty by 2 MeV to 61 MeV. The world average W mass remains unchanged.

One of the benefits of the presented edge EM response model is that it opens the way for other analyses requiring a precise knowledge of the electron and photon energies measured by the central EM calorimeter to retrieve up to 14% of otherwise lost statistics.

Bibliography

[1] G. Arnison *et al.* (UA1 Collaboration), Phys. Lett. B **122**, 103 (1983).

[2] M. Banner *et al.* (UA2 Collaboration), Phys. Lett. B **122**, 476 (1983).

[3] G. Arnison *et al.* (UA1 Collaboration), Phys. Lett. B **126**, 398 (1983).

[4] P. Bagnaia *et al.* (UA2 Collaboration), Phys. Lett. B **129**, 130 (1983).

[5] J. Alitti *et al.* (UA2 Collaboration), Phys. Lett. **B** 276, 354 (1992).

[6] B. Abbott *et al.* (DØ Collaboration), Phys. Rev. D **58**, 012002 (1998).

[7] B. Abbott *et al.* (DØ Collaboration), Phys. Rev. D **58**, 092003 (1998).

[8] B. Abbott *et al.* (DØ Collaboration), Phys. Rev. D **62**, 092006 (2000).

[9] T. Affolder *et al.*(CDF Collaboration), Phys. Rev. Lett. **85**, 3347 (2000).

[10] R. Barate *et al.* (ALEPH Collaboration), "Measurement of the W Mass and Width in e^+e^- Collisions at $\sqrt{s} \sim 192 - 202$ GeV", European Physical Journal C **17** (2000).

[11] G. Abbiendi *et al.* (OPAL Collaboration), "Measurement of the Mass and Width of the W Boson in e^+e^- Collisions at 189 GeV", July 20, 2000. CERN-EP-2000-099, accepted by Phys. Lett. B.

[12] M. Acciarri *et al.* (The L3 Collaboration) "Preliminary Results on the Measurement of the Mass and Width of the W boson at LEP", L3 Note 2575, July 2000.

[13] P. Abreu *et al.* (DELPHI Collaboration), "Measurement of the mass and width of the W in e^+e^- Collisions at $\sqrt{s} = 192 - 202$ GeV", Phys. Lett. B **511**, 159, (2001).

[14] "A combination of Preliminary Electroweak Measurements and Constraints on the Standard Model", The LEP Collaborations ALEPH,DELPHI,L3,OPAL, the LEP Electroweak Working Group and the SLD Heavy Flavour and Electroweak Group, http://lepewwg.web.cern.ch/LEPEWWG/

[15] http://www-cdf.fnal.gov/physics/ewk/wmass_global.html

[16] B. Abbott *et al.* (DØ Collaboration), Phys. Rev. Lett. **80**, 2063 (1998); B. Abbott *et al.* (DØ Collaboration), Phys. Rev. **D 60**, 052001 (1999) and references therein.

[17] F. Abe *et al.* (CDF Collaboration), Phys. Rev. Lett. **82**, 271 (1999) and references therein.

[18] S. Abachi *et al.* (DØ Collaboration), Nucl. Instrum. Methods in Phys. Res. A **338**, 185 (1994).

[19] Eric Flattum, Ph.D. thesis, Michigan State University, 1996 (unpublished).

[20] Ian Adam, Ph.D. thesis, Columbia University, 1997 (unpublished).

[21] S.L. Glashow, Nucl. Phys. **22**, 579 (1961); S. Weinberg, Phys. Rev. Lett. **19**, 1264 (1967); A. Salam, in *Proceedings of the 8th Nobel Symposium*, ed. N. Svartholm (Almqvist and Wiksells, Stockholm, 1968), p. 367.

[22] I.J.R. Aitchison and A.J.G. Hey, "Gauge Theories in Particle Physics", Adam Hilger, 1989, 2nd Edition.

[23] V.D. Barger and R.J.N. Phillips, "Collider Physics", Addison-Wesley, 1987.

[24] R.M. Barnett *et al.*, Review of particle properties, Phys. Lett. **D54** (1996) .

[25] P. Chankowski *et al.*, Nucl. Phys. B**417**, 101 (1994); D. Garcia and J. Sola, Mod. Phys. Lett. A **9**, 211 (1994); A. Dabelstain, W. Hollik and W. Mosle, in *Perspectives for Electroweak Interactions in e^+e^- Collisions*, ed. by B.A. Kniehl (World Scientific, Singapore, 1995) p. 345; D. Pierce *et al.*, Nucl. Phys. B**491**, 3 (1997).

[26] CTEQ Collaboration, "Handbook of Perturbative QCD", Rev. Mod. Phys. **67**, January 1995.

[27] S. Abachi *et al.* (DØ Collaboration), Phys. Rev. Lett. **75**, 1456 (1995).

[28] G. Marchesini *et al.*, Compt. Phys. Commun. **67** 465 (1992), release 5.7.

[29] H. Plotow-Besch, CERN-PPE W5051 (1997), release 7.02.

[30] J. Collins, and D. Soper, Nucl. Phys. B **193**, 381 (1981).

[31] P. Arnold and R. Kaufmann, Nucl. Phys. B **349**, 381 (1991).

[32] G.A. Ladinsky and C.P. Yuan, Phys. Rev. D **50**, 4239 (1994).

[33] E. Mirkes, Nucl. Phys. B **387**, 3 (1992).

[34] J. Collins and D. Soper, Phys. Rev. D **16**, 2219 (1977).

[35] F.A. Berends and R. Kleiss, Z. Phys. C **27**, 365 (1985); F.A. Berends *et al.*, Z. Phys. C **27**, 155 (1985).

[36] J. Smith, W.L. Van Neerven, and J.A.M. Vermaseren, Phys. Rev. Lett. **50**, 1738, (1983).

[37] J. Thompson, "Introduction to Colliding Beams at Fermilab", DØ Note 2367, Fermilab-TM-1909.

[38] H. Aihara *et al.*, "Design, Construction and Performance of the Electromagnetic Module of the DØ End Calorimeter", Nucl. Instrum. Methods in Phys. Res. A **325**, 393 (1993).

[39] Scott Snyder, *Measurement of the Top Quark Mass in DØ* , Ph.D. Thesis, SUNY at Stony Brook (unpublished) (1995).

[40] Track match σ:
$\sigma_{\mathrm{trk}}^2 = (\frac{\Delta s}{\delta s})^2 + (\frac{\Delta z}{\delta z})^2$, Δs and Δz are the differences between extrapo-

lated to the third EM layer track position and the EM cluster centroid in the azimuthal (Δs) and in the z (Δz) directions.

[41] EM fraction:

$f_{EM} = \frac{E_{EM}}{E_{EM}+E_{HAD}}$, E_{EM} is a sum over four EM layers and E_{HAD} is a sum over all hadronic layers.

[42] Isolation:

$ISO = \frac{E(R<0.4)-E^{EM}(R<0.2)}{E^{EM}(R<0.2)}$, $E(R)$ is an electron's energy collected in the four EM layers and all hadronic layers within a cone with radius $R = \sqrt{\Delta\phi^2 + \Delta\eta^2}$. The electron energy collected in the EM layers only is $E^{EM}(R)$.

[43] Track match σ:

$\sigma^2_{\text{trk}} = (\frac{\Delta s}{\delta s})^2 + (\frac{\Delta \rho}{\delta \rho})^2$, Δs and Δz are the differences between extrapolated to the third EM layer track position and the EM cluster centroid in the azimuthal (Δs) and in the radial ($\Delta\rho$) directions.

[44] MICRO_BLANK veto is turned on for 1 to 2 microseconds every 20 microseconds, the circulation time of the beam in the Main Ring, vetoing events when the beam passes through the DØ detector.

[45] Protons were accelerated to about 125 GeV for antiproton production in the Main Ring, continuously, even when there was beam in the Tevatron. The cycle to inject, accelerate and extract the protons took 2.6 seconds. This was called the Main Ring Cycle. The losses during injection were (sometimes) quite large. The injection part of the cycle took 400ms. So, the MRBS_LOSS veto turns the experiment off during Main Ring injection, which occupies 400ms of the 2.6 second Main Ring Cycle.

[46] B. Abbott *et al.* (DØ Collaboration), Phys. Rev. D **57**, 3817 (1998).

[47] S. Aronson *et al.*, Nucl. Instr. and Meth. A 269 (1988) 492.